A spectrually integrated temporal albedo model for thin composite layers of snow and ice on roads
by Andrew Gregory Beddoe

A thesis submitted in partial fulfillment of the requirements for the degree of Master of Science in Mechanical Engineering
Montana State University

Abstract:
This study presents a spectrally integrated solar albedo model for thin composite layers of snow, ice and water on roads. The model is intended to support micro-scale thermal mapping models for forecasting highway pavement temperatures and surface conditions.

The snow-on-slab albedo (SOSA) model estimates the temporal road albedo by modeling surface conditions on highways that strongly affect solar albedo. Snow grain size, impurity concentration and optical mass were found to be important factors. These three factors were highly influenced by traffic and winter maintenance operations.

SOSA is composed of two components (1) a computation albedo routine CAR and (2) a pavement snow conditions routine SCR. CAR calculates visible, near infrared and solar albedos (0.3 - 5 /µm) from 7 physically based parameters: snow grain radius (&,mu;m), carbon soot concentration (mass fraction), mass cross-section (g/cm2), zenith cosine, atmospheric pressure (millibar), underlying surface albedo, diffuse fraction, surface downflux and atmospheric transmittance. SCR models the optical mass of water, ice, snow and sand, light absorbing impurities and the optical grain size. Inputs to SCR are meteorological parameters, surface energy fluxes and traffic parameters.

The optically equivalent grain size required in the model was 1/10th the observed grain size, partially due to the measurement protocol, which classified parficle size by the longest dimension. Optical radii ranged from 50- 150 µm. The sanding materials were the principle light absorbing impurity. Carbon residue from vehicle exhaust and tire residue was insignificant. The sanding material was composed primarily of basalt and granite and had ~0.07% the optical influence of carbon soot in the model. The 0.07% normalization factor is related to the ratio of the imaginary indices of refraction between carbon soot and the bulk sanding material.

Despite erratic and quickly changing surface conditions, SOSA proved effective in calculating albedo. SOSA had an overall standard deviation of 0.15 from observed albedos for the entire road and shoulder. The accuracy of the model improved when it was restricted to calculate albedos inside the lanes only. The standard deviation decreased to 0.11. As a result SOSA estimated surface temperatures accurately over a 24hr period. Surface temperature standard deviations were less than 1.7°C from measured values.

A SPECTRUALLY INTEGRATED TEMPORAL ALBEDO MODEL FOR THIN COMPOSITE LAYERS OF SNOW AND ICE ON ROADS

by

Andrew Gregory Beddoe

A thesis submitted in partial fulfillment
of the requirements for the degree

of

Master of Science

in

Mechanical Engineering

MONTANA STATE UNIVERSITY – BOZEMAN
Bozeman, Montana

November 29, 2001

APPROVAL

Of a thesis submitted by

Andrew Gregory Beddoe

This thesis has been read by each member of the thesis committee and has been found to be satisfactory regarding content, English usage, format, citations, bibliographic style, and consistency, and is ready for submission to the College of Graduate Studies.

Dr. Edward E. Adams — (Signature) — 29-NOV-2001 Date

Approved for the Department of Mechanical Engineering

Dr. Vic A. Cundy — (Signature) — 11/29/01 Date

Approved for the College of Graduate Studies

Dr. Bruce McLeod — (Signature) — 12-3-01 Date

STATEMENT OF PERMISSION TO USE

In presenting this thesis in partial fulfillment of the requirements for a master's degree at Montana State University – Bozeman, I agree that the library shall make it available to borrowers under rules of the Library.

If I have indicated my intention to copyright this thesis by including a copyright notice page, copying is allowable only for scholarly purposes, consistent with "fair use" as prescribed in the U.S. Copyright Law. Requests for permission for extended quotation from or reproduction of this thesis (paper) in whole or in parts may be granted only by the copyright holder.

Signature Andrew Bedloe

Date 11/30/2001

ACKNOWLEDGEMENTS

I would like to thank the Western Transportation Institute for providing the opportunity to conduct the research through their generous financial support via the Safe Passage project, as well as for scholastic assistance provided through the transportation graduate fellowship and graduate research assistantship. Special thanks to Dr. Edward Adams for his leadership, guidance and mentorship. Also, thanks to all others who provided their personal insight and recommendations, Dr. John Mounce, Dr. Douglas Cairns, Dr. Robert Brown, Dr. Jay Conant and Dr. Vic Cundy. Finally, a special thanks to my wife Mary Beddoe and other family members for their enduring support and love.

TABLE OF CONTENTS

LIST OF TABLES

LIST OF FIGURES

NOMENCLATURE

The following are the symbols used in the thesis

A	Cross-sectional control area (m^2).
AHP	Average hourly pass rate of winter maintenance vehicles.
AHT	Average vehicles per hour.
APT	Average vehicles per 15 minutes.
B	Thermal quality or fraction of ice in a unit mass of wet snow.
C_p	Specific heat (J/kg-K).
d_f	Diffuse fraction of solar downflux. Subscript c refers to clear sky diffuse fraction.
d_s	Geometrical snow depth (m).
D_{oyr}	Day of the year.
E	Amount of erosion. Subscripts v and m refer to vehicles and winter maintenance, respectively (kg/m^2).
$e_{a,.s}$	Water vapor pressure (kPa). Subscripts a and s refer to air and surface, respectively.
f_{3-3}	Fraction of near infrared flux from 3 to 5 μm.
f_{basalt}	Fraction of basalt in sanding materials.
G	Global irradiance (W/m^2). Sum of diffuse and direct solar radiation.
g	Gravitational acceleration (m/s^2).
G_{xs}	Geometrical cross-section (m^2).
I	Radiation flux (W/m^2). Subscript o stands for incident flux.
k	Boltzman molecular gas constant (J/molecule-K). Equation (42)
k	Thermal conductivity (W/m-K).

k_e Extinction coefficient (m^{-1}). Subscripts a and s stand for absorption and scattering, respectively.

$K_{h,e}$ Dimensionless turbulent heat transfer coefficient.

L Latent heat of transformation (kJ/kg). Subscripts f, s and v refer to fusion, sublimation and vaporization, respectively.

L Longwave radiation flux (W/m^2). Subscripts i and o refer to incident and emitted IR, respectively.

M Amount of melting in snow layer (kg/m^2).

m Mass (kg).

m_{mol} Molar mass of air (kg/mol). Equation (42).

$m_{re,\,im}$ Complex refractive index. Subscripts re and im stand for real and imaginary parts, respectively.

m_{xs} Optical mass cross-section (kg/m^2).

n Cloud cover fraction.

N Number density (m^{-3}).

n Number of particles. Equation (11).

N_a Avagodro's number (molecules/kmol).

N_f Normalization factor.

P Amount of precipitation (kg/m^2).

p Pressure (kPa or mmbar).

P_i Precipitation intensity (m/s).

Q Energy flux (W/m^2).

R Gas constant (kJ/kg-K).

r Particle radius (μm).

R_{DAPT} Average diurnal vehicle flow rate (Vehicles / 15 minutes).

R_{ef} Spectral reflectivity.

Re_x Dimensionless Reynolds number.

S Equivalent soot concentration of contaminate (mass-fraction).

t Atmospheric transmittance.

Δt time increment (seconds).

T Temperature (° C).

U Wind speed (m/s).

v Velocity (m/s)

V Volume (m^3).

WS Wavelength separation between visible and near infrared regions (0.7 or 0.9 μm).

x Optical path length or relative air mass (m).

x,y,z Cartesian coordinates.

x_c Characteristic length (m).

x_p Characteristic size of scattering particle used in Mie Theory.

y Elevation above reference pressure (m).

Z_e Extinction efficiency. Subscripts a and s stand for absorption and scattering, respectively.

z_g Nodal distance (m).

α Albedo.

β Attenuation coefficient (m^{-1})

ϵ Surface emisivity.

ϵ Internal energy per unit mass (J/kg). Equation (71).

θ Zenith angle (°).

Λ Thermal diffusivity (m^2/s).

λ	Wavelength (m).
μ_0	Cosine of the zenith angle.
ν	kinematic viscosity (m^2/s). Equation (68).
ν	Specific volume (m^3/kg). Equations (60) and (61).
ρ	Density (kg/m^3).
σ	Stefen_Boltzmann constant (W/m^2-K^4).
σ_e	Extinction cross-section (m^2). Subscripts a and s stand for absorption and scattering, respectively.
τ_o	Optical snow depth.
ϕ	Relative humidity.

ABSTRACT

This study presents a spectrally integrated solar albedo model for thin composite layers of snow, ice and water on roads. The model is intended to support micro-scale thermal mapping models for forecasting highway pavement temperatures and surface conditions.

The snow-on-slab albedo (SOSA) model estimates the temporal road albedo by modeling surface conditions on highways that strongly affect solar albedo. Snow grain size, impurity concentration and optical mass were found to be important factors. These three factors were highly influenced by traffic and winter maintenance operations.

SOSA is composed of two components (1) a computation albedo routine CAR and (2) a pavement snow conditions routine SCR. CAR calculates visible, near infrared and solar albedos (0.3 – 5 μm) from 7 physically based parameters: snow grain radius (μm), carbon soot concentration (mass fraction), mass cross-section (g/cm^2), zenith cosine, atmospheric pressure (millibar), underlying surface albedo, diffuse fraction, surface downflux and atmospheric transmittance. SCR models the optical mass of water, ice, snow and sand, light absorbing impurities and the optical grain size. Inputs to SCR are meteorological parameters, surface energy fluxes and traffic parameters.

The optically equivalent grain size required in the model was 1/10th the observed grain size, partially due to the measurement protocol, which classified particle size by the longest dimension. Optical radii ranged from 50 – 150 μm. The sanding materials were the principle light absorbing impurity. Carbon residue from vehicle exhaust and tire residue was insignificant. The sanding material was composed primarily of basalt and granite and had ~0.07% the optical influence of carbon soot in the model. The 0.07% normalization factor is related to the ratio of the imaginary indices of refraction between carbon soot and the bulk sanding material.

Despite erratic and quickly changing surface conditions, SOSA proved effective in calculating albedo. SOSA had an overall standard deviation of 0.15 from observed albedos for the entire road and shoulder. The accuracy of the model improved when it was restricted to calculate albedos inside the lanes only. The standard deviation decreased to 0.11. As a result SOSA estimated surface temperatures accurately over a 24hr period. Surface temperature standard deviations were less than 1.7°C from measured values.

CHAPTER 1

INTRODUCTION

Winter driving conditions are hazardous and often confront motorists with extreme temporal and spatial variability because of local topography, traffic, maintenance practices and meteorological influences. Winter conditions also contribute a large economic burden in loss of property, time delays, and labor and material costs expended in winter maintenance operations [Hanbali 1992]. Many roads may see the highest injuries and fatalities during snowy and icy conditions in part due to the high variability of snow and ice on roads, which complicate anti-snow and ice measures [Naruse et al. 1987]. Knowing exactly when and where snow and/or ice will begin to melt or refreeze could improve planning, help cut costs of snow and ice control and reduce hazards for winter maintenance crews and road users. Because of this, motorists and traffic management personal are in continual need of accurate real-time and forecasted road and weather conditions along rural roads and highways.

To assist in these efforts a more sophisticated snow albedo (reflectivity) model, controlled by the physical properties of snow, is needed for weather-related micro-forecast pavement temperature and condition models. A physically based albedo model will broaden the physical understanding and forecast accuracy of snow and ice formation and ablation on roads thus improving the effectiveness and deployment of anti-snow and ice measures. Albedo α plays a critical role in modeling efforts because it provides a quantitative measure of the fraction of incident solar radiation absorbed (e.g. fraction absorbed = 1 − α) near the surface, and is the dominate energy available to cause increases in road surface temperatures and melt snow on roads during winter [Ishikawa et al. 1987, Naruse et al. 1988, Nakawa et al. 1992].

Albedo refers to the reflectivity of a surface (fraction of energy reflected) in the solar spectrum (generally between 0.2 to 5 μm). and is commonly parameterized as the spectrally-averaged (allwave) albedo. The word itself, albedo, in late latin means whiteness, from the latin albus (white).

Snow is an excellent reflector of shortwave (solar) radiation and emitter of longwave radiation. This means that snow usually lowers absorbed solar energy during the day while effectively emitting longwave radiation at night, creating a net radiation loss from a surface. These conditions commonly cause surface cooling which can lead to ice formation on the road surface.

The albedo of a snow covered road is the result of a composite structure of pavement, ice, anti-skid materials (sand aggregate) and snow acting in concert to absorb, scatter and reflect incident radiation. Of these, snow has the greatest influence on the observed albedo because of its high albedo (e.g. pure semi-infinite snow 0.7 to 0.85, [Marshall 1989]) as compared to dry asphalt (e.g. new asphalt has an albedo of 0.04 and aged asphalt ~5 to 10 years has a mean albedo of 0.12 $\pm$ 0.03, [Pomerantz et al 1999]), water (e.g. an albedo of 0.06 for solar heights > 40 degrees, Fig 7.5, [Kondratyev 1969]) and common anti-skid abrasives (e.g. albedo of gray sand 0.18 to 0.23 , Table 7.3, [Kondratyev 1969]) used in winter maintenance.

It is apparent, then, that snow albedo has a enormous potential to change the amount of solar energy absorbed at the surface of the road. A change in snow albedo from 0.8 to 0.4 (e.g. from removal of snow by plowing or addition of light absorbing contaminates such as anti-skid materials) triples the amount of solar energy absorbed on the surface from 20% to 60% and may greatly accelerate melt [Naruse et al. 1988]. Even slight fluctuations in snow albedo may alter the onset of snowmelt or refreeze on the road, as indicated by Warren [1984] and Brown [1982] for undisturbed snow covers. Thus, an accurate knowledge of the surface albedo is required to precisely model when snowmelt and refreeze might occur.

Snow melting or aging generally has a positive feedback on the snow albedo. Albedo naturally decreases as snow ages because of snow grain growth and a decrease in snowcover thickness [Warren 1984]. As the albedo drops the snow cover is more efficient at absorbing solar energy which in turn increases ablation. This cycle is accelerated when traffic and winter maintenance are introduced and can rapidly change the snowcover conditions, which translates to a rapidly changing albedo [Ishikawa et al. 1987, Naruse et al. 1988]. Combined with dynamic solar effects from shadowing and thermal energy exchange between surfaces, particularly in mountainous regions, pavement temperatures and conditions during winter can fluctuate drastically along a road within a close distance.

Most snow albedo models to date have been developed for use in global climate modeling and were concerned only with natural snow covers experiencing seasonal metamorphism and ablation. The earliest albedo parameterizations treated albedo quite crudely, generally prescribing snow albedo as a single value, or basing it on a distribution of the surface albedo [Marshall 1989]. Others have taken a simple parameterization of snow albedo, dependent on temperature, age of snow, zenith angle or latitude [Table 1.1, Marshall 1989]. However, many of the earlier parameterizations are derived from data at a single site and are not universal parameterizations, as published by Pluss [1997]. A more sophisticated approach was applied to model snow albedo by Marshall [1989], based on the sophisticated theoretical work of Wiscombe and Warren [1980a and 1980b, here after WWI and WWII]. Marshall [1989] developed simple functions, which accurately fit the spectrally integrated (allwave) results of the theoretical spectral albedo model. The model requires 7 realistic physically tuned inputs, which allows the parameterization to be transferable to other locations. However, the model is developed for use in atmospheric general circulation models (GCMs) and seasonal snowcovers and is not directly applicable to thin snow and ice covers on pavement where direct influences from anthropogenic sources must be considered.

Traffic and winter maintenance are factors that indirectly influence snow albedo on roads, but have not been considered at all in albedo models. Actions by vehicles and maintenance practices both alter the physical snow properties, thus snow albedo. Vehicles mechanically break snow crystals, compact snow, mix contaminates, move and erode snow on the road. Maintenance operations deposit large amounts of contaminates on the snow through application of abrasives and remove snow mass by plowing. In addition, differences in local traffic and anti-snow and ice operations contribute to the variable snow conditions along the road. The net result of these transportation influences is to increase the inhomogeneity and to accelerate metamorphism and ablation of snow roads as compared to a seasonal snowpack, which complicates measuring and modeling efforts.

Within this thesis a allwave albedo model for thin composite layers of snow and ice on pavement (snow-on-slab) is presented. The albedo routine is adapted from a physically parameterized snow albedo model [Marshall 1989]. The snow-on-slab albedo (SOSA) model includes the effects from motor traffic and winter maintenance on the physical snow structure, contamination and ablation on pavement and is intended to support road surface temperature modeling efforts for snow and ice covered roads. The allwave albedo is calculated based on realistic physical conditions of the snowcover and the pavement.

This snow-on-slab albedo model is seen as necessary to improve the accuracy of pavement temperature forecasting. It provides the first ever (to the knowledge of the author) physically-based albedo model applied to snow and ice in a transportation setting. The model was developed to be incorperated into WinThermRT to improve albedo estimates to achieve more accurate forecast of surface temperatures (see Chapter 2). Improvements in surface temperature modeling will contribute to improved safety and efficiency on rural roads. Success of the thermal modeling will assist in increasing traveler safety through reduction in accidents, improve maintenance operations through effective and timely use of resources, and demonstrate the feasibility of ITS in rural applications.

The following summarize the rational for the thesis:

1. The high variance of albedo of snow and ice on roads plays an important role in the surface energy budget.
2. Current classification of snow and ice on roads is lacking in a sophisticated approach in modeling albedo.
3. Future highway safety and efficiency will benefit from a physically – based albedo model tailored to road and highway snow.
4. Assist in development of intelligent transportation systems in rural settings.
5. Improve accuracy of strategic road weather and condition forecasting models.

CHAPTER 2

BACKGROUND

Support for this research was provided by the *Safe Passage* Project, a cooperative effort by the Western Transportation Institute (WTI), MSU-Bozeman and the Montana Department of Transportation (MDT). Funding was provided by the Research and Special Programs Administration of the U.S. Department of Transportation through WTI.

The *Safe Passage* Project is concerned with optimizing weather related operations, motorist safety and incident management along Interstate 90 (I-90), a major east-west corridor between Livingston and Bozeman (Figure 1). Severe weather conditions common in the northern rockies, that consistently plague the corridor during winter months, compel the project to focus on the issue of weather and weather-related pavement conditions, reported as contributing to up to 70% of the accidents between 1994-1999 [Accident statistics, MDT, Safety Management Section, 1998]. Intelligent Transportations Systems (ITS) technologies such as road and weather information systems (RWIS), employed in *Safe Passage*, provide site-specific meteorological and pavement temperature data, an important component to icing. However, it is economically impossible to line entire stretches of roads with sensors, thus requiring extrapolation between RWIS sites. This limits strictly using RWIS as decision support tools regarding appropriate action in snow and ice control efforts because of the limited accuracy of extrapolated pavement temperatures due to small amounts data between sites. As a result a micro-forecast pavement temperature model (WinThermRT) which utilizes

ITS technology in conjunction with National Weather Surface (NWS) forecast data is in continuing development.

This thesis supports development of the computational thermal model (WinThermRT), an integral component of *Safe Passage,* which is intended to accurately micro-forecast pavement temperatures and roadway conditions. The thermal model (WinThermRT) is adapted from a computational model called PRISM (Physically Reasonable Infrared Signature Model) used by the U.S. Military to model surface temperatures of vehicles for use in infrared imagery [Adams and McDowell 1991]. PRISM uses a series of flat plates to represent the three-dimensional shape of a vehicle. Shadowing and surface to surface re-radiation are accounted for within the model. The concept was expanded to terrain and highways through employment of Geographic Information Systems (GIS) and Digital Elevation Maps (DEM) [Adams, WTI Report, Vol. 4 (1), March 2000].

Currently, WinThermRT micro-forecasts pavement temperatures to a 30 m resolution (Standard United States Geological Service (USGS) Dimensions) by extrapolating meteorological forecasted data (on a 40 km grid) obtained indirectly from the National Weather Service (NWS) and Eta program (a mesoscale meterological model, for more detail contact the National Oceanic and Atmospheric Administration NOAA) via the Advanced Regional Prediction System [ARPS, Xue et al. 2000]. The albedo model was developed only as a point model within WinThermRT. The spatial extrapolation of albedo across the complex terrain grid is accomplished through WinThermRT's platform.

Therefore, the surface albedo at the grid point represents the averaged abledo for a 30 m square surface over the road.

Bozeman Hill (BZH) was chosen as the research site. It is located within the corridor at mile marker 321.1 (Figure 2). Only west bound lanes of I-90 were studied. Bozeman Hill was selected as the site because it provided the highest point along the highway within the corridor and is a good representative of the severe weather within the corridor or other mountain passes. Also, an existing MDT RWIS adjacent the highway helped reduce cost and construction time and provided an existing system into which additional radiation sensors could be integrated.

Radiation

Thermal models for pavement icing are primarily concerned with radiant energy exchange on a surface in the shortwave and longwave regions. Albedo is important in radiant energy exchange on surfaces because knowledge of albedo makes it possible to determine the amount of heat obtained from incoming shortwave (solar) radiation.

Shortwave Radiation

Radiation from the sun is the primary energy fueling atmospheric motions and different processes in the atmosphere, on the earth's surface and in the oceans [Kondratyev 1969, Pluss 1997]. Radiation emitted by the sun may be regarded as

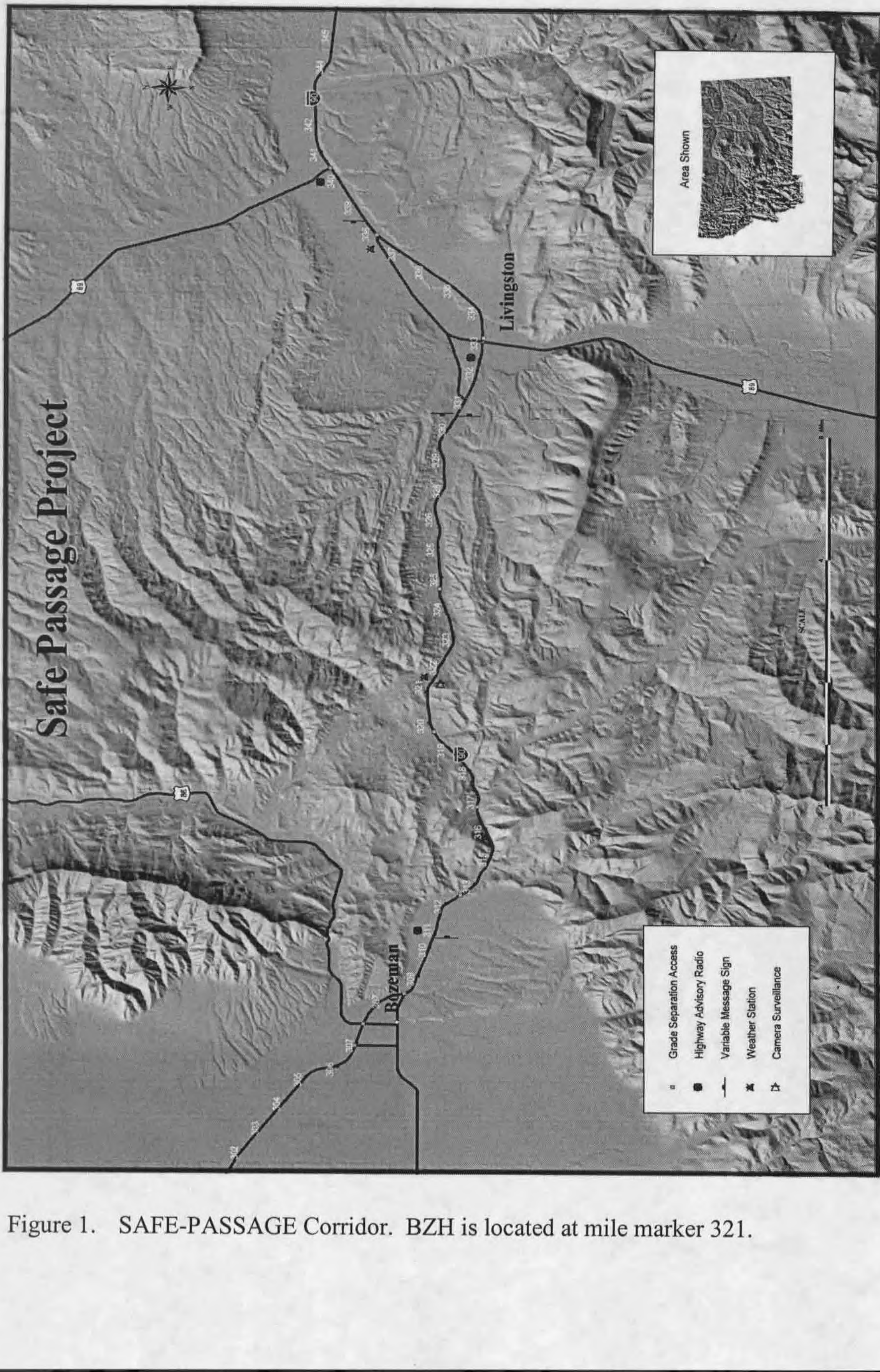

Figure 1. SAFE-PASSAGE Corridor. BZH is located at mile marker 321.

Figure 2. Aerial photo of BZH

approximately equivalent to a black body radiating at 6000 K [Figure 1.11, Robinson 1966]. More than 98% of the total energy received from the sun at the top of the atmosphere is between the wavelengths 0.2 to 5 μm [Robinson 1966, Kondratyev 1969, Pluss 1997]. Less than 0.1% of the total solar energy is below 0.3 μm due to absorption by stratospheric ozone [Marshall 1989]. Consequently, ultraviolet contributes little to the radiant energy flux at the earth's surface. This spectral region, 0.2 to 5 μm, is referred to as *shortwave* or *solar* radiation. *Longwave* IR (terrestrial) radiation refers to the thermal energy of the earth's surface and atmosphere within the spectral region 5 to 100 μm.

The amount of solar radiation incident at the top of the atmosphere is known as the solar constant S [Pluss 1997]. It is defined as the magnitude of solar flux passing per unit time (1 second) through a unit surface (1 m^2) perpendicular to the sun's rays at a distance of 1 astronomical unit [149.5 x 10^6 km, Robinson 1966]. The astronomical unit represents the mean distance between the shortest distance and the longest distance in earth's orbit around the sun [Robinson 1966].

Solar radiation entering the atmosphere undergoes successive selective attenuation which alters the spectral and angular distribution of the surface down-flux from that at the top of the atmosphere. A portion of the flux is absorbed by constituents in the atmosphere, a portion is scattered by molecules (Rayleigh scattering) and aerosols (Mie scattering) leading to *diffuse* radiation, and the remainder reaches the surface as *direct* radiation [Kondratyev 1969, Marshall 1989, Pluss 1997]. The sum of diffuse and direct radiation at the earth's surface is commonly referred to as *global* radiation and can fluctuate greatly due to variations in cloud cover and solar zenith angle. Global radiation is subdivided into three spectral regions UV, VIS and NIR (Table 1). The visible spectrum is further divided into wavelength by corresponding perceived colors (Table 2).

Table 1. Solar radiation wavelength regions and respective mean radiation energy. The wavelength separation between VIS and NIR for radiative transfer models is generally divided at 0.7 or 0.9 μm. ARPS makes the separation at 0.7 μm. Reproduced from Pluss [1997].

Wavelength (μm)	Name	Mean radiation energy at the earth surface
0.2-0.4	Ultraviolet (UV)	9%
0.4-0.75	Visible (VIS)	49%
0.75-5.0	Near Infrared (NIR)	42%

Table 2. VIS wavelength regions and the corresponding colors. Reproduced from Table 1.4, Kondratyev [1969].

Color	Wavelength Interval (μm)	Typical Wavelength (μm)
Violet	0.390 – 0.455	0.430
Dark blue	0.455 – 0.485	0.470
Light blue	0.485 – 0.505	0.495
Green	0.505 – 0.550	0.530
Yellow-green	0.550 – 0.575	0.560
Yellow	0.575 – 0.585	0.580
Orange	0.585 – 0.620	0.600
Red	0.620 – 0.760	0.640

Atmospheric transmittance refers to the selective attenuation of certain wavelengths in the atmosphere that alters the spectral composition at the earth's surface and in turn effects albedo. Atmospheric transmittance is the ratio of surface solar downflux to solar downflux at the top of the atmosphere. Maximum values on clear days will only reach as high as 0.7 to 0.8 because of the presence of Rayleigh scattering [Marshall 1989].

Direct shortwave radiation at the earth's surface depends on atmospheric composition, cloud cover and the optical path length of the beam of light. The fraction of solar radiation scattered, reflected and refracted within the atmosphere refers to diffuse radiation. Diffuse fraction of solar radiation influences snow albedo because it alters the effective zenith angle of the incoming radiation [WWI]. On clear days, diffuse flux, a result of molecular scattering, may account for about 10 – 15% of global radiation [Pluss 1997]. However, the main cause of diffuse radiation is due to clouds [Pluss 1997]. As a result, an overcast day may be virtually diffuse. This condition allowed Pluss [1997] to simplify the parameterization of diffuse radiation by assuming isotropy because on clear days the diffuse fraction was small and on cloudy days the diffuse fraction was nearly isotropic.

Absorption and Scattering by Particles. The attenuation of light interacting with particulate matter is caused by two mechanisms, absorption and scattering. The underlying process of scattering involves the removal of energy from an incident electromagnetic wave and the subsequent reemission of some portion of the energy with essentially no change in wavelength. The portion that is not re-emitted and goes to raise the internal energy of the particle refers to absorption.

The Lambert or Bouger law describes attenuation of light by a medium interacting with light as,

$$I(\lambda)=I_o(\lambda)\cdot e^{(-\beta(\lambda)\cdot x)} \tag{1}$$

where I_o is incident flux of monochromatic light, I is the flux after passing through a distance x known as the optical path length (m) and $\beta(\lambda)$ is the attenuation coefficient (m^{-1}) determined by the material interacting with light [Horvath 1993]. When both scattering and absorption are involved in the attenuation of light, $\beta(\lambda)$ is called the extinction coefficient k_e and is written as the sum of the absorption coefficient k_a and the scattering coefficient k_s,

$$k_e = k_a + k_s \tag{2}$$

It follows that,

$$\sigma_e = \sigma_a + \sigma_s \tag{3}$$

$$Z_e = Z_a + Z_s \tag{4}$$

where σ_e is the extinction cross-section (m^2) and Z_e is the dimensionless extinction efficiency [Hansen and Travis 1974]. The extinction efficiency refers to the amount of light attenuated by the particle relative to amount of light incident on the cross-section [Hansen and Travis 1974, Horvath 1993], and is represented as,

$$Z_e = \frac{\sigma_e}{G_{xs}} \tag{5}$$

where G_{xs} is the geometric cross-section (m^2). The extinction cross-section may be understood as the area illuminated in the medium or on a particle by a cross-section of incident light.

Particles that do not absorb light have only a real spectral refractive index m, but if they do absorb light the spectral refractive index is complex,

$$m(\lambda) = m_{re}(\lambda) + i \cdot m_{im}(\lambda)$$

(6)

where $m_{re}(\lambda)$ is the real part and represents velocity of the optical wave in the particle and the imaginary part $m_{im}(\lambda)$ represents damping of light by the bulk material [Akhmanov and Nikitin 1997].

The extinction coefficient k_e may be obtained from the imaginary part of the spectral refractive index of the medium as

$$k_e(\lambda) = \frac{4 \cdot \pi \cdot m_{im}(\lambda)}{\lambda} \tag{7}$$

The single-scattering albedo ω, essential for multiple-scattering problems, is defined as the ratio of scattering to extinction cross -section,

$$\omega = \frac{\sigma_s}{\sigma_e} = \frac{k_s}{k_e} = \frac{Z_s}{Z_e} \tag{8}$$

and refers to the fraction of energy removed from the incident beam [Hansen and Travis 1974, WWI].

The phenomena of attenuation may be simplified by considering absorption and scattering by a single particle (*single scattering*) while in reality it involves successive interactions (*multiple scattering*) by two or more particles. In determining single-scattering of electromagnetic radiation two fundamental theories are usually introduced, that assume scattering by independent particles. In the solar spectrum the snow particles and the mean optical path between grains are large enough compared to wavelength that little error is induced from this assumption [WWI, Sergent 1998]:

1.) *Rayleigh scattering* considers scattering by molecules small compared to wavelength (such as air, nitrogen and ozone) [Meyer-Arendt 1984, Pluss 1997]. Particles that cause Rayleigh scattering are about one-tenth the wavelength of incident light. Rayleigh molecules are small compared to the incident wave and thus the assumption may be made that there is a constant electric field across the particle. This allows a simplification by assuming a single *electric dipole* for each molecule [Meyer-Arendt 1984, Serway 1990]. As a result Rayleigh particles scatter in phase, which leads to symmetric scattering [Hansen and Travis 1974].

A main characteristic of Rayleigh scattering is the symmetric forward and backward scattering by molecules that follows a $1 + \cos^2(\theta)$ distribution (Figure 3), e.g., the forward and backward components are twice the scattering at $\theta = 90°$ directions.

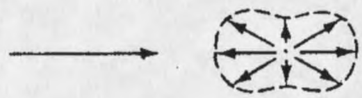

Small particles: Rayleigh scattering

Large particles: Mie scattering

Figure 3. Angular distribution in Rayleigh and Mie scattering. Reproduced from Figure 3.3-6 Meyer-Arendt [1984].

Rayleigh scattering is also characterized by extreme wavelength dependence. Rayleigh showed that the intensity of scattered light, i, is inversely proportional to the fourth power of the wavelength:

$$i \approx \frac{1}{\lambda^4} \tag{9}$$

This states that light of shorter wavelength is scattered by molecules much more than the longer wavelengths. Figure 4 shows intensity of scattering vs. wavelength.

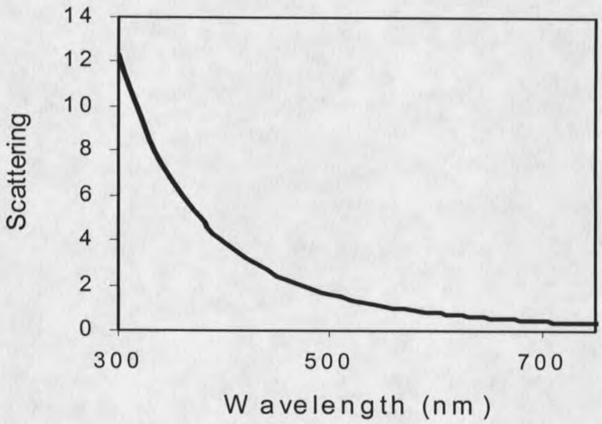

Figure 4. A plot of Rayleigh scattering intensity as a function of wavelength.

Within a molecule positive charges (protons) are heavy compared to negative charges (electrons) and move little compared to electrons when under extinction of an incident wave. Therefore, electrons are most sensitive to induced oscillations [Meyer-Arendt 1984]. Electrons also reradiate the absorbed electromagnetic radiation. This *reradiation* is the fundamental process to molecular light scattering. As the frequency of the impinging electric field approaches the resonate frequency of the electron-oscillators, which generally have resonances in the ultraviolet, the amplitude of the electron-oscillators, and hence the ability of the molecule to remove energy from the lightwave, increases which enhances the scattering ability of the molecule [Meyer-Arendt 1984]. This is why molecules scatter light more readily in the atmosphere as wavelength decreases towards ultraviolet. It is the reason the sky appears blue.

For more detail and information on Rayleigh scattering coefficients see Hansen and Travis [1974] and others such as van de Hulst [1957], Born and Wolf [1965], Kondratyev [1969] and Meyer-Arendt [1984].

2.) *Mie scattering* considers scattering by particles large compared to wavelength (such as dust aerosols, water vapor or ice crystals) [Meyer-Arendt 1984, Pluss 1997]. Particles that scatter according to Mie theory are greater than one-tenth the wavelength of incident light. Scattering of light by clouds and snow is primarily due to Mie scattering affects. Mie scattering differs from Rayleigh scattering in that is not wavelength dependent and scattering is antisymmetric (Figure 3).

The nonsymmetrical scattering results from scattered light from one point on the particle being out of phase with light scattered from another point, the light interferes causing the scattered-light distribution to be anisymmetric.

Mie particles primarily scatter in a forward direction with no dependence on wavelength, which explains way most clouds appear white. As particle increase in size they become more forward scattering. For larger particles angular dependence of scattering becomes complicated, often showing many maxima and minima, requiring multiple parameters to describe [Meyer-Arendt 1984]. As a result, Mie theory takes into account size of particles, refractive index of scattering particle and the surrounding medium, dielectric constant and the absorptivity of the particles [Meyer-Arendt 1984].

The size of Mie particles (assumed spherical) relative to wavelength λ is given by,

$$x_p = \frac{2 \cdot r \cdot \pi}{\lambda} \tag{10}$$

where r is the particle radius. The extinction cross-section is represented as

$$\sigma_e = Z_e \cdot r^2 \pi \cdot n \tag{11}$$

where n is the number of particles and Z_e is the extinction efficiency.

Because Mie particles are large compared to wavelength the induced electric field of the particle by the incident wave cannot be considered constant and thus the simplification of assuming only one dipole is inadequate. Often, Mie theory considers multidipoles. As a result, the derivation of Mie scattering coefficients is mathematically complicated and extensive. For more detail see Hansen and

Travis [1974] and others van de Hulst [1957], Born and Wolf [1965], Kondratyev [1969] and Meyer-Arendt [1984].

Once single-scattering parameters are computed, multiple-scattering which occurs in the bulk medium is simulated by a variety of methods in radiative transfer theory. A number of multiple-scattering theories for bulk mediums have been developed. Hansen and Travis [1974] review a few multiple-scattering theories as applied to planetary atmospheres, these include the adding-doubling method, method of successive orders, iteration of formal solution, invariant imbedding, method of x and y functions, discrete ordinate method, spherical harmonic method and the Monte Carlo method.

The parameterization of albedo used in the thesis is based on the radiative transfer model of Wiscombe and Warren [WWI, WWII], which uses the delta-Eddington approximation for multiple-scattering [Marshall 1989]. It was chosen by Wiscombe and Warren because it is capable of handling strongly forward-directed scattering, as is the case with snow particles [WWI]. The delta-Eddington approximation can also account for direct and diffuse radiation incident on the snowpack eliminating restrictions inherent in earlier methods [WWI]. For more detail see Joseph et al. [1976] and WWI.

Albedo

Radiant energy incident on a surface (snow, water, asphalt, etc..) is partially reflected and absorbed. The fraction reflected (albedo) differs for many kinds of surfaces and is directly affected by the spectral and angular composition of the solar irradiance and the physical properties of the surface. Essentially, albedo is an exhibited material property of the surface. Lower albedos indicate that more radiation is absorbed on a surface. Absorbed radiation may be converted to thermal heat causing the surface to warm or induce phase change. High albedo surfaces absorb less irradiance reducing the solar influence to the surface and thus tend to be cooler.

Allwave albedo α is defined as the ratio of reflected Q_r to incident Q_i shortwave radiation,

$$\alpha = \frac{Q_r}{Q_i} \tag{12}$$

and is taken as a decimal fraction or a percent [Gray and Male 1981]. The net absorbed shortwave Q_{sw} radiation on the surface may then be determined from

$$Q_{sw} = (1-\alpha)\cdot Q_i \tag{13}$$

The spectrally integrated albedo may also be defined as

$$\alpha = \frac{\int_{\lambda_1}^{\lambda_2} R_{ef}(\lambda)\cdot I(\lambda)\cdot d\lambda}{\int_{\lambda_1}^{\lambda_2} I(\lambda)\cdot d\lambda} \tag{14}$$

where $R_{ef}(\lambda)$ is the spectral reflectivity and $I(\lambda)$ is the monochromatic intensity at wavelength λ [Gray and Male 1981, Pluss 1997]. The limits of integration λ_1, λ_2 are generally taken as 0.2 to 5 μm.

Pavement

Pavement is constructed by mixing a binder with aggregate to form a composite known as 'concrete' in the industry [Pomerantz et al. 1999]. A common binder is asphalt, a bituminous and black material. Asphalt is very poor reflector (e.g., an excellent absorber) of solar radiation. Newly paved surfaces where the asphalt significantly coats the aggregate tend to have an albedo of about 0.04 [Pomerantz et al. 1999]. Over time (5 to 10 yrs) actions by traffic wear the asphalt and expose more aggregate, which raise the albedo to a mean value of 0.12 $\pm$ 0.03 [Pomerantz et al. 1999]. Spectral reflectance measurements of asphalt binder by Pomerantz et al. [1999] suggest that asphalt concrete albedo is not highly wavelength dependent (i.e., its imaginary index of refraction would be independent of wavelength). Typical Portland cement concrete has an albedo near 0.35 [Pomerantz et al. 1999].

Snow

The optical properties of snow were reviewed in entirety by Warren [1982]. Snow albedo is dependent upon radiation wavelength (λ), zenith angle (°), grain size (μm) and light absorbing impurity concentration (Figure 5). A summary of parameters affecting snow albedo and emissivity of snow are in Table 3.

Grain size and zenith angle have a greater influence on snow spectral albedo in the near infrared [WWI, Warren 1982)], while the spectral reflectance of snow in the visual spectrum is sensitive to changes in impurity content and depth (for relatively thin snow) and weakly sensitive to changes in grain size and zenith angle [WWI, Warren 1982)]. Microwave emissivity is sensitive to all parameters but is not of concern for the model because it contributes such a small amount of energy compared to radiant solar energy (Table 1).

Table 3. Parameters affecting albedo and emissivity of snow. Reproduced from Table 2, Warren [1982].

	VIS Solar Albedo	NIR Solar Albedo	Thermal IR Emissivity	Microwave Emissivity
Grain size	(+)	yes		yes
Zenith angle	(+)	yes	yes	yes
Depth	yes			yes
Contaminates	yes			
Liquid water content				yes
Density				yes
Temperature				yes

The sign (+) means only if the snowpack is thin or impurities are present.

Spectral Albedo. The spectral reflectance of snow varies with wavelength of incident radiation, being very high (over 90%) in the visible and near-ultraviolet and low in the infrared [Warren 1984]. As a result, most solar irradiance absorbed by "pure" snow is in the NIR wavelengths. Ice is a strong absorber in the IR from 5 to 100 μm, a weak absorber in the VIS spectrum, with some strong absorption bands in the NIR between 0.8 and 1.5 μm [WWI, Warren 1982]. Maxima in snow reflectance are at 1.1, 1.3, 1.8 and 2.2 μm [WWI].

Zenith Angle. Snow albedo increases with zenith angle θ [WWI], as measured by Hubbley [1955], Bryazgin and Koptev [1969], Korff et al. [1974], LilJequist [1956] and

Rusin [1961]. Increases in θ raise albedo at all wavelengths, however, dependence is weaker in the visible (by only a few %) than in the near infrared (by as much as 20%) [WWI, Fig. 6., Warren 1982]. At small zenith angles (e.g. $\theta < 50°$, Petzold's [1977] rule-of-thumb) albedo is relatively independent of zenith angle, as supported by Wiscombe and Warren's theoretical work [WWI]. Surface irregularities may help reduce the influence of zenith angle to snow albedo at large angles because of shadowing at the surface from nonplanarity [WWI]. Also, at large zenith angles the direct radiation becomes dominated by diffuse sky radiation essentially reducing the effective zenith angle [Wiscombe and Warren's personal communication with M. Kuhn, WWI].

Cloud Cover. Cloud cover indirectly influences snow albedo (due to Mie scattering) by converting direct solar irradiance to diffuse thus changing the effective zenith cosine. It always raises the allwave albedo [WWI, Marshall 1989]. However, at large zenith angles ($\theta > 60°$) the spectral snow albedo is reduced by cloud cover which acts to lower the effective zenith angle (purely diffuse radiation has an effective zenith angle of 50°) [WWI, Fig. 12.]. The formation of clouds for zenith angles near 50° have relatively no influence on altering the spectral snow albedo, while cloud cover for $\theta \ll 50°$ tend to raise albedo a little [WWI, Fig. 12.]. Cloud cover also alters the spectral distribution of irradiance (e. g. it causes a spectral shift towards the visual spectrum, referred to as "visible-enrichment", [WW]) which tends to raise snow albedo and "acts counter to the zenith angle effect for $\theta > 50°$ " [WWI, Marshall 1989]. Wiscombe and Warren [WWI] state that the visible-enrichment effects usually win out. They sight numerous observations in agreement with their model.

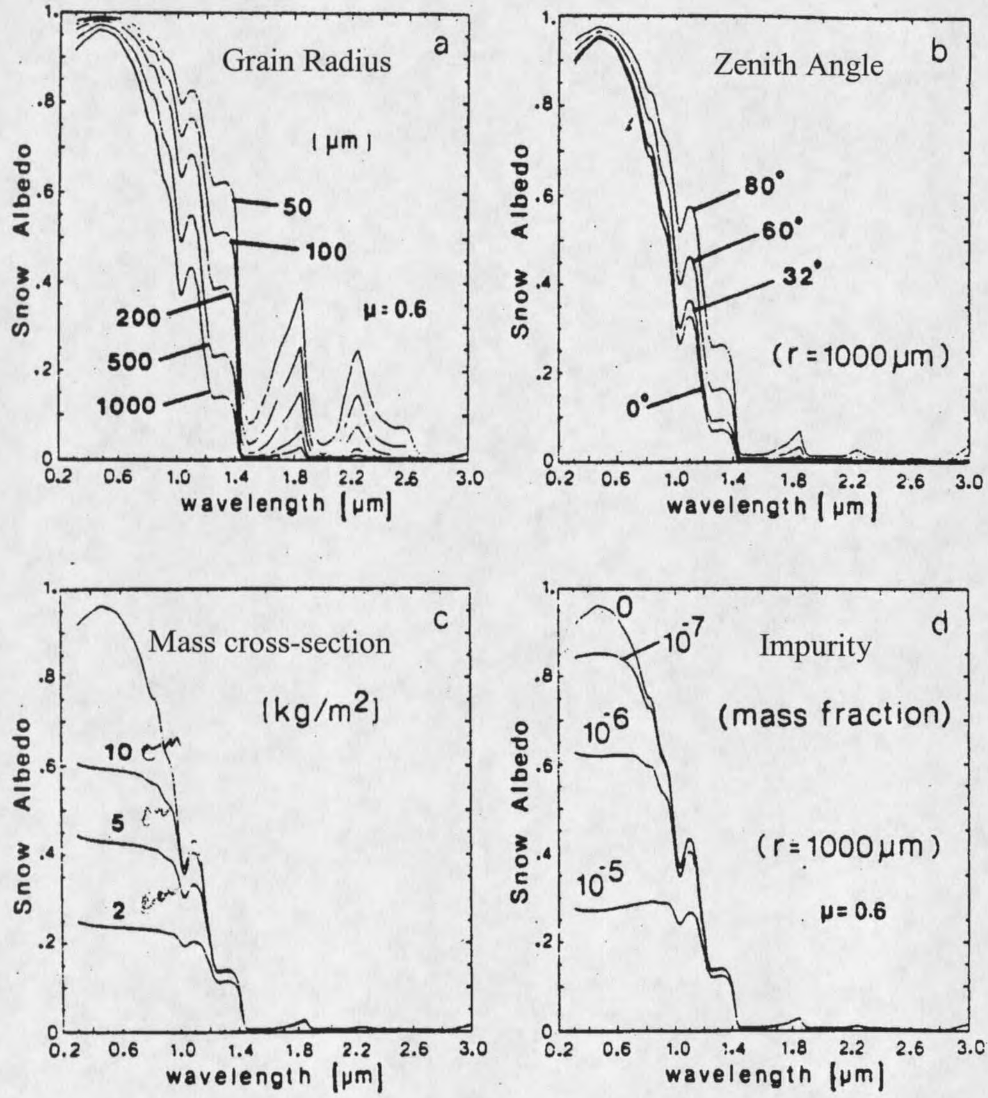

Figure 5. The influence of (a) grain radius, (b) zenith angle, (c) mass cross-section and (d) impurity concentration (soot) on the spectral albedo of snow. Reproduced from Figure 2.1, Marshall [1989].

Grain Size. Spectral snow albedo drops for all wavelengths as grain size increases [Warren 1982]. Absorption of photons (light ray) occurs within a snow grain and scattering occurs at the ice-snow interface [Warren 1982]. As grain size increases the optical path that the photon travels lengthens, raising its chances of it being absorbed between scattering opportunities at the grain boundaries and this acts to lower the snow albedo [Warren 1982, Marshall 1989]. The reduction of albedo due to grain size is greater in the NIR than in the VIS where ice is less absorbent (e.g. a smaller imaginary refractive index) in the VIS [WWI, Fig. 1., Marshall 1989].

The albedo of seasonal snow normally drops as it ages due in part to snow grain growth. An exception was observed by Liljequist [1956] at Maudheim, on a small ice shelf on the coast of Antarctica [Warren 1982]. He observed following a storm event that the snow albedo would increase after windstorms. Warren [1982] suggested that grain growth could have been slowed by the very cold temperatures and reduced by windstorms, which broke ice crystals effectively reversing metamorphism. Gravitational sorting of broken ice crystals might cause the smallest to settle out last and remain on the surface where they would strongly influence the albedo [Warren 1982]. Nakamura et al. [2001] experimentally confirmed that smaller grains have larger reflectances and that the uppermost layer of snow has the strongest effect on snow reflectance in the wavelength region 0.28 – 2.5 μm.

Liquid Water. Presence of liquid water in snow has little influence on VIS snow albedo [Warren 1982]. However, it has a stronger influence on the near infrared spectral reflectance [Warren 1982]. As now melts liquid water replaces air between snow grains, trapped by capillary action [Colbeck 1975; 1979; 1982; 1997, Sommerfeld and LaChapelle 1970]. The replacement of air by water between snow grains causes an increase the effective grain size, because the spectral index of refraction of water and ice are essentially equal for $\lambda > 0.5$ μm (e.g. about 0.9% difference at $\lambda = 0.589$ [Serway 1990, Table 35.1.]) [Warren 1982, WWI]. Refreezing of the liquid water changes the spectral albedo only slightly (only by a few percent at some near-infrared wavelengths [Fig. 5, Warren 1982]) due to differences in spectral imaginary index of refraction between water and ice [Warren 1982]. Also, as wet snow is refrozen the liquid water between grains freezes and probably maintains a similar shape to its liquid state creating no change to the effective grain size [WWI].

Light Absorbing Impurities. Snow albedo is highly sensitive to light absorbing contaminates, more so in the VIS region than in the NIR spectrum. New "pure" snow has negligible amounts of impurities and consists mainly of air and ice. Air and ice are not significantly absorptive in the visible spectrum and thus are highly transparent in the visible region. However, some common impurities found in seasonal snowcovers are very absorptive in the VIS spectrum. When present in the snow system the effect is to lower solar albedo. Very low concentrations of impurities (1 to 2 ppm) can reduce visible snow albedo by 1% (for new snow) up to 5% (for old melting snow) [WWII, Fig. 5.(a), (c)]. Higher concentrations have even greater effect.

As mentioned above, snow impurities lower the allwave albedo by primarily lowering the VIS snow reflectance (reduction in allwave albedo is about one-third that of visible [WWII]). Contaminates reduce reflectivity in the visible spectrum but have negligible effect in the near-infrared albedo and infrared emissivity because pure ice becomes more absorptive as solar wavelength increases from NIR to IR [Warren 1984]. In the IR region the spectral imaginary index of refraction of ice is much larger than the impurities for $\lambda > 5\ \mu m$ so no effect is noticeable [WWII, Warren 1984].

Many types of contaminates may enter snow to reduce abledo. The most common in seasonal snow are carbon soot, desert dust and volcanic ash [Warren 1984]. Of these, carbon soot is the most absorptive, about 50 times more absorptive than desert dust and about 200 times more absorptive than volcanic ash [Warren 1984]. Different impurities are more influential on roads and often are in larger concentrations than those found in season snowcovers because of highway maintenance operations.

The optical properties of snow impurities govern their effect on reducing snow albedos. The spectral imaginary refractive index m_{im} is an important optical property, which provides an index of the level of light absorption by the impurity. A common method to obtain m_{im} is to measure reflection and transmission spectra of highly polished thin slabs (~1 μm) prepared from the median, which requires extensive effort and is expensive. As a result, the aggregate optical properties of anti-skid abrasives employed in snow and ice control, which consist of a mixture of sand, clay and crushed rock materials have not been studied in detail. Salts effect on solar albedo (MgCl, a de-icing agent), which is added to the abrasives, are negligible given that sea salts are nearly transparent at solar wavelengths [WWII].

There are three primary impurity parameters that influence snow reflectance, these are concentration, mean size and spectral imaginary refractive index [WWII, p2737]. Allwave snow albedo drops as the concentration of absorptive impurities increases [WWII, Fig. 7.]. If the concentration of the impurities gets high enough the albedo will reach an asymptotic limit, e.g., the albedo of the impurities. Very large concentrations of contaminates on the surface can inhibit snowmelt by insulating the snow [Warren 1984]. Depths for debris to sufficiently insulate or have a significant effect on melt can vary, for "dirt" 5 to 10 mm, for desert sand 20 mm, and for volcanic ash 20 to 30 mm [Warren 1984].

The size and location of light absorbing contaminates in snow influence the albedo. Soot impurities internal to the snow grain have approximately twice the influence as an external mixture at reducing albedo (mean radius of soot is about 0.1 μm [Warren 1984]). Spatial influences of contaminates within the snowpack also applies to impurities with larger particulates (radius ~ 1 μm) such as dust [Warren 1984]. WWII showed that smaller particles are always better at reducing snow albedo than larger ones [WWII, Fig. 4.]. The size of the snow particles also dictates the influence of impurities. Wiscombe and Warren's spectral albedo model showed that for fixed concentrations of a contaminate (carbon soot) had a larger effect on lowering albedo for old snow ($r = 1000$ μm) than for new snow ($r = 100$ μm) [WWII, Fig. 5.]. This was attributed to the fact that solar radiation penetrates further into snow as grain size increases which increases the absorption opportunities by impurities between scattering opportunities by snow grains (WWII, Warren 1982).

For a fixed grain size and impurity concentration snow albedo will reach an asymptotic maximum as the snow depth increases. Wiscombe and Warren's (WWI) theoretical model showed that snow density only indirectly influences the snow albedo by raising the equivalent liquid-water depth of the snow layer.

Snow Depth. The spectral albedo of the underlying surface can affect the snow albedo for thin layers of snow. When light enters a snow layer, the majority of the NIR and IR are absorbed in the top layer [Marshall 1989]. However, visible light penetrates further into the snow through refraction and scattering and is absorbed only when it intercepts a light absorbing impurity or the underlying surface. As the snow depth decreases the probability of the visible light scattering to the bottom surface increases thus reducing the albedo. Reduction in snow depth reduces the albedo only in the visible region [WWII]. "Critical depth" refers to an optical depth of snow required for the snowcover to be optically semi-infinite and can vary greatly depending on the grain size, amount and type of absorbing impurities, solar zenith angle and the spectral composition of irradiance [Marshall 1989]. The critical depth is not a geometrical depth per se, but refers to an optical mass cross-section (kg/m^2, hereafter referred to as a "mass cross-section" of the medium) used to determine an optical path length x (m) to obtain complete attenuation of light. The path length x depends upon the volumetric density of the medium. For more detail see CHAPTER 2, Theoretical Model of Snow Albedo.

Critical depths for snow can range from 20 (for new snow) to 200 kg/m^2 (for old melting snow) in the VIS albedos (Marshall 1989). But critical depths for the NIR are thin (generally less than 10 kg/m^2) where snow is optically semi-infinite in the NIR region [WWI, Marshall 1989]. Table 4 is an attempt to demonstrate the large variability in geometrical depths exhibited by different density snow for arbitrary critical depths.

Table 4. Geometrical depth of snow on a surface for various densities of snow vs. arbitrary critical depths. The geometrical depth d_s is estimated from $d_s = C_d/\rho$ where C_d is the critical depth and ρ is the median density of the snow. LED refers to the liquid equivalent depth. The median density for each snow classification is estimated from Table 1, Maeno et al. [1988].

Critical Depth (kg/m^2)	Geometrical Depth of Snow d_s (cm)									
	New snow		Powder snow	Compacted snow			Grain snow		Slush	LED
	Dry	Wet		Dry		Wet	Dry	Wet		
				Soft	Hard					
	ρ 100 kg/m^3	ρ 150 kg/m^3	ρ 300 kg/m^3	ρ 375 kg/m^3	ρ 625 kg/m^3	ρ 600 kg/m^3	ρ 375 kg/m^3	ρ 550 kg/m^3	ρ 900 kg/m^3	ρ 1000 kg/m^3
5	5.0	3.3	1.7	1.3	0.8	0.8	1.3	0.9	0.6	0.5
10	10.0	6.7	3.3	2.7	1.6	1.7	2.7	1.8	1.1	1.0
15	15.0	10.0	5.0	4.0	2.4	2.5	4.0	2.7	1.7	1.5
20	20.0	13.3	6.7	5.3	3.2	3.3	5.3	3.6	2.2	2.0
25	25.0	16.7	8.3	6.7	4.0	4.2	6.7	4.5	2.8	2.5
30	30.0	20.0	10.0	8.0	4.8	5.0	8.0	5.5	3.3	3.0
35	35.0	23.3	11.7	9.3	5.6	5.8	9.3	6.4	3.9	3.5
40	40.0	26.7	13.3	10.7	6.4	6.7	10.7	7.3	4.4	4.0

The underlying surface can have the opposite effect on snow albedo. If the visible albedo of the base surface is higher than the asymptotic limit of the snow albedo it can act to increase the snow albedo as the optical mass cross-section drops below the critical depth. However, this is never the case for snow on roads because common pavement materials are highly absorptive in the visible region. Absorptive impurities can also have the same effect generally only raising the spectral albedo in the NIR wavelengths [WWII, Fig. 5. (c)]. This is the case if the spectral imaginary refractive index of the contaminate dominates that of snow in the NIR region, e.g., essentially the bulk m_{im} of snow and contaminates approaches the m_{im} of the impurity at high concentrations of the impurity [WWII].

Theoretical Model of Snow Albedo

There are a number of theoretical snow reflectance models developed which are commonly based on radiative-transfer theory [Warren 1982, Sergent 1998]. A full review of radiative transfer models regarding snow reflectance has been given by Wiscombe and Warren [WWI] and Warren [1982]. In these models snow grains are represented as spheres that scatter in each others far-fields (scattering in the far-field assumes particles are sufficiently separated that there geometrical cross-sections perpendicular to incoming light rays do not lie in the shadow of other particles). The single-scattering parameters are derived from Mie theory [Sergent 1998]. Multiple-scattering which occurs in the entire snowpack is simulated from the single-scattering parameters by different methods [WWI, Warren 1982, Sergent 1998]; the *two-stream* approximation, Dunkle and Bevans [1956], Giddings and LaChapelle [1961] (neither of these studies explicitly compute scattering by individual grains to set up the two-stream approximation, but instead are found by fitting experimental data [Warren 1982]), and

Bohren [1987]; the *delta-Eddington* approximation, WWI, WWII, and Choudlhury and Chang [1979a, b, 1981]; the *discrete-ordinate* method, Stamnes et al. [1988]; the *adding-doubling* method, Sergent et al. [1998], Aoki et al. [1999], and Aoki et al. [2000].

The albedo model used in this thesis is adapted from the spectrally integrated parameterization of Marshall [1989], which is based on the theoretical model of Wiscombe and Warren [WWI, WWII]. As a result, the radiative transfer theory upon which this thesis is based is from the theoretical snow reflectance model of Wiscombe and Warren [WWI, WWII].

The radiative transfer model of Wiscombe and Warren [WWI, WWII] is applicable to snowcover conditions found on roads because it applies a physical approach and includes most of the factors of concern, such as grain size, thin snowcovers and impurity influences. The theoretical model accounts for single-scattering by snow grains using Mie theory, accurate at all wavelengths, and multiple-scattering by using the delta-Eddington approximation, which can handle extreme anisotropic scattering by snow grains [WWI and WWII]. The theoretical model is dependent upon realistic physical parameters and agrees well with recorded observations of spectral snow albedo [WWI, WWII]; the model depends on the following physical parameters [taken from WWI, pg 2715]:

$m(\lambda)$	complex refractive index of ice
λ	wavelength (μm)
r	mean snow grain radius (μm)
μ_0	cosine of solar zenith angle θ

d_f ratio of diffuse incident flux to total (direct and diffuse) incident flux

m_{xs} optical mass cross-section of water mass in the snowpack (kg/m^2)

α_g albedo of surface beneath snow

m_{xs} is obtained from ρd_s, where ρ is the snow density (kg/m^3) and d_s is snow depth (m). The optical snow depth (it represents the degree of exponential attenuation in the medium of the form $I = I_o \exp(-\tau_o)$) is obtained as,

$$\tau_o = N \cdot \sigma_e \cdot x = \frac{m_{xs} \cdot \sigma_e}{\frac{4}{3} \cdot \pi \cdot r^3 \cdot \rho_{ice}} = \frac{3 \cdot m_{xs} \cdot Z_e}{4 \cdot r \cdot \rho_{ice}} \quad (15)$$

where, for a sphere

$$N = \frac{1}{\frac{4}{3} \cdot \pi \cdot r^3} \quad (16)$$

and

$$\sigma_e = \pi \cdot r^2 \cdot Z_e \quad (17)$$

N is the number density of spherical snow grains (m^{-3}), σ_e is the extinction cross-section (m^2) and x is the optical path length, taken as the equivalent depth of bubble free ice (ρ_{ice}= 917 kg/m^3). The product of $N \cdot \sigma_e$ represents the attenuation coefficient of the medium (m^{-1}).

Ice particles are assumed to scatter as optical spheres and that each sphere scatters in each other's far-field [WWI]. This assumption is shown to be valid in the solar spectrum for both low and high density snow, the later is more common on well traveled roads [WWI]. Also, the sphericity assumption is adequate for modeling groups of nonspherical particles, as argued by WWI the effects of nonsphericity are small in relation to effects from grain size variation [Warren 1982].

Light absorbing impurities are accounted for through the complex refractive index. "Mie calculations are done separately" for the contaminate and the "ice particles and then averaged together using respective cross-sectional areas per unit volume as weight factors" [WWII]. Light absorbing impurities are assumed uniformly distributed as an external mixture among the snowcover as spheres with an arbitrary radius (0.1 μm). The external mixture assumption would be valid for snow and sand particles mixing on the road. The assumed radius of the impurities inherent in the parameterized model introduced below, is much smaller than the actual radius of sand impurities on the road, thus the differences in particle size must be accounted for when determining the effective mass fraction of the sanding contaminates, see CHAPTER 3, section, Validation of the computational albedo routine, heading, Determining the effective soot content in the model.

The theoretical model [WWI and WWII] requires extensive calculations to obtain albedo. Use of such a model in thermal mapping of complex terrain is extremely time consuming and inefficient because of the large amounts data required for mathematically involved calculations. It is therefore necessary to simplify the theoretical model to speed calculations through a parameterization of albedo.

Parameterization of Snow Albedo

There are a variety of published albedo parameterizations that have been published that are based on a broad range of inputs. However, these simplified models are usually derived from sight specific data (primarily for seasonal snowcovers) and are not directly transferable to other locations. For thermal modeling of terrain and pavements, using models such as WinThermRT, a more universal albedo model is required because albedo is extrapolated over an expansive and complex topographical grid. It would be impossible and economically unfeasible to parameterize albedo over the entire terrain grid using measurements at each sight. Thus, a parameterization of albedo that is developed from a physical standpoint and is computationally efficient is required.

This thesis selected the parameterization of albedo of Marshall [1989] on which to base the snow-on-slab albedo model, because it satisfies the above requirements. Marshall [1989] simplified the sophisticated theoretical spectral snow albedo model of Wiscombe and Warren (WWI, WWII) for use in GCMs. The parameterized albedo model (SNOALB) of Marshall [1989] combines the effect of similar variables on albedo. The advantage is a simplified model that increases computational efficiency, but is transferable to any location because it is still dependent on realistic physically based parameters. However, some accuracy is sacrificed in the calculations because of the parameterizations [Marshall 1989].

The optical influences of light absorbing impurities in the parameterization are modeled after carbon soot [Marshall 1989, WWI, WWII]. When other contaminates are present, such as on roads, they are normalized to soot before input into the model.

The optical mass cross-section of the snowcover is used in the parameterization of albedo only when it is not semi-infinite, e.g., when the mass cross-section is less than the critical depth for the physical snowcover (remember the critical depth is a function of the geometrical snow depth, impurity concentration and effective grain size). For thin snow layers the albedo will lie between the deep snow albedo and the underlying surface albedo. When this is encountered in the model, the VIS and NIR albedos are linearly interpolated between the theoretical minimuam α_{min} and maximum α_{max} albedos for the given snow conditions. α_{min} represents the minimum effective snow depth to reach within 1% of the underlying surface albedo, and α_{max} represents the maximum effective snow depth to reach within 1% of the semi-infinite snow albedo [Marshall 1989].

SNOALB requires as input values the optical mass cross-section of the snow, zenith cosine, atmospheric surface pressure, atmospheric transmittance, soot fraction, diffuse fraction and snow grain radius. As output the parameterization calculates the shortwave, VIS and NIR albedos. A wavelength selection option allows the user to choose between 0.7 or 0.9 μm as the separation point between NIR and VIS albedos.

Parameters

The following summarizes the albedo parameterization of Marshall [1989]. The parameters were statistically fit to spectrally integrated albedo data generated by the theoretical model of spectral snow albedo [WWI, WWII]. During generation of data, the model assumed entirely diffuse radiation. Marshall's [1989] model minimized the number of predicting variables yet maintained the physical dependence of the theoretical model. For more details see Marshall [1989] and WWI and WWII.

The four principal factors influencing snow albedo identified by Wiscombe and Warren [WWI, WWII] and parameterized by Marshall [1989] are zenith angle, impurity content, grain size and the optical mass cross-section. Their effects on spectrally integrated visible and near-infrared albedo can be seen in Figure 6 [Reproduced from Fig. 2.2, Marshall 1989]. The influence of zenith angle on snow albedo could be mimicked by increasing grain size and a reduction in the optical snow mass cross-section mimicked by increasing soot content. Therefore, similar effects of each pair were combined into two parameters: effective grain size and effective soot.

Effective Grain Size Parameter. The similar influence of grain size and zenith cosine is shown in Figure 6 (a) and (b). Albedo is more sensitive to changes in grain size r than in zenith cosine. Thus, influences on snow albedo of the two were combined into an effective grain radius, r_{eff} [Marshall 1989].

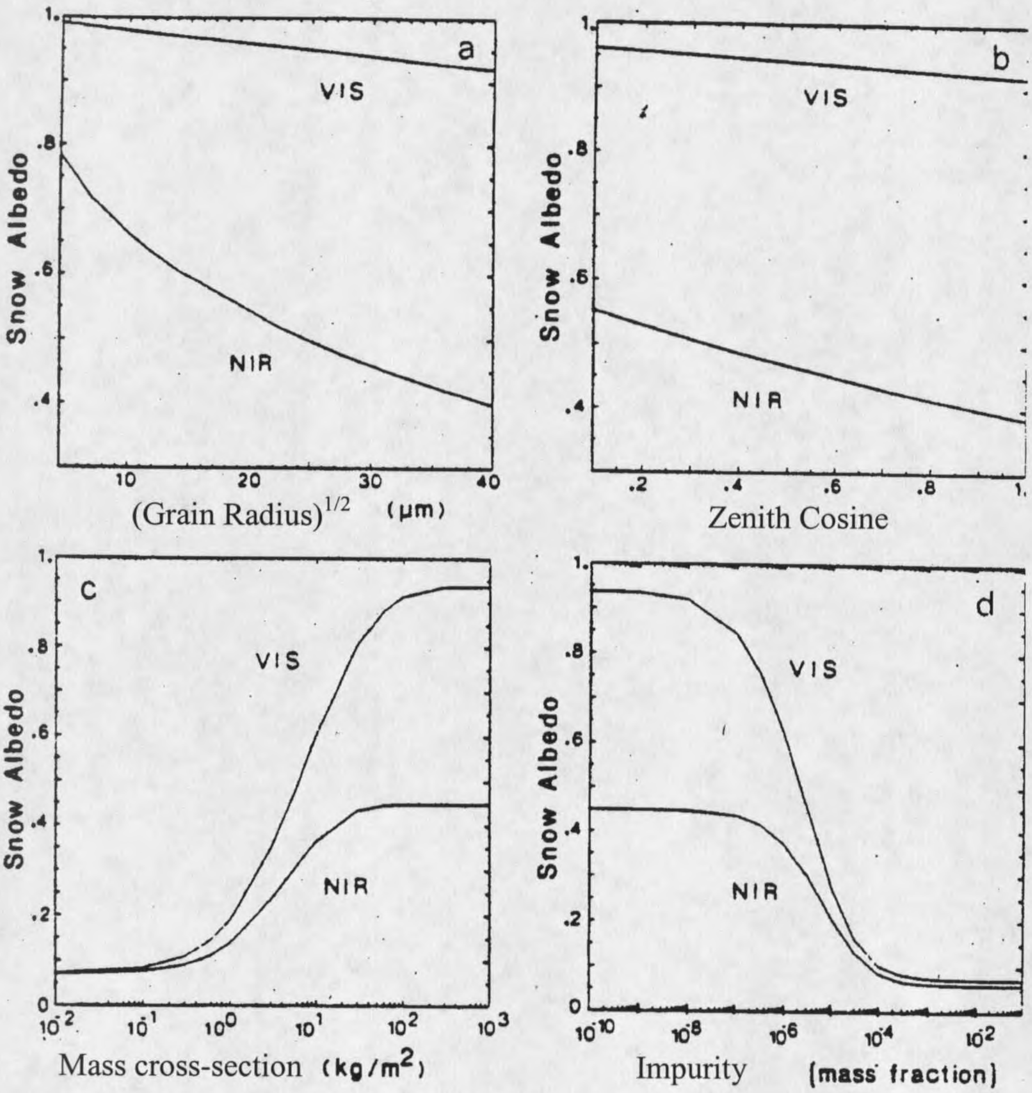

Figure 6. The influence of (a) snow grain size, (b) solar zenith cosine, (c) snow mass cross-section and (d) impurity concentration of carbon soot on the spectrally integrated VIS (0.3 – 0.7 μm) and NIR (0.7-3 μm) snow albedo. The effective snow grain radius r is 1000 um which represents old melting snow [Warren 1982]. Reproduced from Figure 2.2, Marshall [1989].

The zenith angle was correlated to the square-root of the grain size. The zenith angle of diffuse radiation μ_d was used as the reference. $\Delta\mu$ represents the difference in zenith cosine μ_o from μ_d. The effective grain radius, r_{eff}, was defined as,

$$r_{eff} = \sqrt{r} + \Delta\mu \cdot \left(\frac{\sqrt{r}}{b} \right)^2 \tag{18}$$

values for the slope b are in Table 5.

Table 5. Values of slope used to estimate an effective grain radius in equation (18). Reproduced from Table 2.2, Marshall [1989].

	VIS 0.7	NIR 0.7	VIS 0.9	NIR 0.9
b	1.281	1.264	1.307	1.204

Effective Soot Parameter. As mentioned above, carbon soot and the optical mass cross-section show similar influence to the spectrally integrated snow albedo (Figure 6). Both an increase in soot and a decrease in the optical mass lower snow albedo. The effect is strong in the VIS and weak in the NIR where snow is more absorptive. As a result, the effect of soot and the mass cross-section were combined into an effective soot parameter by Marshall [1989].

Marshall [1989] reported an inverse nonlinear relationship between soot and the mass cross-section. The relationship was reduced to linear by applying a log transform. Additional dependence of the intercept a and the slope b on the underlying surface albedo α_g were expressed as a function of α_g using a least-squares fit,

$$a = a' + b' \cdot \alpha_g \tag{19}$$

$$b = c' + d' \cdot \alpha_g + e' \cdot \alpha_g^2 \qquad (20)$$

with coefficients a', b', c', d' and e' are in Table 6.

Table 6. Values of coefficients from equation (19) and (20) for VIS and NIR spectral regions. Reproduced from Table 2.3, Marshall [1989].

	VIS 0.7	NIR 0.7	VIS 0.9	NIR 0.9
a'	-13.64	-13.79	-13.78	-13.62
b'	-2.33	-2.74	-1.89	-1.83
c'	-1.24	-1.34	-1.28	-1.30
d'	0.57	0.90	0.67	1.35
e'	-0.43	-1.54	-0.50	-2.19

To combine soot and the mass cross-section into an effective parameter, d_s was converted into an equivalent soot concentration S':

$$\ln(S') = a + b \cdot \ln(d_s) \qquad (21)$$

rewriting,

$$S' = e^a \cdot d_s^{\ b} \qquad (22)$$

where a and b are coefficients from equations (19) and (20) above. The effective soot, S_e is simply the sum of S' and the true soot concentration S,

$$S_e = S + S' \qquad (23)$$

Atmospheric Transmittance. Marshall [1989] used the atmospheric model of Wiscombe et al. [1984], ATRAD, to generate values of solar, visible and near-infrared transmittance under several conditions of cloud cover. The sky cover ranged from clear to thick overcast skies and zenith cosine μ was varied from 0.2 to 0.6 (θ ~78° to 53°).

Marshall [1989] formed a parabolic relationship between solar transmittance, t(solar) and divisions near-infrared and visible,

$$t = a \cdot t(solar) + b \cdot (t(solar))^2 \tag{24}$$

where coefficients are in Table 7 and the value t(solar) refers to visible or near-infrared transmittance.

Diffuse Fraction Parameter. Marshall [1989] obtained the diffuse fraction d as a function of atmospheric transmittance t. A diffuse fraction of 1 means that all radiation is scattered out of the direct solar beam. Marshall [Fig. 2.11, 1989] found the following relationship for visible and near-infrared diffuse fraction d_f,

$$d_f = d_c + b \cdot (t - t_c) \qquad 0 \leq d_f \leq 1 \tag{25}$$

where d_c is the diffuse fraction for clear sky and t_c is the atmospheric transmittance for clear sky. The slope b is a function of zenith cosine μ_0 and defined as,

$$b = f' + g' \cdot \mu_o \tag{26}$$

where values f' and g' are given in Table 7.

Table 7. Values of the coefficients a and b in equation (24) f' and g' in (26) and c and k in (28) for VIS and NIR spectral regions. Reproduced from Table 2.4, Marshall [1989].

	VIS 0.7	NIR 0.7	VIS 0.9	NIR 0.9
a	1.571	0.425	1.506	0.058
b	-0.572	0.575	-0.506	0.941
f'	-0.339	-0.297	-0.342	-0.248
g'	0.470	0.294	0.459	0.190
c	0.446	0.063	0.345	0.250
k	-0.389	-0.169	-0.414	-0.004

The clear sky diffuse fraction d_c is obtained from Bouger's law, equation (2) under the assumption that the diffuse fraction is proportional to the amount of radiation removed from the direct beam,

$$d_c = \frac{c \cdot (I_0 - I)}{I_0} \tag{27}$$

where c is a proportionality constant. The clear sky diffuse fraction becomes,

$$d_c = c \cdot \left[1 - e^{(-k_e \cdot x)}\right] \tag{28}$$

where x is the optical path length (relative air mass) and c and k are listed in Table 7.

The clear sky near-infrared transmittance t_c is modeled using a power law as,

$$\ln(t_c) = a \cdot x^b \cdot \frac{p}{p_0} \tag{29}$$

where p and p_0 are the surface and sea-level atmospheric pressures, respectively. Coefficients are in Table 8.

The clear sky visible transmittance t_c is given by [Marshall 1989],

$$t_c = 1 - c \cdot x \cdot e^{\left[d_f \cdot \left(1 - \frac{p}{p_0}\right)\right]} \tag{30}$$

where again x is the relative air mass and coefficients are in Table 8.

Table 8. Values for the coefficients a, b, c and d in equation (29) and (30) for spectral regions VIS and NIR. Reproduced from Table 2.5, Marshall [1989].

	VIS 0.7	NIR 0.7	VIS 0.9	NIR 0.9
a		-0.257		-0.396
b		0.306		0.238
c	0.054		0.040	
d	-0.400		-0.800	

Snow Albedo Parameterization

To calculate semi-infinite integrated albedo under a clear sky, two parameters are required, effective soot S_e and effective grain size r_{eff}. When cloud cover is present, which only affects the NIR albedo, a value of the atmospheric transmittance is required.

Clear Sky Albedo. Marshall [Fig 2.17, 1989] divides albedo between two limiting values: a high (clean snow) albedo α_h and a low (dirty snow) albedo α_1. α_1 is dependent upon only soot while α_h depends on snow grain radius as well. The parameterization for visible and near-infrared albedo under clear sky is calculated by,

$$\alpha = \alpha_h - (\alpha_h - \alpha_2) \cdot e^{\left(-k_h \cdot \ln\left(\frac{S_2}{S}\right)\right)} \qquad S < S_2 \tag{31}$$

$$\alpha = \alpha_1 - (\alpha_2 - \alpha_1) \cdot e^{\left(-k_1 \cdot \ln\left(\frac{S}{S_2}\right)\right)} \qquad S > S_2 \tag{32}$$

where α is the integrated snow albedo that lies between α_h and α_1 based on some soot and grain size value and $(\ln(S_2), \alpha_2)$ are the inflection points between the two divisions [Marshall 1989]. The inflection points are defined as,

$$\alpha_2 = \frac{\alpha_h + \alpha_1}{2} \tag{33}$$

$$\ln(S_2) = e + f \cdot \ln(\sqrt{r}) \tag{34}$$

where r is the grain size and values for the coefficients e and f are in Table 9. α_h for visible and near-infrared spectral regions is expressed as,

$$\alpha_h(VIS) = a + b \cdot \sqrt{r} \tag{35}$$

$$\alpha_h(NIR) = c + d \cdot \ln(\sqrt{r}) \tag{36}$$

The slope k_h is calculated from,

$$k_h(x) = k_{h1}(x) + k_{h2}(x^2) \qquad with: x = \ln\left(\frac{S_2}{S}\right) \tag{37}$$

where values for k_{h1}, k_{h2} and k_1 are in Table 9.

Table 9. Values for the slopes k_{h1}, k_{h2} and k_1 in equations (32), (33) and (38), coefficients a, b, c and d from (36) and (37), and coefficients e and f from (35). Reproduced from Table 2.6 and 2.7, Marshall [1989].

	VIS 0.7	NIR 0.7	VIS 0.9	NIR 0.9
k_{h1}	0.450	0.580	0.450	0.800
k_{h2}	-0.040	-0.040	-0.040	-0.120
k_1	0.464	0.482	0.474	0.539
a	0.9988		0.9952	
b	-0.0020		-0.0034	
c	1.0670		0.9832	
d	-0.1811		-0.2161	
e	-6.3550	-5.9328	-6.3914	-6.0302
f	-1.9752	-1.8102	-1.9194	-1.5541

Near-Infrared Albedo Under Cloudy Skies. Changes in atmospheric transmittance alter the near-infrared albedo. The parameters assume all incident radiation is diffuse. A change in albedo from clear sky is related to atmospheric transmittance through

$$\alpha_{cld} = \alpha_c + b \cdot (t_{cld} - t_c) \tag{38}$$

where c and cld designate clear and cloudy sky albedo. The slope b depends only on soot by,

$$b = a' + b' \cdot \ln(S) + c' \cdot \ln(S)^2 \tag{39}$$

where values for a', b' and c' are Table 10.

Table 10. Values of the coefficients a', b' and c' in equation (39), and a, b and c in equation (41). Reproduced from Table 2.8, Marshall [1989].

	NIR 0.7	NIR 0.9
a'	0.3953	0.1060
b'	0.0637	0.0243
c'	0.0017	0.0005
a	0.0016	-0.0020
b	-0.0158	0.0141
c	0.0462	0.0372

Extension of Near-Infrared to 5 μm. The parameterization extends the near-infrared albedo from 3 to 5 μm. Wavelengths from 3 to 5 μm account for 0-2% of near-infrared downflux and depend on atmospheric transmittance. So Marshall [1989] adjusted the parameterization to obtain the near-infrared albedo more accurately by including wavelengths above 3 μm and up to 5 μm. The adjusted near-infrared albedo A_{nir} is obtained as a weighted average of the near-infrared ($\alpha_{nir3} < 3\ \mu m$) and the near-infrared albedo from 3 to 5 μm (α_{nir3-5}) as,

$$\alpha_{cld} = f_{3-5} \cdot \alpha_{nir3-5} + (1 - f_{3-5}) \cdot \alpha_{nir3} \quad (40)$$

where f_{3-5} is the fraction of near-infrared flux from 3 to 5 μm defined as a non-linear function of atmospheric transmittance t as,

$$f_{3-5} = a + b \cdot t + c \cdot t' \quad (41)$$

Values for a, b and c are obtained from Table 10.

Snow on Roads

Winter Maintenance Practices

As commerce and personal mobility became more and more dependent on rubber-tired motor vehicles, beginning with the advent of the automobile, anti-snow and ice operations became necessary to provide safer and less hindered mobility during winter months. Current practices largely evolved through experience and vary from state to state and even between a state's internal transportation departments [Hanbali 1965, Coulter 1965, Personal communication with Maurice DeDycker, Division Maintenance Supervisor, and crew members, MDT-Bozeman]. Anti-snow and ice operations directly influence the physical properties of snow and ice on roads, which control snow albedo. Thus, maintenance practices play an important role on snow albedo.

Maintenance of the I-90 corridor is divided between Bozeman and Livingston MDT winter maintenance crews. Bozeman's winter route extends a few miles east of Bozeman Hill, thus winter maintenance practices of concern are those of the MDT-Bozeman.

Snow may be artificially removed from a road by chemical, mechanical and thermal means. To remove large quantities of snow mechanical methods are most cost effective and widely utilized. The majority of these can be classified as displacement (blade) plows and rotary plows [Gray and Male 1981]. MDT-Bozeman employs only blade snowplows equipped with abrasive dispensers through the research corridor [Personal communication with Maurice DeDycker, MDT-Bozeman].

Displacement snowplows are not completely effective at removing all snow from the road; residual snow commonly is left behind. The snow removal effectiveness is strongly dependent upon the physical properties of the snow (e.g. density, liquid water content, strength, bonding to the pavement surface, etc.). In the case of very dense snow well bonded at the snow-pavement interface plows are usually ineffective at removing snow, requiring other means of removal such as solar influences and anti-icing chemicals [Gray and Male 1981]. Most studies have focused on snow removing performance and efficiencies [Gray and Male 1981]. No studies were found that developed methods to determine mass of snow removed from the road, which would be useful in modeling albedo.

Thermal methods that use pavement heating systems or "in situ melting systems" to remove snow and ice from the road are not commonly employed on a large scale because of the high cost of installation and operation [Gray and Male 1981]. Remote locations and high mountain passes common to rural highways where ice and snow are of greater risk further make thermal methods less desirable. Hence, "in situ melting systems" are not employed within the research corridor.

Anti-icing chemicals used to control snow act to lower the freezing temperature of water [Coulter 1965]. They help prevent the formation of ice films, weaken the bond between snow and pavement, melt new snow on the road, or melt residual snow left behind by plowing [Gray and Male 1981]. Salts and dicers suppress the vapor pressure of ice thus lowering the freezing temperature of water. Commonly they are wetted into anti-skid abrasives ("sanding" materials) to help the sanding materials seat into the ice or compacted snow before actions by vehicles can whisk it off. Direct application of the liquid is also common. Calcium chloride CaCl, magnesium chloride MgCl and sodium chloride NaCl are three typical chemicals.

Liquid anti-icing chemicals (apart from sanding materials wetted with MgCl) are typically not used through the I-90 corridor by MDT-Bozeman crews. The sand pile is pre-wetted with MgCl to help keep it from freezing and at times sand is injected with MgCl as it is dispensed on the road to help it seed into the ice [Personal communication with Maurice DeDycker, Division Maintenance Supervisor, MDT-Bozeman]. Generally, about 7-10 gallons of MgCl is used per cubic yard of sand [Maurice DeDycker]. However, some additional random infrequent uses do occur when de-icing chemicals are applied directly. This is typically done by Livingston MDT crews when lengthening their route to provide assistance to MDT-Bozeman [Personal communication with Maurice

DeDycker]. No direct application of liquid anti-icing chemicals were observed for the days studied.

Anti-skid abrasives are used to increase the sliding friction at the tire-snow interface. MDT-Bozeman uses an aggregate sand mixture containing various minerals and crushed rocks from local quarries. Their sanding materials are held to an aggregate mixture as outlined in Table 11. The mixture usually varies depending on which contractor wins the bid.

Table 11. Gradation of sanding aggregate. Montana test method MT-202.

Sieve	Percentage passing
3/8	100
4M	40-80
10M	-
40M	0-40
200M	0-10
PI	NP

As stated previously, application of the abrasives again is driver and storm dependent. Application rates are regulated by engine RPMs and the opening width of the dispensing gate, which do not work properly on all of the sanding trucks used by the MDT-Bozeman [personal communication with Maurice DeDycker and crew members, MDT-Bozeman]. Combined with driver judgment and storm variability, application rates can be extremely variable. However, corners, grades and overpasses are typically sanded more heavily than horizontal straight sections [personal communication with Maurice DeDycker and crew members, MDT-Bozeman]. To generalize sanding rates at a single value, DeDycker implied that sanding materials are spread about 1 cubic yard per highway lane mile [personal communication with Maurice DeDycker, MDT-Bozeman].

Vehicle Influences

Actions by vehicles and winter maintenance practices indirectly affect snow albedo by directly altering the structure of snow through non-uniform mechanical mixing, compaction, movement and removal of snow. Thus, knowledge of traffic volumes passing the research area is necessary to model the physical snow properties and hence albedo on the road.

Vehicle movements assist in the removal of snow [Coulter 1965, Schaerer 1970]. Schaerer [1970] reported that for snow having a free-water content FWC of 30% (slush) or more snow was readily removed by the actions of traffic. Schaerer also observed that with a FWC of less than 15%, snow was compacted by passing vehicles, and for FWCs residing between 15% to 30%, the snow "remained uncompacted on the road in a soft, loose state" [Schaerer 1970]. Other findings show that having a vehicle density greater than 30 vehicles per hour can reduce the amount of chemicals needed. Only about 30% to 50% of ice needs to be melted so that the remaining slush can be thrown off the road by passing vehicles.

Vehicle traffic also influences the physical structure of snow on roads. Traffic breaks snow crystals, which reduce their optical size, mixes in VIS light absorbing contaminates and contributes to the high anisotropy of snow coverage over the road [Minsk 1965, Yong and Fukue 1977, Naruse et al. 1988, Maeno et al. 1988]. Cars can also supply thermal heat to the snow surface through thermal emittance and mechanical actions [Ishikawa et al. 1999]. Coulter [1965] indicated that tire friction adds heat to the surface. Maeno et al. [1987] observed inhomogeneous melting of snow by rapid acceleration of vehicles while climbing steep grades. But generally at highway speeds, thermal heat emitted by vehicles was shown to be insignificant [Ishikawa et al.1999].

Characteristics of Snow on Roads

The physical properties of snow on roads differ greatly from seasonal snowcovers in thickness, density, ablation rate, metamorphism and impurity content. An important characteristic of snowcovers on roads is their inhomogeniality, which is caused by frequent melt-freeze cycles and constant irregular mixing and redistribution of snow by vehicles and winter maintenance operations.

The low surface albedo of pavement combined with effective re-radiation of thermal energy at night can create large diurnal surface temperature fluctuations on roads. As a result, snowcover on roads can undergo rapid changes in its physical structure. Powder snow on the road surface in the morning can turn to slush and melt completely from the road by afternoon. Wet snow present in the evening may refreeze immediately after the sun sets, strengthening its bond to the pavement surface, hindering removal efforts [Minsk 1965, Gray and Male 1981]. If snow is present on the road for some period of time, as in colder regions, it may under go successive diurnal thaw and refreeze cycles.

Coupled with the actions of motor vehicles and winter maintenance (such as mechanical breakage and redistribution) a very thin highly anisotropic snow structure may form [Maeno et al. 1988]. As a result, snow albedo modeling on roads is complicated since various types of snow and ice may exist simultaneously on a road as determined by specific meteorological and traffic conditions.

Work to understand and determine the physical structure of snow on roads was largely undertaken to assist winter maintenance operations in snow and ice control [Minsk 1965]. Early work on snow density, temperature, hardness, and water content on roads was summarized by Minsk [1965].

More recently, Maeno et al. [1988] classified snow on roads by generalizing attempts given by Kinosita et al. [1969, 1970] and Aoki et al. [1977]. Kinosita et al. focused on snow in colder regions and Aoki studied snow in warmer regions. Meano et al. [1988] grouped snow into type and sub-type by warm and cold regions. Seven types were used: new-snow, compacted-snow, powder-snow, grain-snow, slush, ice-crust and ice-film with five types (all except powder-snow and slush) divided into sub-groups for liquid water content (dry or wet), compacted snow was sub-divided into hard and soft. The new classification given in Table 12 allows the observer to distinguish the physical structural of snow and ice through visual confirmation [Maeno et al. 1988].

Snow densities on roads are higher than natural snow densities and generally increase due to motor vehicle actions [Maeno et al. 1988, Fig. 5.]. Repeated passes of traffic forms ruts in the snow tire tracks. Densities in ruts reached 500-700 kg/m^3 and were higher than snow densities outside of the ruts. Maeno et al. [1988] also found that densities within tire ruts fluctuate greatly due to redistribution of snow from passing vehicles.

Only limited traffic volumes are required to reach high snow densities observed on roads, with the largest and most rapid changes in densities occurring with newly deposited snow. Maeno et al. [1988] found that a relatively few passes (veh<10) of vehicles were needed to raise snow densities from 69 kg/m^3 to around 400 kg/m^3 in the tire tracks.

Table 12. Classification of snow and ice on roads. Reproduced from Table 1, Maeno et al. [1988].

Type	Sub-type		Density (kg/m^3)	Hardness ($x10^4$ kg/m^2)
New snow	Dry new snow		~100	~0
	Wet new snow		100~200	
Compacted snow	Dry compacted snow	Soft	250~500	10~50
		Hard	500~750	50~200
	Wet compacted snow		400~800	10~50
Powder snow	Powder snow		200~400	~0
Grain snow	Dry grain snow		250~500	~0
	Wet grain snow		400~700	
Slush	Slush		800~1000	~0
Ice-crust	Dry ice-crust		>750	90~300
	Wet ice-crust			
Ice-film	Dry ice-film		>800	-
	Wet ice-film			

Vehicles can also act to reduce the hardness of compacted snow. Meano et al. [1988] observed the rapid reduction in snow hardness for melting wet compacted-snow (near

0°C) due in part to accelerated melting and erosion by passing vehicles. Naruse et al. [1988] also observed accelerated ablation rates from traffic. But thermal energy available for melting coupled with vehicle actions is not the sole mechanism to reduce the hardness of compacted snow on roads, chemical contamination and mechanical mixing and erosion from traffic also effect snow hardness. At temperatures below freezing chemical and mechanical actions can still reduce snow hardness when melting is not as influential [Maeno et al. 1987]. However, this happens at a slower rate than when melting is present [Maeno et al. 1988].

CHAPTER 3

METHODOLOGY

Within this chapter instrumentation used to measure data for the thesis is discussed. The second section gives an overview of the snow-on-slab albedo model. Appendix A contains source code for the snow-on-slab albedo model.

Instruments and Observations

Measurements and observations were performed during the months of January through May 2001. Measurements of meteorological (MET) data were continuous over the period. Observations were made only on days when snow fell and accumulated on the road. A total of 19 of days were observed. Over the period, traffic data were recorded continuously, excluding intermittent periods required to down load data and recharge the data logger.

An MDT RWIS was used to collect meteorological data at the site (Figure 7). The RWIS is located approximately 30 m from the highway up on an embankment. All sensors except for the surface temperature sensor (positioned on the road surface) were located at the RWIS tower. Data collected from the RWIS was assumed to be near enough to the road to minimize spatial differences between the highway and the tower. Data were sampled every 3 minutes.

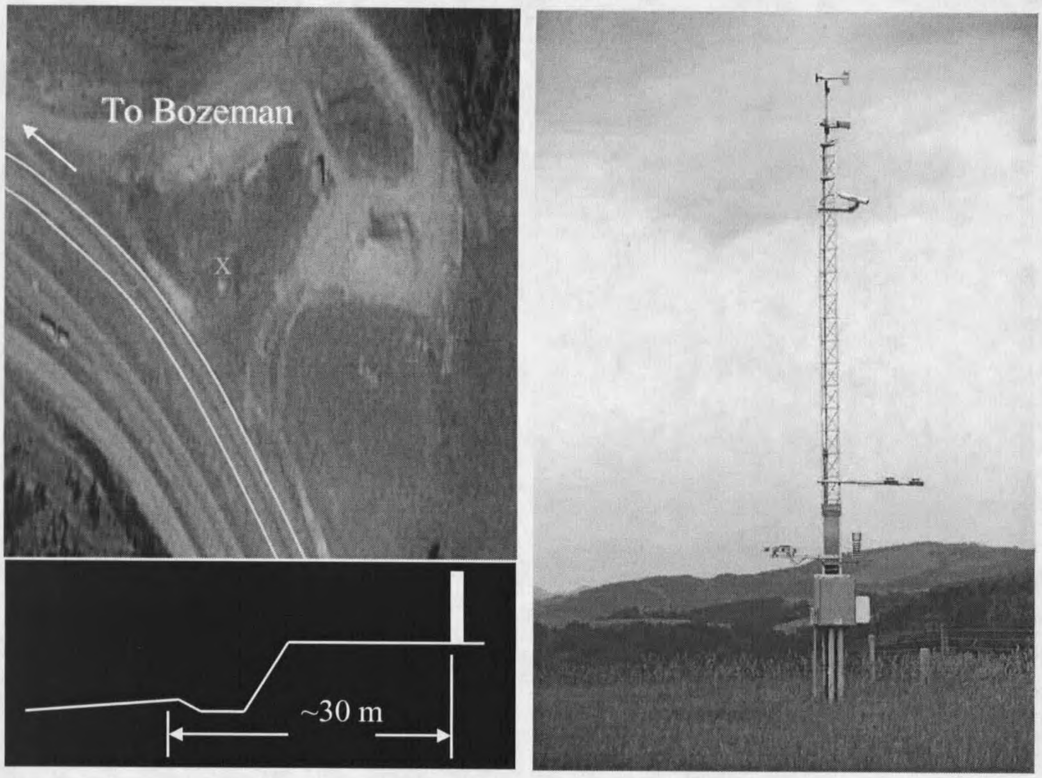

Figure 7. RWIS at BZH

Meteorological data collected by the RWIS was air temperature (C), relative humidity (RH), wind direction (°), wind speed (m/s), precipitation type, precipitation rate (cm/h), surface temperature (C), sub-surface temperature (C), incoming shortwave and longwave radiation (W/m^2) and reflected shortwave radiation (W/m^2) over the road. Instrumentation used in the RWIS is in Table 13.

Table 13. Instruments on the RWIS used for this study.

RWIS Tower					
Institution	Instrument	Model	Measures		Sensitivity
MDT	Weather Identifier	SSI #WIVIS	Precipitation 0.02 to 200 in/hr	0.4 to 4 in/hr	<5% error
				0.1 to 20 in/hr	<10% error
			Precipitation Identification		<1% error
MDT	Humidity Sensor	SSI P/N 726575501	Relative humidity 10 to 100%		+/- 5%
MDT	Anemometer	SSI #05103	Wind speed	Propeller	0.4 m/s
			Wind direction	Vane	0.8 m/s
MDT	Sub-Surface Temperature	SSI #S16UG-D	Sub-surface temperature -22° F to 176° F		± 0.36° F over range
MDT	Pavement Sensor	SSI #FP 2000	Pavement surface temperature -22° F to 176° F		± 0.36° F over range
			Surface condition	Dry Wet	-5 to 32° F 0 to 100% up to 0.50 inches
				Chem Wet	
				Snow/Ice Warning	
				Snow/Ice Watch	
WTI	Pyranometer	PSP Eppley	Incoming shortwave radiation		9 $\mu V/Wm^{-2}$
WTI	Pyradiometer	PIR Eppley	Incoming longwave radiation		4 $\mu V/Wm^{-2}$

Additional measurements and observations used in conjunction with RWIS data to classify snow conditions and albedo on road are as follows:

1.) Digital images were captured on 15-minute intervals via the Bozeman Hill internet site, it may be accessed through the MDT homepage [www.mdt.state.mt.us]. Images were used for visual confirmation of the snowcover across the road. One Surface Systems Inc. SSI color video camera was used and attached to a separate pole closer to the road. Camera output provided JPEG images.

2.) A UNICORN+ vehicle traffic classifier from DIAMOND traffic products was used to record vehicle volumes and speeds of motor traffic passing the investigation site. Vehicles counts were grouped by axle into two categories (1) "private" car, truck and trailer traffic for three or less axles and (2) "commercial" truck and bus traffic for axles > 3. Counts were summed per lane every 15 minutes. In addition to category, daily totals, average period traffic APT (15-minute period) and percentages along with average daily traffic ADT were calculated.

3.) The physical properties of snow, ice and water cover on the road was measured and observed on 15-minute intervals. Snow properties were sampled randomly to provide an unbiased representation for the road surface. The road was divided into a numbered grid. Points on the grid were selected randomly for each measurement. The properties measured included depth on road, snow grain size and classification of snow according to Maeno et al. [1988]. Location on the road was grouped into 3 divisions (1) on road in wheel tracks R1, (2) on road outside wheel tracks R2 and (3) on shoulder of road R3 (Table 14). Passing (inside) and slow (outside) lanes were marked as L1 and L2, respectively.

Table 14. Three divisions noted on road.

No. Representation	Symbol	Descriptions
1	R1	Wheel tracks on road
2	R2	On road but not in wheel tracks
3	R3	Shoulder

Efforts were made to measure snow densities that resulted in unreasonable results because of extremely small samples and time constraints from passing vehicles. This was later dropped in favor of using median densities calculated from the snow classification of Maeno et al. [1988] (Table 15).

Table 15. Snow Classification and median densities.

No. Repres.	Mean Density (g/cm^3)	Symbol	Descriptions
0	0	none	Dummy
1	0	DRY	Dry road
2	1	DAMP	Thin or spotty film of moisture
3	1	WET	Continuous film of moisture
4	0.1	NSd	New Snow Dry
5	0.15	NSw	New snow wet
6	0.3	PS	Powder Snow
7	0.375	DCSS	Dry compacted snow soft
8	0.625	DCSH	Dry compacted snow hard
9	0.6	WCS	Wet compacted snow
10	0.9	SLUSH	Liquid water and ice mixture
11	0.375	GSD	Grain snow dry
12	0.55	GSW	Grain snow wet
13	0.75	I CD	Ice crust dry
14	0.75	I CW	Ice crust wet
15	0.8	I FD	Ice film dry
16	0.8	I FW	Ice film wet

A single snow sample was collected every 15 minutes when snow was present on the road. The samples were used to determine impurity weight fraction in the snowcover. Each sample's dry and wet weight was measured to determine the mass fraction of contaminates in the snowcover. The impurity mass fraction was taken as the dry impurity weight divided by the total weight of snow and impurity. Carbon testing was performed on the dry contaminate to determine the concentration of carbon.

Albedo on the road was measured every 15 minutes using a Li-Cor LI-200SA pyranometer sensor mounted on a rod (Figure 8). This was intended as a secondary measurement of albedo. The rod allowed the extension of the sensor over the road away from the person performing the measurements as to minimize shadowing effects. Incident and reflected solar radiation was measured by rotating the rod 180°.

Figure 8. Hand held instrument and Li-Cor pyranometer sensor.

The data lacked enough samples to obtain a statistically significant representation of the snow properties on the road. Safety concerns and time constraints only allowed one sample of each of the physical snow properties to be taken each 15-minutes. Also, sample intervals vary slightly, depending on measurement opportunities between passing vehicles.

Radiation Instrumentation

The radiation instruments were supplied by the WTI. MDT and Surface Systems Inc. (SSI) field technician provided assistance in installation of sensors.

Pyranometers. Two Epply Precision Spectral Pyranometers (PSP) were installed to measure incident and reflected solar radiation. The up-faceing pyranometer was installed on the RWIS tower and was not shaded from direct solar radiation (Figure 7).

The down-facing pyranometer was mounted along the road. A tower and boom extended the sensor over the shoulder about 19ft above the road (Figure 9). A shading wall was constructed and installed to restrict the majority of the view of the sensor to the road surface since the pyranometer could not be located at a lower height over the center of the road, the optimal location. This compromise in location was restricted by traffic and safety requirements along the highway.

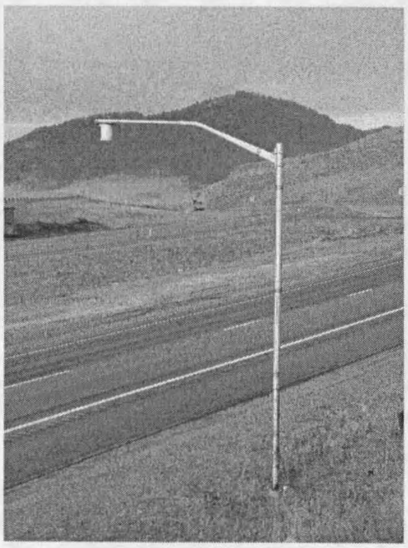

Figure 9. Down facing pyranometer over I-90

Due to instrumental troubles with the pyranometer and the RWIS remote processing unit (RPU) and difficulties coordinating with installation personal these data were not available for the measurement periods. The main problem was due to the vendor not providing sufficient support and not allowing access to the proprietary software. As result, the handheld instrument fixed with a Li-Cor pyranometer obtained albedo measurements used in this thesis. Incoming shortwave radiation was measured by the up-facing pyranometer which had been installed earlier.

The Li-Cor LI-200SA pyranometer intentionally intended to be used as back up to the defaulted PSP is not ideal for measuring albedo. The sensor is suitable for measuring global sky radiation but is not recommended by the manufacturer for measuring reflected radiation from a surface because of the non-ideal (an ideal response is a uniform spectral response from 0.28 to 2.8 um) spectral response (Figure 10) of the silicon photodiode. However, the error is small for a dry asphalt surface.

The relative response of the silicon photodiode does not extend uniformly over the solar spectrum. It is weakly sensitive near 0.4 um increasing nearly linear to a peak near 9.5 um and decreasing nearly linearly to a cutoff near 1.2 um [Li-Cor Instruction Manual]. Dry asphalt (bitumen) spectral solar reflectivity is nearly constant at 0.05% (Figure 11) and thus the spectral distribution of reflected solar flux of the asphalt is nearly unchanged from the incident flux. As a result, there should be only a small error incurred in albedo when both spectral distributions are weighted according to the relative response curve of the photodiode.

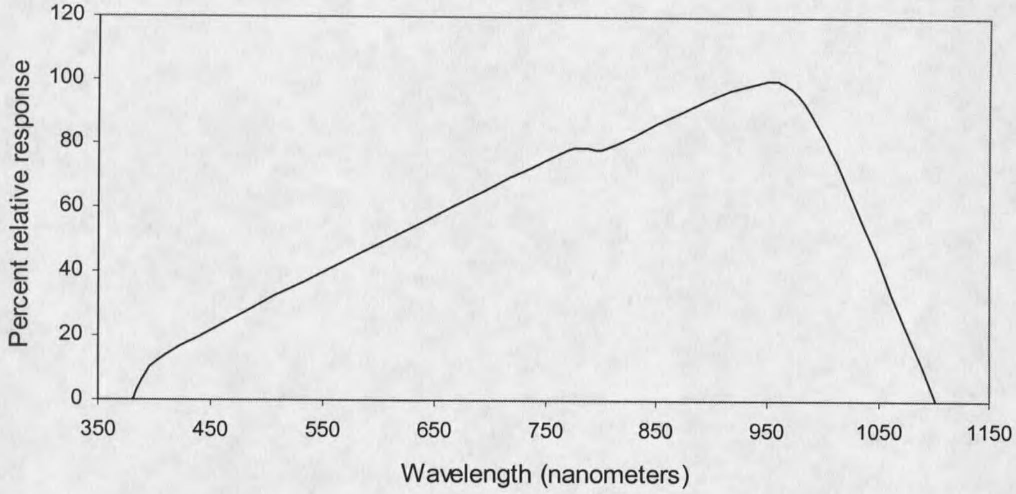

Figure 10. LI-200SA spectra response curve. Reproduced from LI-COR radiation sensors instruction manual [1986].

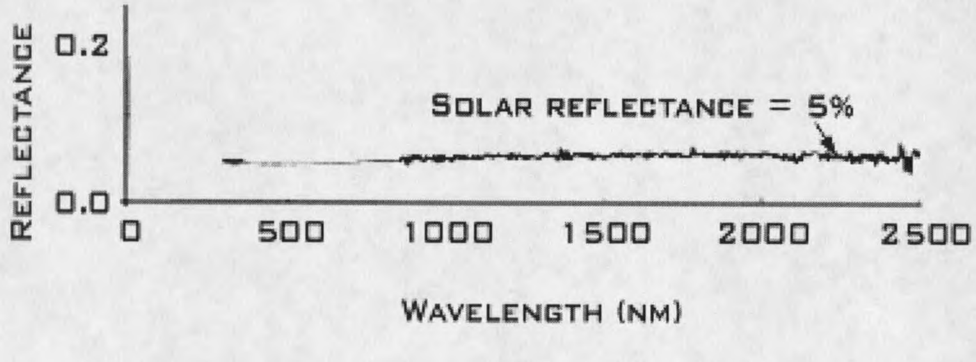

Figure 11. Spectral reflectivity of asphalt (bitumen) pavement. Partially duplicated from the Heat Island Group, http://EETD.LBL.gov/HeatIsland.

However, snow reflectance might induce a greater error because the spectral reflectance of snow is not constant over the solar region (Figure 5). Semi-infinite "pure " snow is highly reflective in the VIS and an effective absorber in the NIR. When weighted according to the relative response of the photodiode the high reflectance of a snow surface near 0.4 um might not register as strong as a weak reflectance near 0.9 um. As a result, it suggests that the albedo of snow would be slightly suppressed when measured by the Li-Cor because of bias of the sensor response toward longer VIS wavelengths. On the other hand, there might not be much error in albedo measurements for highly dirty snow because VIS light absorbing contaminates suppress the spectral reflectivity in the VIS region causing the variation in VIS spectral reflectivity to be lower. The result is a more uniform spectral reflectance that does not change the spectral distribution of the radiation as greatly.

Pyradiometer. One Eppley Precision Infrared Radiometer (PIR) was permanently installed on the RWIS tower and used to measure incoming longwave radiation (Figure 7). No shading disk was used.

Accuracy of the sensor was suspect, despite continual communication with the acting MDT field technician and SSI to confirm calibration and system protocol. Measured longwave radiation was unrealistic during the observation periods. As a result longwave radiation was approximated based on air temperature, vapor pressure and cloud cover fraction (see Chapter 3, Validation of the Test-Platform). The additional variable, cloud cover, needed to approximate incoming IR was not measured at the research site and so was estimated from ARPS forecasts.

Observations

Snow Grain Size. Grain size was measured by direct observation of the snow sample from the road surface. A 10x-magnified lens was used with a mm grid ruler to estimate the grain size range. The range of snow was distinguished by noting the largest and smallest grains. Grain size was assumed as the longest length of the crystal. The longest axial dimension was selected to classify the snow grain size because of the limited magnification and measurement precision employed in the field.

Sample observations were limited to one per snow sample. The method weighted the observed snow particle size range towards the sample distribution rather than the population, due to high anisotropy of the snow properties on roads, because only one measurement was taken to represent the snow conditions at each grid point. Also, a limited magnification and measurement scaling (mm divisions) almost certainly shifted the observed grain size towards larger grains because larger grains were more visible then small ones. Some very small grains may have been entirely overlooked if they were undistinguishable with the 10x lens. Also, the small grains (<1 mm) may have been inaccurately measured because they were estimated by using the same mm scale.

The method used in this thesis to measure snow grain size in all likelihood overestimated the actual grain size on the road because only the largest dimensions of a grain were used which tends to shift the mean to a larger grain size. As result the effective grain size used in the model was overestimated when based on the measurements methods used in this thesis. Future work would alter the protocol. In addition, the actual optically effective size in the snow cover will differ from the effective optical size [WWI, WWII]. Nakamura et al. [2001] supports this, indicating that the actual size distribution may shift to smaller grains if the smaller bonds betweens snow grains are not included in the size distribution. Furthermore, actions by vehicles to mechanically break snow grains also could decrease mean particle size.

Snow Depth. The depth of snowcover was measured with a mm division ruler at the point the sample was obtained and assumed as the mean depth for the adjacent area. Again, because there was one measurement of depth for each point no distribution was obtained. High undulation of snowcover on the road increases variability of the measurement.

When only water was present at the sample point the depth of the water as assumed to lie between a wet and dry surface according to an arbitrary visual classification of the condition (Table 16). The median depth was linearly interpolated between the high (wet surface) and the low (dry surface).

Table 16. Estimating median depth of water on road.

Classification	Approximate Depth (mm)
Dry	0
Dry \ Damp	0.25
Damp	0.5
Damp \ Wet	0.75
Wet	1

Snow-on-Slab Albedo Model

The snow-on-slab albedo model (SOSA) can be viewed as being composed of two major components, a computational albedo routine and a pavement snow conditions routine. The computational albedo routine (CAR) was adapted from the parameterized allwave snow albedo model (SNOALB) of Marshall [1989]. CAR calculates the allwave albedo on the road given 7 realistic physical input parameters. The pavement snow conditions routine (SCR) models snow conditions on the road. It is a preliminary effort to model grain growth, snow accumulation and erosion, impurity content, and snow type exposed to vehicle and winter maintenance influences.

The SOSA model is written in C language as a subroutine package to WinThermRT. All communication between WinThermRT and SOSA will be accomplished through call statements. Extrapolation of albedo over the terrain grid is accomplished in WinThermRT.

The model assumes the snowcover has homogeneous properties, such as grain size, depth, density, impurity concentration, temperature and ablation. The thermal characteristics are assumed to be that of a very thin layer which is at the temperature of the pavement surface. As a result, actual temperature gradients and heat conduction through the snowcover is neglected at this time. Radiation heat fluxes are assumed to absorb uniformly in the bulk snowcover at the pavement surface. All melt takes place at the interface between the snow and pavement. Observed snow conditions are assumed to represent an average for the snow-pavement surface. The assumption is valid for

WinThermRT's surface element model in which the albedo of the grid point is the surface average for the 30 m square elemental plate.

Computational Albedo Routine.

The albedo routine was directly adapted from the parameterization of albedo by Marshall [1989]. The parameterized albedo routine of Marshall [1989] was converted to C language [by Dr. R. L. Brown, Montana State University]. For details on the mathematical formulation of the albedo routine see Chapter 2, Parameterization of Albedo, the section on parameters summarizes Marshall's [1989] model.

Adoptions were made to SNOALB to account for differences in snow properties encountered over pavements exposed to passing traffic and winter maintenance operations. This required a major portion of this thesis to be concerned with the validation of SNOALB for snowcover on roads. Validation focused on the properties of snow on roads that influences albedo but differ from seasonal snowcovers. The treatment of the spectral and angular distribution of solar radiation in SNOALB is not changed in the model. Atmospheric transmittance and diffuse fraction do not differ between seasonal snocovers and snow on roads because they are properties of the solar downflux and not the snow. Therefore, they were not a focus for adoption of SNOALB to snowcover on roads. As a result, validation focused on effective grain size, optical mass cross-section and VIS light absorbing impurities effective mass fraction. SNOALB was also updated to account for conditions of wet and dry pavements and to return the appropriate albedo.

CARs inputs directly adapted from SNOALB are snow grain radius (μm), contaminate concentration (mass fraction), mass cross-section (g/cm^2), zenith cosine, atmospheric pressure (mmbar), underlying surface albedo, diffuse fraction for VIS and NIR, surface downflux for VIS and NIR and atmospheric transmittance for VIS and NIR. On output CAR gives the spectrally integrated VIS and NIR region and solar albedos.

The albedo routine was run over a range of arbitrary data to provide a view of CARs sensitivity to model inputs. As discussed earlier Warren [1982] classified grain size, impurity mass fraction, snow depth and zenith cosine as the primary factors affecting snow albedo. The sensitivity of CAR to these four factors is demonstrated below. The effect of grain size and impurity concentration can be clearly seen in Figure 12

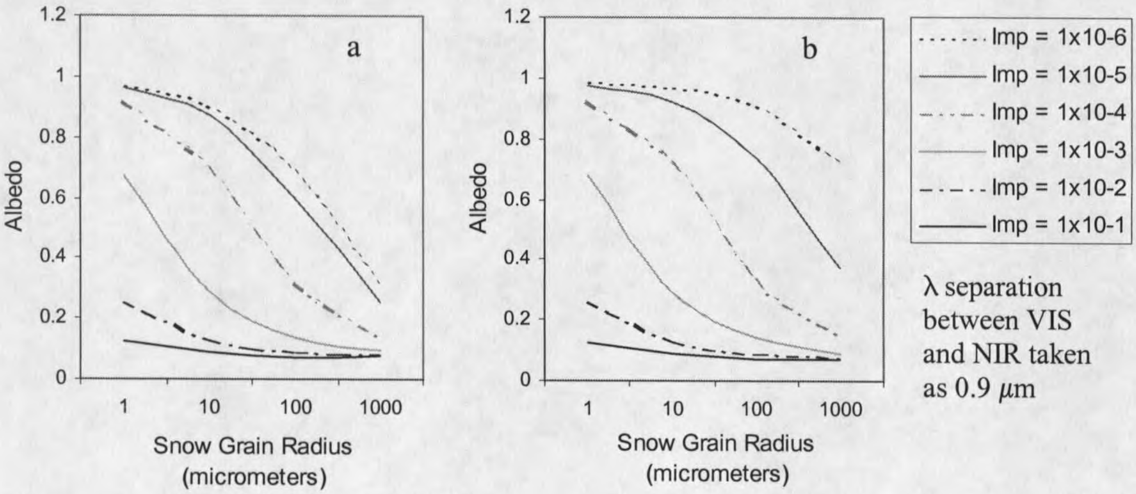

Figure 12. The influence of snow grain size on albedo (a) for a $m_{xs} = 5$ kg/m^2 and (b) for a $m_{xs} = 50$ kg/m^2. Other data is $d_f = 0.5$, $p_{atm} = 750$ millibar, $\mu_o = 0.65$, $\alpha_g = 0.12$.

Grain size is varied from 1 to 1000 μm and the concentration of impurities is varied from 1 to 100,000 ppm in Figure 12. Grain size and impurity content have a strong influence on albedo in the model. The influence of impurities increases with concentration and increasing grain size. Albedo is more sensitive to increases in grain size for thin snow than for deep snow. This is demonstrated in Figure 12, (a) the effect of the underlying surface albedo is shown to be greater as grain size increases than in (b) which represents snow of equal density but 10 times deeper.

The influence of different underlying surface albedos is shown in Figure 13. It is clearly seen that as the grain size increases the pavement albedo has a stronger influence on the snow albedo. This is explained as follows, as grain size increases incident light rays on the surface of the snowpack have an increased chance of penetrating deeper into the snowcover, which raises their probability of being absorbed at the bottom surface.

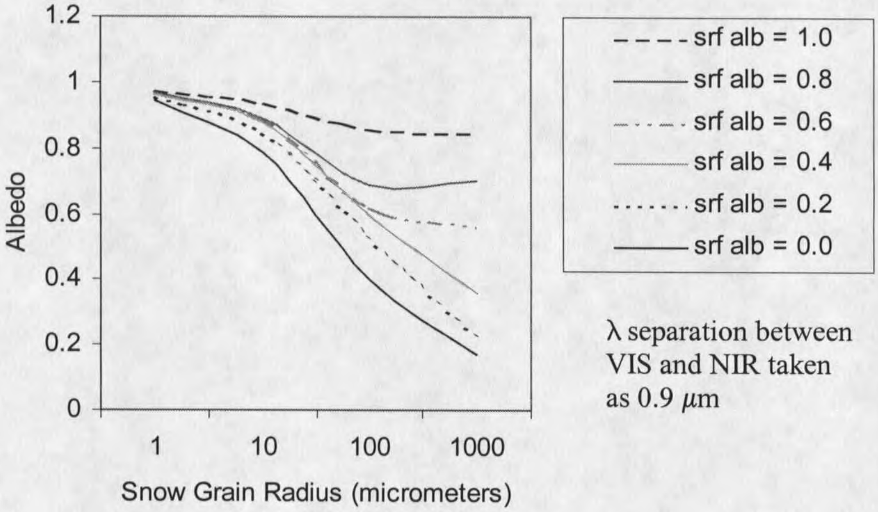

Figure 13. Influence of the underlying surface on the albedo of thin snow over a range of grain sizes. Results for $m_{xs} = 0.5$ kg/m^2, $d_f = 0.5$, $p_{atm} = 750$ millibar, impurity concentration of 10 ppm and $\mu_o = 0.65$. Pavement albedo varied from 1 to 0.

The influence of zenith cosine and diffuse fraction (d_f was considered because it affects albedo by altering the effective zenith angle) on snow albedo is demonstrated in Figure 14 and Figure 15. It can be clearly seen that the affect of zenith angle and diffuse radiation on snow albedo is minimal compared to the affect of impurity concentration and grain size. As a result, the impurity mass fraction and grain size are the strongest factors affecting the accuracy of the albedo routine. Consequently, uncertainties in μ_o and d_f have less weight than uncertainties in impurity concentration and grain size to error in the model.

The optical mass cross-section simply determines the degree of influence of the underlying surface albedo. Snow thickness on roads is in general optically thin. Thus, the mass cross-section is an important factor in CAR because of the low albedo of pavement (e.g. $\alpha_g = 0.12$) in comparison to snow albedo (e.g. clean snow $\alpha = 0.7$ to 0.8).

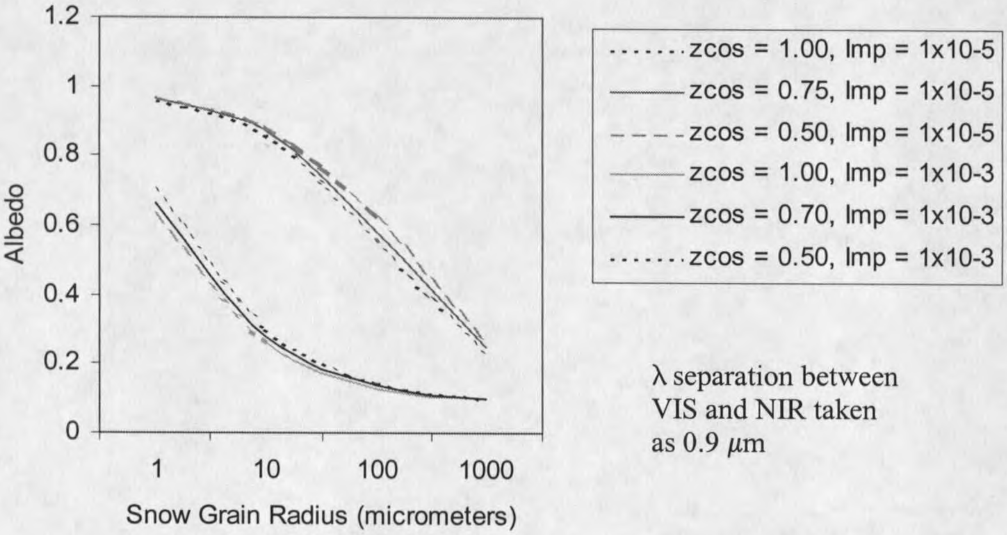

Figure 14. Influence of zenith cosine on snow albedo over a range of grain sizes. Results for $m_{xs} = 0.1$ kg/m^2, $d_f = 0.5$, $p_{atm} = 750$ millibar impurity concentration of 10 ppm and 1000 ppm, $\alpha_g = 0.12$ and $\mu_o = 0.65$.

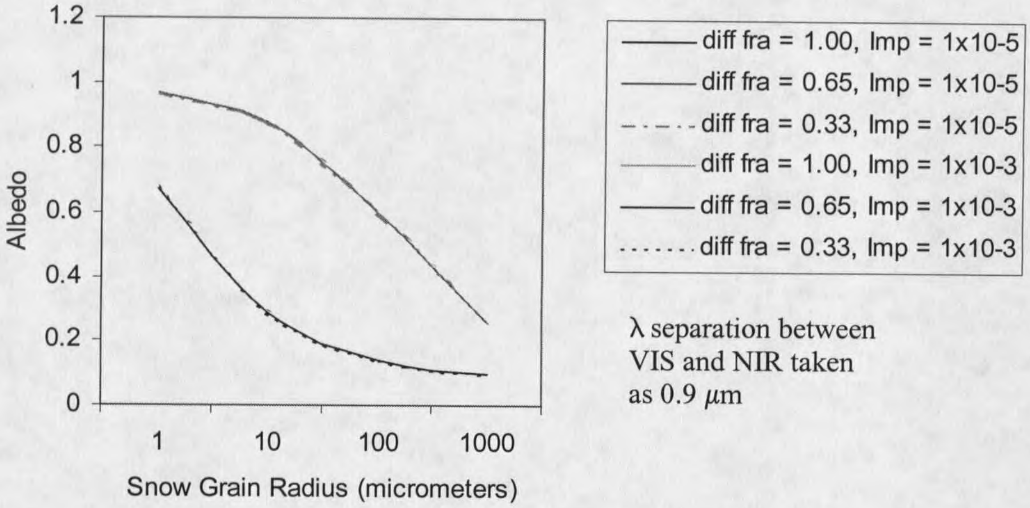

Figure 15. Influence of diffuse fraction on snow albedo over a range of grain sizes. Results for $m_{xs} = 0.1$ kg/m^2, $d_f = 0.5$, $p_{atm} = 750$ millibar impurity concentration of 10 ppm and 1000 ppm, $\alpha_g = 0.12$ and $\mu_o = 0.65$.

Data for atmospheric transmittance, surface downflux and diffuse fraction were not available at the research site. As a result, atmospheric transmittance was assumed to be the global average of 0.55, a reasonable assumption [Marshall 1989, Wallace and Hobbs 1971, Fig. 7.1]. Diffuse fraction was assumed to be 0.5 to represent 50% diffuse surface downflux. The surface downflux was estimated in the albedo model by matrix fluxes developed by Marshall [1989]. The division between VIS and NIR regions is taken as 0.7 μm. The cosine of the zenith angle μ_o is set to 0.65 in CAR to represent isotropic diffuse conditions [Marshall 1989].

Atmospheric pressure data was not available from Bozeman Hill RWIS. Pressure data comes from Bozeman Farm, [provided by Dr. S. Custer, Department of Earth Sciences, MSU] and is extrapolated to Bozeman Hill [Liaw 1973].

The density of the atmospheric air should normally decrease with increasing altitude [Liaw 1973]. Assuming that a column of gas extending vertically into the atmosphere is at constant temperature, the atmospheric surface pressure p may be calculated from the following relationship [Liaw 1973, Jones and Dugan 1996],

$$p = p_o \cdot e^{-\left(\frac{m_{mol} \cdot g \cdot z}{k \cdot T \cdot Na}\right)} \tag{42}$$

where p_o = reference surface pressure (kPa or mmbar)

T = atmospheric air temperature

m_{mol} = molar mass of air (28.97 kg/kmol)

k = Boltzman molecular gas constant (1.38×10^{-23} J/molecule-K)

g = gravitational acceleration (9.81 m/s^2)

N_a = Avagodro's number (6.022×10^{26} molecules/kmol)

z = elevation difference between reference and desired surface (m)

Equation (42) is more accurate for small differences in elevation or altitude between the reference and surface in question because variation in atmospheric temperature can be minimized. The elevation of Bozeman farm is 1455.42 m and the elevation of Bozeman Hill is approximately 1524 m, so $z \sim 70$ m. The air temperature measured by the RWIS is substituted as the atmospheric air temperature in equation (42).

Pavement Snow Conditions Routine.

The pavement snow conditions routine (SCR) models the temporal physical conditions of the snowcover on the roads. The physical conditions modeled and needed as inputs into SOSA are snow grain radius (μm), contaminate concentration and the optical mass cross-section (g / cm^2). Heat fluxes are calculated in the test-platform (see CHAPTER 3, Test-Platform) and are used in conjunction with MET data from RWIS to model snow conditions.

The routine is composed of three parts, (1) a routine to approximate the effective grain size, (2) a routine to estimate mass fraction of impurities and (3) a routine to keep track of the mass cross-section of snow, ice, sand and water on the pavement.

Effective Grain Size. An increase in the FWC of snow effectively increases the optical grain size. Thus to generalize, the effective snow grain radius is classified according to the FWC of the snow on the road (Table 17)

Table 17. Effective snow grain radius with respect to FWC. The effective radius is adopted from radii used by WWI and WWII to represent new, aged and melting snow.

FWC	Effective radius r_{eff} (μm)
Less than 15%	50
Greater than or equal to 15% and less than 30%	100
Greater than or equal to 30%	1000

The effective grains size in SCR increases as the FWC of the snow increases. If refreezing occurs the snow grain size is held at its previous value. This approximates the negligible decrease in the effective radii when refreeze occurs. However, if new snow begins to accumulate the grains size is allowed to decrease through adjustment to the FWC. The grain size is set to zero when the snow and ice completely ablates from the road.

Pure ice on the surface may contain fractures and air bubbles that can raise the reflectance and hence the effective grain size. However, ice is still readily transparent for thin depths. To simulate semi-transparent behavior, an effective radius of $r_{eff} = 500{,}000$ μm is assumed for ice with a mass cross-section greater than 1 kg/m^2. Other effective grain sizes were experimented with but gave less desirable results. "Black ice" is taken as a skiff of ice with a mass cross-section of ≤ 1 kg/m^2 (a maximum geometrical depth of ~ 1 mm) and is assumed optically transparent. Hence, the effective radius of black ice is taken to be zero. If water is only present an effective depth of zero is also used.

The Optical Mass Cross-Section. The routine uses a series of control statements in succession with physical principles to monitor the mass cross-section of water, snow, ice and sand on the highway. Water accumulates from rain precipitation or snow/ice melt. Snow deposition is only from precipitation. The mass cross-section of ice represents refreeze of liquid water. The sum of water, snow and ice mass cross-sections is the total optical mass cross-section input into CAR.

The mass cross-section routine accounts for the ablation and deposition of ice, snow and water by applying the following assumptions: *melting* of snow and ice occurs when the surface temperature is at or above the equilibrium temperature, $Q_m > 0$ and snow or ice is present; *freezing* occurs when the surface temperature is at or below the equilibrium temperature, $Q_m < 0$ and liquid water is present; *evaporation* occurs in the model when the surface temperature is greater than the equilibrium temperature, $Q_e < 0$ and liquid water is present. Condensation was not considered.

As stated above, the mass cross-section is taken as the optical mass of the medium over a unit area on the surface. The medium is water and is normalized to bubble free ice within CAR, which gives an effective optical path length. The governing differential equation DE used to equate the mass cross-section is developed from the law of conservation of mass [referenced from Chandrasekharaiah and Debnath 1994]. Consider a fixed control area A with depth d_s, which represents a volume V that changes with d_s. Mass m within V at time t may be expressed as

$$m = A \cdot \int_0^{d_s} \rho \cdot dz \tag{43}$$

where ρ is the bulk density of the medium. The law of conservation of mass (in material form) states mass must be conserved during motion [Chandrasekharaiah and Debnath 1994],

$$\frac{D(m)}{Dt} = 0 \tag{44}$$

In spatial form,

$$\frac{\partial(m)}{\partial t} + \mathbf{v} \circ \nabla(m) = 0 \tag{45}$$

Then evaluation of equation (43) and substitution into equation (45) gives,

$$A \cdot \left[\frac{\partial(\rho \cdot d_s)}{\partial t} + \mathbf{v} \circ \nabla(\rho \cdot d_s) \right] = 0 \tag{46}$$

where $\frac{\partial(\rho \cdot d_s)}{\partial t}$ represents the local change of mass in the volume

$\mathbf{v} \circ \nabla(\rho \cdot d_s)$ represents mass entering and leaving the volume

Equating the mass fluxes to melt, precipitation and vehicle erosion and dividing through by A, the mass balance per unit area on the highway, which represents the mass cross-section of the medium, [similar to the DE used by Naruse et al. 1988] may then be stated as,

$$\frac{\partial(\rho \cdot d_s)}{\partial t} + \dot{M} + \dot{E}_v + \dot{E}_m = \dot{P} \qquad (47)$$

where d_s = snow thickness (m)

ρ = mean snow density (kg/m^3)

M = amount of melting in the snow layer (kg/m^2)

E_v = amount of erosion by vehicles (kg/m^2)

E_m = amount of erosion by winter maintenance (plowing) (kg/m^2)

P = amount of precipitation (kg/m^2)

The partial differential equation (47) considers a unit area with thickness h from the pavement surface to the top of the snowcover to represent the mass cross-section, so dimensions of each term are mass per unit area (kg/m^2). A positive sign indicates mass deposition for P and a negative sign indicates mass ablation for M, E_v and E_m. The relation does not account for negligible amounts of evaporation and sublimation from the surface.

Accumulation and ablation of snow (water, ice and sand are analogous) on the road may then be modeled using a forward differencing scheme,

$$\frac{\partial m_{xs}}{\partial t} = \frac{m_{xs}{}^{j+1} - m_{xs}{}^{j}}{\Delta t} \tag{48}$$

Substitution into equation (47) and rewriting yields,

$$m_{xs}{}^{j+1} = m_{xs}{}^{j} + \Delta t \cdot \left(\dot{P} - \dot{M} - \dot{E}_v - \dot{E}_m\right) \tag{49}$$

The snowmelt rate $\dot{M}$ (kg/m^2-s) is given by [Gray and Male 1981],

$$\dot{M} = \frac{Q_m}{L_f \cdot B} \tag{50}$$

where L_f = latent heat of fusion (333.5 kJ/kg)

B = thermal quality or fraction of ice in a unit mass of wet snow

Q_m = energy flux available for change of phase (kJ/m^2-s)

Direct precipitation rates from the RWIS that could have been used to determine P turned out to not be reliable, in fact, mostly none existent. However, the RWIS did provide a general intensity classification, e.g., light, moderate and heavy. The classification is adopted from the NWS. This allowed intensity rates to be estimated as a single value in Table 18.

Table 18. General classification of precipitation rates based on intensity classifications by the NWS.

Intensity classification	Rate range (cm/hr)	Rate used (cm/hr)
Light	0.0 – 0.25	0.2
Moderate	0.26 – 0.76	0.5
Heavy	> 0.76	1.0

Vehicles erode and compact snow as discussed previously. The amount of erosion per vehicle (kg/m^2-veh) is estimated from Fig. 1, Schaerer [1970]. The vehicle erosion flux (kg/m^2-s) per lane is then taken as,

$$\dot{E}_v = \left(\frac{\rho \cdot d_s}{\Delta t \cdot AHT} \right) \cdot \frac{APT}{60} \tag{51}$$

where ρ_s is the snow density, d_s is the snow depth, Δt the assumed time period and AHT is the average hourly traffic (see Table 19). The 1/60 is used to convert $\dot{E}_v$ from amount per 15 minutes to per 1 second. The erosion amount per vehicle, represented by the term in parenthesizes in equation (51), are given in Table 19 for a range of FWCs.

Table 19. Traffic erosion rates verses FWC of snow. The ρ_s was taken near that of slush (900 kg/m^3) and AHT was taken as 50 veh/hr for m_{xs} > 4.5 kg/m^2 and 100 veh/hr for m_{xs} < 4.5 kg/m^2, where $m_{xs} = \rho_s \cdot d_s$. Δt was estimated from Figure 1, Schaerer [1970]. With m_{xs} = 4.5 and ρ_s = 900 kg/m^3, d_s is ~ 5 mm.

Mass cross-section (kg/m^2)	FWC $\geq$ 30%	30% > FWC $\geq$ 15%	FWC < 15%
$m_{xs} \geq 4.5$	0.18 kg/m^2-veh	0.036 kg/m^2-veh	0.0 kg/m^2-veh
$m_{xs} < 4.5$	0.018 kg/m^2-veh	0.0036 kg/m^2-veh	0.0 kg/m^2-veh

The FWC controls the erosion, compaction and effective grain size in the model. The FWC is defined as,

$$FWC = \frac{m_{xsWATER}}{m_{xsWATER} + m_{xsICE} + m_{xsSNOW}} \tag{52}$$

The max liquid water holding capacity of the snow is taken as 30% [Schearer 1970]. The effective saturation depth of water on the pavement surface is taken as 1 kg/m^2 (~ 1 mm of water). Liquid water beyond 1 mm is assumed to drain completely from the surface.

The SCR employs a simple approach to estimate the mass cross-section of sand on the road since little work has been done to understand and model sand distribution over roads due to sanding operations. The sand mass cross-section is approximated by an average lane hourly pass rate AHP based on the observations of winter maintenance vehicles passing the research site. Approximately 1 cubic yard of sand per lane mile is deposited on the pavement during general sanding procedures. The bulk mass of sand per cubic yard is 1668.39 kg. Thus, for 12ft lanes the sand distribution over a mile is taken as ~0.2834 kg/m^2 per pass of the plow. SCR only allows sand to be deposited when snow or ice is present. Since vehicles readily remove snow with a FWC $\geq$ 30%, sand is only applied in the model while the FWC < 30%. The sand mass fraction is calculated by taking the sand mass cross-section divided by the sum of the mass cross-sections of sand, water, ice, and snow.

Test-Platform

To assist in development of SOSA, a test-platform was created to provide an experimental foundation to which SOSA could be compared. The test platform is intended to use the same meteorological inputs as WinThermRT but which is spatially restricted to a single node. Development focused on the temporal dependence of albedo at the single grid point. Extrapolation of albedo to the topographical grid is accomplished internal to WinThermRT.

The test-platform developed consists of a computational routine (energy routine) used to compute heat fluxes at the surface of the road. The energy routine calculates the net radiation (short and longwave), sensible, latent, ground, precipitation and vehicle heat fluxes at the road surface and returns the total flux Q_m at the surface available to change temperature or phase. Equation (53) gives the general energy balance used in the routine [Price et al. 1976, Ishikawa et al. 1999],

$$Q_m = Q_{lw} + Q_{sw} + Q_h + Q_e + Q_g + Q_p + Q_a \tag{53}$$

where Q_m = total energy flux (W/m^2)

Q_{lw} = net longwave radiation flux (W/m^2)

Q_{sw} = net shortwave radiation flux (W/m^2)

Q_h = sensible or convective heat flux (W/m^2)

Q_e = latent heat flux (W/m^2)

Q_g = ground heat flux (W/m^2)

Q_p = precipitation heat flux (W/m^2)

Q_a = heat flux from vehicles (W/m^2)

A negative (-) sign indicates heat flux directed away from the surface and a positive (+) sign indicates heat flux towards the surface. Q_p is zero with no precipitation. Q_a is negligible because of minimal shading time from each vehicle [Ishikawa et al, 1999]. Q_e is zero for dry roads.

Air temperature, relative humidity, wind direction, wind speed, precipitation type, precipitation rate, surface temperature, subsurface temperature, incident solar irradiance, incident longwave radiation and atmospheric pressure are the meteorological inputs into the test-platform. All MET data except atmospheric pressure is obtained from the MDT RWIS unit at Bozeman Hill. Pressure comes from Bozeman Farm, (operated by Department of Earth Sciences, MSU) and is extrapolated to Bozeman Hill. Data was isolated into 24 hr periods for running through the model.

<u>Longwave Radiaiton Flux</u>. Net longwave radiation flux Q_{lw} (W/m^2) is obtained from the difference between incoming L_i and emitted L_o longwave flux,

$$Q_{lw} = L_i - L_o \tag{54}$$

L_i was intended to be obtained by direct measurement from an Eppley PIR mounted on the RWIS Tower. However, data coming from the PIR was suspect, so incoming IR was estimated from air temperature, water vapor pressure and cloud cover fraction (see CHAPTER 4, Validation of the Test-Platform).

Emmission of longwave radiation may be obtained using Planck's relation [White 1991] given by

$$L_o = \varepsilon \cdot \sigma \cdot T_s^4 \tag{55}$$

where ϵ is the surface emisivity [assumed ~ 1 for snow and asphalt, Adams 1991, Snyder et al. 1997, Sobrino and Cuenca 1999 and Ishikawa 1999], $\sigma = 5.67 \times 10^{-8}$ (W/m^2-K^4) is the Stefen-Boltzmann constant and T_s is the effective surface temperature. The model assumes that T_s represents the temperature of the thin snowcover and the pavement surface as a bulk medium.

Shortwave Radiation Flux. The net surface flux from solar radiation Q_{sw} (W/m^2) is dependent upon the amount of global radiation G absorbed at the surface,

$$Q_{sw} = G \cdot (1 - \alpha) \tag{56}$$

where the amount of radiation absorbed at the surface is known from the albedo α. G is the sum of diffuse radiation I_{dif} and direct beam radiation I_{dir}; $G = I_{dir} + I_{dif}$. Total shortwave downflux (global radiation G) is measured at the RWIS by an Eppley PSP.

Turbulent Fluxes. The sensible (convective) heat flux takes into account heat transfer between air and the surface without phase change. Sensible flux Q_h is driven by the temperature gradient between the air and the surface as follows [Ishikawa et al. 1999],

$$Q_h = \rho_a \cdot C_p \cdot K_h \cdot U \cdot (T_a - T_s) \tag{57}$$

where C_p is the specific heat capacity of air (J/kg-K), U is the wind speed (m/s), T_a and T_s are the air and surface temperature (K), respectively, K_h is a dimensionless turbulent transfer coefficient for heat and ρ_a is the air density (kg/m^3), which is obtained from the ideal gas law as

$$\rho_a = \frac{p_{atm}}{R \cdot T_a} \tag{58}$$

where R is the gas constant for air (0.287 kJ/ kg-K) and p_{atm} is the atmospheric pressure (kPa).

The latent heat flux Q_e (W/m^2) is due to phase change and is driven by the vapor pressure gradient between air and surface. The latent flux is only included in the energy balance (53) when there is evaporation from the surface and is denoted by [Ishikawa et al. 1999],

$$Q_e = 0.622 \cdot \rho_a \cdot L_e \cdot K_e \cdot U \cdot (e_a - e_s) \cdot p_{atm}^{-1} \cdot 1000 \quad (59)$$

where L_e = latent heat of phase change (kJ/kg)

e_a, e_s = water vapor pressure of air and surface (kPa)

K_e = dimensionless turbulent transfer coefficient for water

p_{atm} = atmospheric pressure (kPa)

The unit transformation of 1000 J/kJ is used to keep latent flux in the same units as the other heat flux's in the model (W/m^2). K_h and K_e may be assumed the same, under neutral atmospheric conditions [Price et al. 1976, Ishikawa et al. 1999]. Ishikawa [1999] reported the value for K_h (2.3 x 10^{-3}) for a melting snow surface.

Neutral atmospheric conditions describes the state of stability of the atmosphere. Also known as neutral stability or hydrostatic equilibrium. Neutral stability refers to the state of a saturated or unsaturated parcel (differential volume) of air that when displaced vertically experiences no buoyant acceleration. In other words, a parcel of air displaced from its original position remains at the new position because of a balance between gravitational and pressure forces (e.g. the parcel of air is at the same temperature and pressure as the surrounding air). This state depends on local weather conditions, the adiabatic lapse rate (basically a vertical temperature gradient) and amount of solar heating at the surface and in the atmosphere. Large scale atmospheric motions (motion in horizontal extent >> motion in vertical extent) are basically neutrally stable [Schneider 1996]. However, small scale motions are not explicitly neutral. Local meteorological factors (such as excessive surface heating) can influence the stability directly above the surface. Nonetheless, in general, neutral stability conditions apply under a range of meteorological circumstances including very strong winds, or light wind and cloudy skies.

Vapor pressure, e_a and e_s, is calculated from the Clausius-Clapeyron equation, which provides a simple and reasonably good approximation [Liaw 1973, Jones and Dugan 1996]. The Clausius-Clapeyron equation can be derived from the Gibbs function, a relation that describes complete equilibrium. It relates the saturation pressure-temperature slope, latent heat and the change in volume for a phase transformation as follows [Jones and Dugan 1996]

$$\frac{dp}{dT} = \frac{h_{fg}}{T \cdot v_{fg}} \tag{60}$$

where $h_{fg} = h_g - h_f = L_e$ the latent heat of phase change (kJ/kg), T is the temperature (K) and $\nu_{fg} = \nu_g - \nu_f$ is the specific volume (m^3/kg). Subscript f and g refer to states of saturated liquid and saturated vapor, respectively. Water vapor may be modeled as an ideal gas using the ideal gas equation [Jones and Dugan 1996],

$$p_g \cdot v_g = R \cdot T \tag{61}$$

where p_g is saturation vapor pressure (kPa) and R is the gas constant for water (0.462 kJ/kg-K). Also, noting that for water that $\nu_g >> \nu_f$, it allows ν_f to be assumed zero with respect to ν_g. Substitution of (61) into (60) and simplifying gives,

$$\frac{dp}{dT} = \frac{L_e \cdot p_g}{R \cdot T^2} \tag{62}$$

Separation of variables and integration between limits (p, p_o) and (T, T_o) leads to,

$$\ln\left(\frac{p_g}{p_o}\right) = \frac{L_e}{R} \cdot \left(\frac{1}{T_o} - \frac{1}{T}\right) \tag{63}$$

Then rearranging terms provides the final form for the Clausius-Clapeyron equation, which is only accurate for small temperature changes where L_e may be approximated by a single value:

$$p_g = p_o \cdot e^{\left(\frac{L_e}{R} \cdot \left(\frac{1}{T_o} - \frac{1}{T}\right)\right)} \tag{64}$$

where p_o, T_o = reference saturation pressure (kPa) and temperature (K), respectively

p_g = saturation vapor pressure (kPa)

L_e = latent heat of the phase transition (kJ/kg)

R = gas constant (kJ/kg-K)

T = temperature of reaction (K)

The partial pressure of water vapor in air can be obtained from the definition of relative humidity ϕ,

$$\varphi = \frac{p_v}{p_g} \tag{65}$$

where p_v is the vapor pressure (kPa) and p_g is the saturation vapor pressure [Jones and Dugan 1996]. At the snow and water surface where ϕ was not measured, H_2O vapor pressure is assumed to be saturated [Adams 1991], i.e., $\phi = 1$. Therefore,

$$p_v = p_g \tag{66}$$

which allows vapor pressure to be obtained from the Clausius-Clapeyron equation (61). In the air, the vapor pressure is simply calculated from the relative humidity relation because ϕ is measured by the RWIS. The H_2O vapor pressure is as follows,

$$p_v = \varphi \cdot p_g \tag{67}$$

Flow over a surface is considered turbulent when the dimensionless Reynolds number Re_x is $\geq 500{,}000$. The Reynolds number is given by

$$\mathrm{Re}_x = \frac{\overline{U} \cdot x_c}{\nu} \tag{68}$$

where $\bar{U}$ is the mean wind speed (m/s), x_c is the characteristic length (m) and ν is the kinematic viscosity (m^2/s).

The characteristic length along the road depends on the direction of wind. At times the wind direction may be parallel to the road, perpendicular or lie some where between. Minimal winds speeds for turbulent conditions (neglecting surface roughness, local terrain and vehicle influences) over the road are given in Table 20.

Table 20. Minimal mean wind speeds for turbulent conditions above the road surface. Characteristic lengths are taken as 10 m (represents wind perpendicular to 2 lane highway) and 40 m (wind parallel to highway). ν is for dry air, obtained from Appendix G, White [1991]. $Re_x = 500{,}000$.

	Wind Speed U (m/s)		
	350 K	300 K	250 K
Perpendicular to road	1.00	0.79	0.57
Parallel to road	0.26	0.20	0.14

Winds commonly are parallel to the I-90 over the pass since the highway is in a east-west direction (prevailing winds are westerly) and is cut below the ridge forming a channel that increases wind velocities. On average winds speeds over days considered were $\bar{U} > 1$ (m/s). Also, there are addition reasons to support the turbulent assumption: (a) local terrain irregularities around the highway can produce eddies, (b) a continual flow of vehicles passing over the road mix air on the surface creating turbulence and (c) the road surface is not smooth when covered with snow.

Ground Heat Flux. Heat conduction is given by Fourier's Law of conduction,

$$Q = -k \cdot \frac{dT}{dz} \tag{69}$$

where coefficient k_b is the thermal conductivity (W/m-K) of the material [White 1991]. The asphalt pavement and aggregate base was originally assumed to be an isotropic medium with the thermal conductivity k_b of pure asphalt. The ground heat flux Q_g is determined as follows,

$$Q_g = k_b \cdot \frac{T_g - T_s}{z_g} \tag{70}$$

where T_s is the surface temperature (K) representing the snowcover and top layer of pavement measured by the RWIS, T_g is the ground temperature measured at a depth z_g = 43 cm below the pavement surface. This method assumed a linear temperature profile and uniform conductive properties through the pavement and base material, obviously a large simplification. Initial runs indicated that measured ground temperature data from the RWIS was unreasonable (see CHAPTER 4, Validation of Test-Platform). As a result, ground temperature was approximated using a historical annual temperature trend near 1 m and the ground temperature profile was updated to reflect a nonlinear profile from diurnal fluctuations. The temperature data is from Fort Assiniboine, MT, Site 2019, Montana Natural Resources Conservation Services (NRCS), United States Department of Agriculture (USDA) [unpublished calculations, Jeff Bristow, WTI, MSU].

The historical diurnal ground temperature trend was fit to a sinusoidal function as follows,

$$T_g = 8.2 \cdot \sin\left(\frac{2 \cdot \pi \cdot D_{oyr}}{365} - \frac{266 \cdot \pi}{365}\right) + 10.3 \tag{71}$$

where D_{oyr} is the day of the year and T_g is the ground temperature (C°) at 1 m depth. T_g is converted to Kelvin.

The temperature profile may be obtained through simplification of the general energy equation. The energy equation for any unit volume is given as [taken from Chandrasekharaiah and Debnath 1994],

$$\rho \cdot \left(\frac{D\varepsilon}{Dt}\right) = T \circ D - div(Q) + \rho \cdot h \tag{72}$$

where $\rho \cdot \left(\frac{D\varepsilon}{Dt}\right)$ is the internal energy storage per unit volume

T•D is the mechanical work energy per unit volume

div(Q) is the heat flux crossing the surface per unit volume

ρh is the internal energy generation per unit volume

Excluding work and internal energy generation for an isotropic solid medium and limiting heat flow to one dimension, (72) is reduced to

$$\frac{\partial T}{\partial t} = \Lambda \cdot \left(\frac{\partial^2 T}{\partial z^2} \right) \tag{73}$$

where $\Lambda = \dfrac{k}{\rho \cdot C_p}$ and is known as the material thermal diffusivity (m^2/s). ρ and C_p are the density [e.g., bitumen 2203 kg/m^3, Tan et al. 1997] and specific heat (e.g., bitumen ~ 0.8812 kJ/kg-K) of the material, respectively. Applying forward differencing for the temporal derivative and a central differencing scheme for the spatial derivative,

$$\frac{\partial T}{\partial t} = \frac{T_i^{j+1} - T_i^j}{\Delta t} \tag{74}$$

$$\frac{\partial^2 T}{\partial z^2} \doteq \frac{T_{i+1}^j - 2 \cdot T_i^j + T_{i-1}^j}{\Delta z^2} \tag{75}$$

equation (73) becomes,

$$T_i^{j+1} \doteq T_i^j + \frac{\Delta t \cdot \Lambda}{\Delta z^2} \cdot \left(T_{i+1}^j - 2 \cdot T_i^j + T_{i-1}^j \right) \tag{76}$$

The profile was divided into 101 nodes separated by 1 cm. Node 101 represented the snowcover and pavement surface temperature and node 1 represented the diurnal temperature T_g. The profile was divided into three materials, sand, unbound aggregate and bitumen materials to better approximate differing thermal conductivities of the various mediums under the pavement. Each material was assigned a representative thermal diffusivity (thermal diffusivities used for sand, aggregate and bitumen are 2.5 x 10^{-7}, 4.26 x 10^{-7}, 5.36 x 10^{-7}, respectively [Tan et al. 1997]). The ground heat flux Q_g was then calculated from the temperature gradient between nodes 100 and 101 from (70). Tg represents node 100 and T_s represents node 101. k_b is the thermal conductivity of bitumen [~ 1.34 W/m*K, Tan et al. 1997] and z_g is 1 cm.

Precipitation Heat Flux. Heat flux from precipitation may warm a surface as in the case of rain falling on snow or cool the surface as for snow falling on a surface above freezing. The precipitation flux Q_p is given by [Ishikawa et al. 1999]

$$Q_p = \rho_p \cdot C_p \cdot (T_p - T_s) \cdot P_i \tag{77}$$

where C_p = is the specific heat of precipitation (J/kg*K)

ρ_p = is the density of precipitation (kg/m^3)

T_p = precipitation temperature (K)

P_i = precipitation intensity (m/s)

Vehicle Heat Flux. Ishikawa et al. [1999] developed a method to estimate IR emission based on shading time of the vehicle over the snowcover. The method considered thermal emission from the vehicles along with shading of shortwave radiation. Ishikawa et al. [1999] reported that as speed of passing vehicles increase the IR emitted to the snow surface decreases. At highway speeds there is essentially no influence from vehicles to the energy budget [Ishikawa et al. 1999]. As a result, the vehicle heat flux Q_a is nearly zero.

CHAPTER 4

RESULTS AND FINDINGS

In this chapter, (1) measured data are presented, (2) sensors and equipment are validated and (3) measurements of snow conditions on the road are used to validate the CAR. Then (4) an effort is made to model snow conditions on road to create a temporal albedo model (SOSA). The modeled data is compared to the measured data.

Results

This section provides an overview of the measured data. Initially albedo observations are introduced, then snow properties and traffic data are presented. An effort is made to determine some general trends in some of the data for modeling purposes within SOSA.

Albedo

Measurements of albedo are shown in Figure 16. A noticeable and important characteristic is the large and rapid variation in albedo on the road. The mean albedo was near 0.299 with a large sample standard deviation (STD) of 0.197. The upper limit of albedo observed was near 0.8 while the lowest limit was for wet asphalt pavement near 0.07.

A large variation in albedo for the total road surface is also present at the three regions designated (1) on the road in wheel tracks R1, (2) on the road not in wheel tracks R2 and (3) on the shoulder R3 (Figure 17). The shoulder on average tended to have a higher albedo (0.414) being about twice that observed over the lanes, mean albedo of R1 and R2 were 0.255 and 0.287, respectively. The shoulder experienced the largest variation in albedo (STD = 0.221). Again, R1 and R2 in the lane had similar fluctuations in albedo, having STDs of 0.171 and 0.189, respectively. Large variations in snowcover and impurity concentration were visually apparent at the three areas.

The variation is snow albedo is a result of the extreme inhomogeneous snowcover on the roadway. As discussed, vehicle traffic compacts and erodes snow depending on the liquid water content. The vehicle actions form large undulations of the snowcover across the road. In addition, the random distribution of sanding materials by maintenance operations is further complicated by the erratic redistribution by vehicles. These factors act in concert to cause the inhomogeneous snowcover and impurity concentration found on roads.

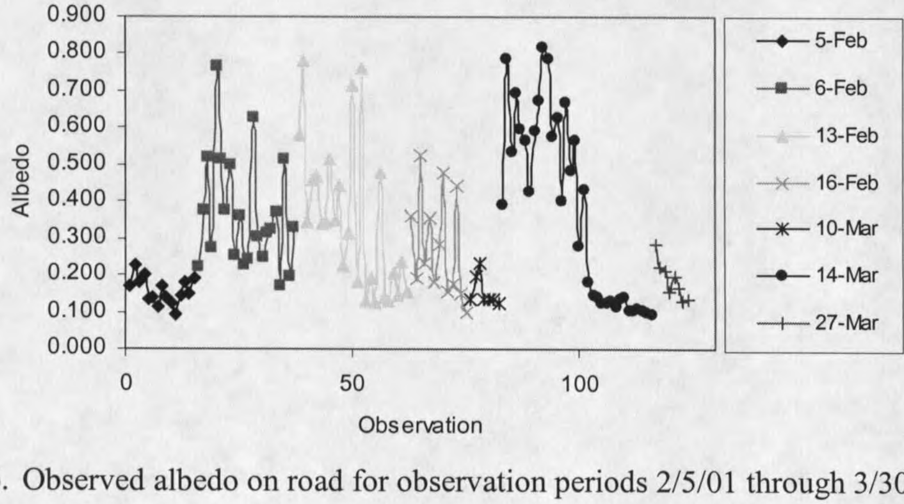

Figure 16. Observed albedo on road for observation periods 2/5/01 through 3/30/01.

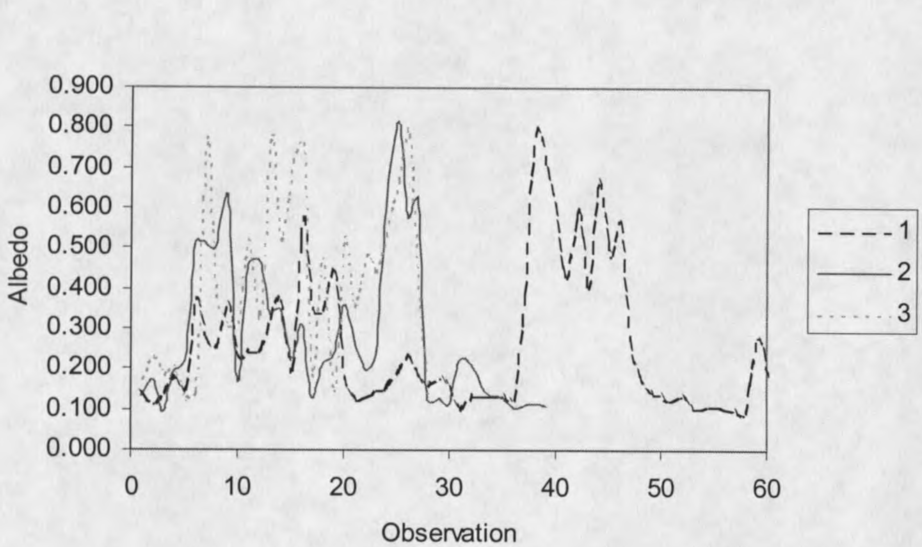

Figure 17. Measured albedo for different location on the road for observation periods 2/5/01 through 3/3/01.

Allwave albedos of some homogenous surfaces were measured with the Li-Cor LI-200SA pyranometer: dry aged asphalt, wet aged asphalt, wet/damp sanding materials and dry sanding materials (Figure 18). Measurements were performed under clear skys near noon to minimize zenith cosine effects. Albedo of dry aged asphalt (Figure 18, (a)) compared well to published values [~0.12, Pomerantz et al. 1999]. The slight difference may be attributed to differing aggregate and exposure of aggregate between pavements observed. When liquid water covers asphalt pavement, the albedo is slightly lowered to a mean of 0.07 (Figure 18, (b)) because the albedo of water at large solar angles is less than dry pavement. The solar albedo of water for diffuse and direct (small μ_o) radiation is 0.066 and less [Kondratyev 1969, Fig. 7.10]. At very large $\theta > 80^\circ$ the influence of water is reversed and actually acts to raise the albedo. Sanding materials showed a similar trend, as expected (Figure 18, (c) and (d)). The albedo of dry sanding materials is slightly above dry pavement, which tended to raise the albedo of dry pavement only slightly. Wet sanding abrasives have a similar influence. As a result, dry and wet/damp sanding materials were neglected in the model when snow is not present. However, water is accounted for because of the larger influence to lower albedo. SOSA uses the dry pavement albedo (0.12) for the underlying surface albedo. To account for water on the asphalt the wet pavement albedo is taken as 58% of the dry pavement albedo.

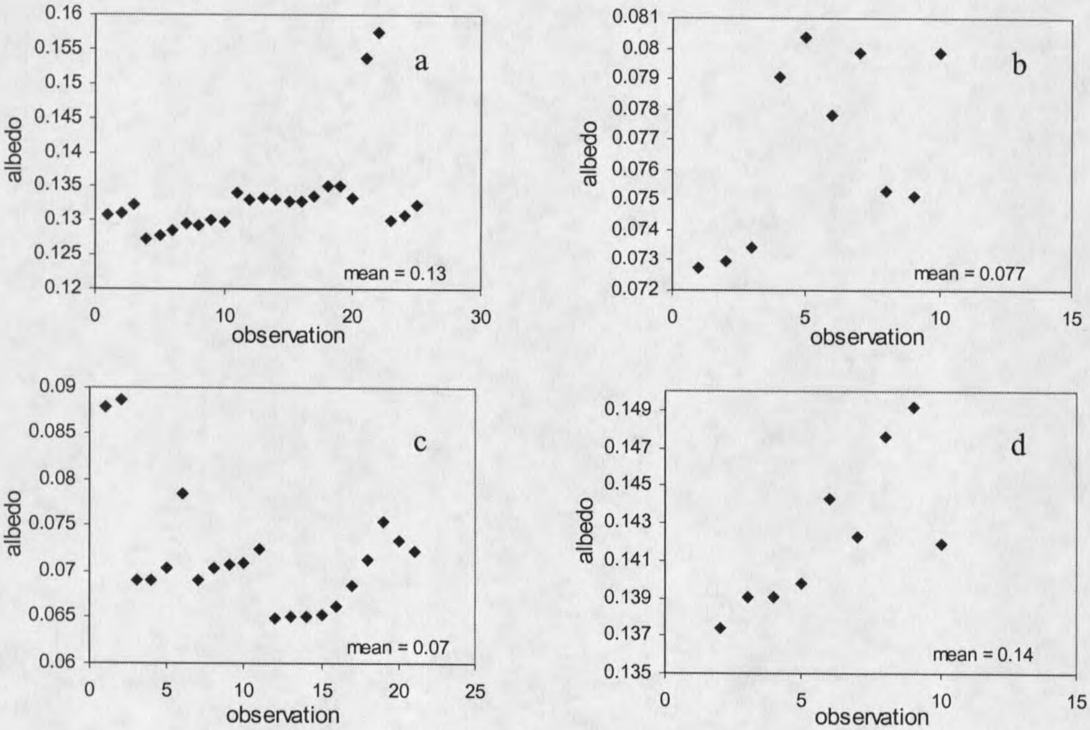

Figure 18. Allwave albedo for (a) dry aged asphalt, (b) wet dry aged asphalt pavement, (c) dry sanding materials and (d) wet sanding materials.

Snowcover Properties

Snow depth is of concern when the snowcover is optically finite. When the snow optical mass cross-section (remember when normalized to the density of ice it represents an optical path length) drops below the critical depth the underlying surface begins to influence the snow albedo and so must be included in the albedo. This is commonly the case on roads.

The large variations in snow mass cross-sections observed on the road (region 1, 2 and 3) are shown in Figure 19, STD of 0.21 g/cm^2. Overall the mass cross-section was optically thin, with the maximum near 1.13 g/cm^2 and a mean of 0.1972 g/cm^2.

Snow depth differed for the three regions (Figure 20). R1 consistently had a lower mass cross-section (mean 0.1046 g/cm^2) and showed the least amount of variation (STD = 0.095 g/cm^2). The lower mass cross-section is attributed to maintenance practices and vehicle wheels removing snow from the lane. R2 on average had more snow (mean of ~ 0.21 g/cm^2) but had larger variation (STD = 0.21 g/cm^2) because of vehicles erratically redistributing snow over the road. The shoulder (R3) had the most snow (0.3624 g/cm^2) because it had less influence from vehicles, which commonly stayed in the lane while passing the site. Winter maintenance operations frequently plowed on the shoulders when the geometrical snow depth got too great which contributed towards the larger variation (STD = 0.2879 g/cm^2).

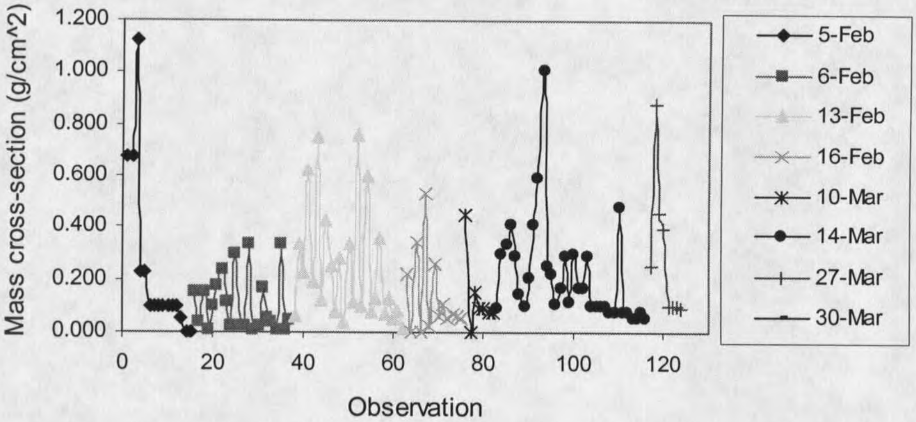

Figure 19. Observed snow mass cross-section (g/cm^2) from 2/5/01 through 3/30/01.

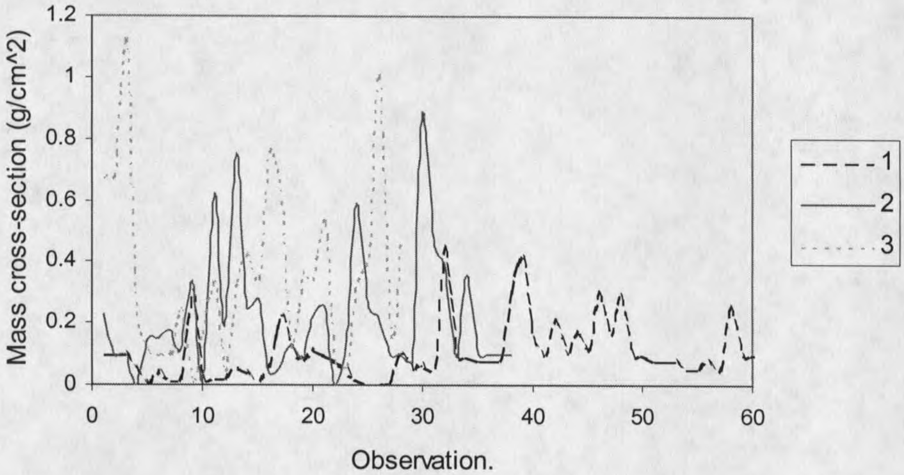

Figure 20. Snow mass cross-section for different locations on road from 2/5/01 through 3/30/01.

Grain sizes observed are shown in Figure 21. The three locations (1,2 and 3) on the road showed similar mean grain sizes 0.46, 0.57 and 0.42 mm respectively. STD for 1, 2 and 3 was 0.37, 0.45 and 0.17 mm, respectively.

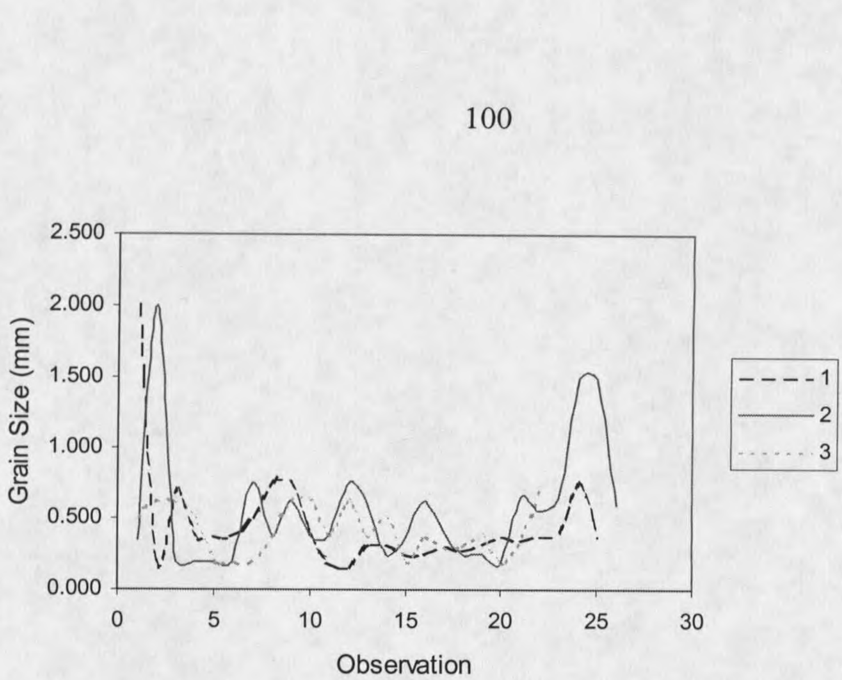

Figure 21. Measured grain size for observation periods 2/5/01 through 3/30/01.

The impurity concentrations over the measurement periods are given in Figure 22 and for the 3 regions in Figure 23. The snow in the lanes had the highest concentration of sanding materials (R1 mean = 0.368 and R2 mean = 0.362 vs. R3 mean = 0.273) because sanding operations spread antiskid materials primarily in the lanes. Actions by passing vehicles redistributed the sand over the road and threw snow and contaminates from R1 and R2 onto the shoulders and beyond. The constant redistribution of snow and contaminates from traffic seemed to be responsible for the increased variance in the contaminate concentrations (R1 STD = 0.218 and R2 STD = 0.244), because the shoulder had the lower variation in contamination with a STD of 0.132, which correlates to minimal travel of traffic in R3. This indicates that traffic is an important influence on the contaminate concentration in snow on roads.

The snow impurities contained low levels of carbon (mean ~ 0.74% by weight and STD = 0.307% by weight), which indicate that carbon has a minimal influence on the optical properties of the snow impurities on roads. This suggest that carbon contributions from vehicle tire residues, exhaust and eroded asphalt are negligible, most likely because of the short time periods snow was present on the road after accumulation and because of the large amounts of other contaminates present in the snowcover. As a result, the minimal amount of carbon in the snow impurities was neglected when normalizing snow impurities to carbon soot.

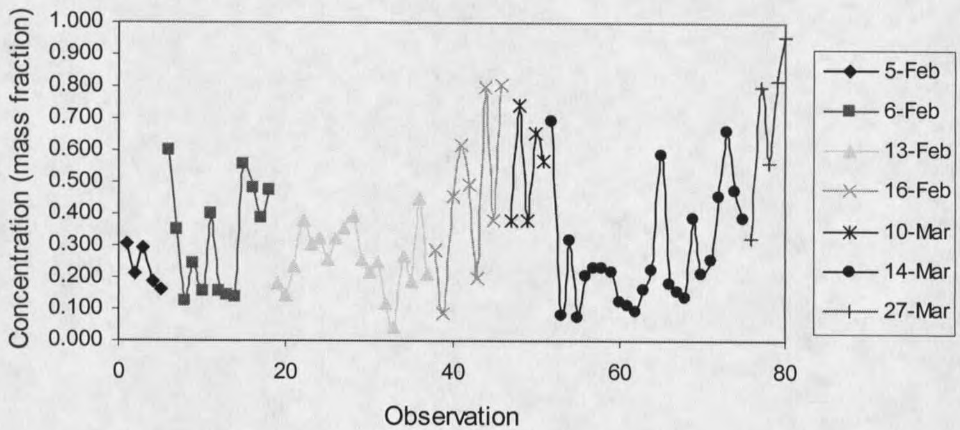

Figure 22. Observed impurity concentration (mass fraction) for observation periods 2/5/01 through 3/30/01.

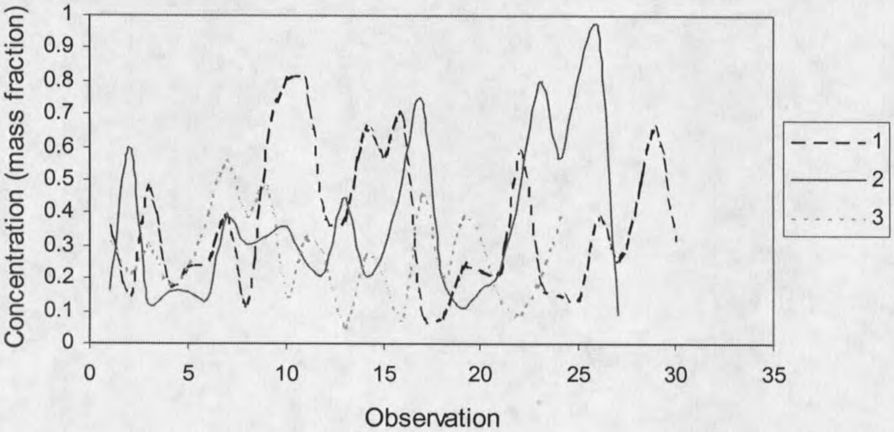

Figure 23. Impurity concentration for R1, R2 and R3 for observation periods 2/5/01 through 3/30/01.

Traffic and Winter Operations

Winter maintenance operations were monitored past the research point and are given in Table 21. On average, when snow was on the road the maintenance vehicles passed the site about 3.95 times per hour. Of the passes 93% of the time maintenance crews plowed and 36% of the time they sanded. The operations were extremely dependent upon the weather, road conditions, vehicle used and driver decisions behind the wheel. Some plow truck's gates become stuck in certain positions, which eliminates control of the flow rate of sanding materials during distribution [Personal communication with Maurice DeDycker, Division Maintenance Supervisor, MDT-Bozeman] while some truck's gates work properly. The combination of the above acting in concert during each storm occurrence contributes to highly variable anti-snow and ice operations. Insufficient data was available to compute winter maintenance patterns as a function of weather parameters and human and vehicle factors. Therefore, sanding frequency rates are input as a single value that provides a best fit to the model (based on averages of observed operations).

Passing vehicles indirectly influence the snow albedo on roads as discussed above. As a result understanding vehicle movements past the research sight is important. Traffic volumes and speed were monitored from 1/23/01 to 4/25/01, the ADT for each observation is broken down in Table 22.

Table 21. Winter operations frequency. %PlwFrqy refers to percent of passes in which plowing occurred. %SndFrqy refers to percent of passes in which sanding occurred.

Date	Pass Frequency / hr	Plow Frequency / hr	Sand Frequency / hr	%PlwFrqy	%SndFrqy
1/24/01	8.0	4.0	4.0	50	50
2/5/01	4.0	4.0	1.6	100	40
2/6/01	4.3	4.2	1.3	96	31
2/13/01	1.6	1.6	0.4	100	27
2/16/01	1.3	1.0	0.7	75	50
3/10/01	4.8	4.8	0.0	100	0
3/14/01	3.4	3.4	2.6	100	78
3/27/01	4.0	4.0	1.0	100	25
3/30/01	4.0	4.0	0.0	100	0
4/9/01	3.2	3.2	0.8	100	25
4/20/01	4.8	4.8	3.2	100	67
Max	8.00	4.80	4.00	100.00	77.78
Min	1.33	1.00	0.00	50.00	0.00
Mean	3.95	3.54	1.42	92.83	35.68
STD	1.76	1.21	1.32	16.05	24.56

Table 22. Mean ADT for 1/23/01 to 4/25/01.

	Average Daily Traffic ADT		
Date	Passing Lane	Travel Lane	Total
1/23 to 1/25			4176
2/1 to 2/8			4185
2/13 to 2/17	656	3417	4073
3/8 to 3/14	1179	3837	5016
3/19 to 3/25	1152	3870	5022
3/30 to 4/5	1216	3808	5024
4/19 to 4/25	1119	3861	4979
Max	1216	3870	5024
Min	656	3417	4073
Mean	1064	3759	4639
STD	231	192	464
%DvMean	0.22	0.05	0.10

The mean ADT for the measurement period is relatively stable near 4639 as indicated by a STD of 416, i.e., only a 10% deviation from the mean ADT. Based on data collected, ADT showed no correlation to road conditions. Therefore, a single value may accurately approximate the vehicle volumes through the corridor for the period of interest.

However, ADT lumps weekday and weekend traffic flows together and thus does not provide insight into possible vehicle volume patterns over the week. Substantial variation between the two could cause differing (degree of influence) snow conditions to occur over a week. Table 23 breaks down the average vehicles per hour, per period, daily totals and percentages for weekday, weekend and combined traffic volumes. The average daily volumes are given in Table 24 and plotted in Figure 24.

Traffic volumes through the corridor are slightly higher (~16%) on weekends than on weekdays. "Private" vehicles (axles ≤3) on average are responsible for the increase. Private vehicles increase from 78% to 84% of the total traffic, while "commercial" traffic (axles > 3) decrease from 21% to 16% of the total traffic volume from weekdays to weekends. The average weekly traffic composition is weighted towards the weekday averages being about an 80% private and 20% commercial.

The traffic is not evenly distributed between the two lanes of traffic. L2 carries the majority of the traffic volume, approximately 79% of the total vehicle volume. This varies little between weekdays and weekends. On average about 92% to 95% of commercial traffic (axle > 3) travels in L2 vs about 72% of private vehicles. When the effect of private and commercial vehicles to snow conditions on roads is better understood the traffic volume distribution may be included in the model. Presently, little data is available; therefore, commercial and private vehicles are lumped together in the model as the average period traffic APT (vehicles per 15 minutes).

Table 23. Comparison of weekend (wkend), weekday (wkday) and total week vehicle volumes. L1 and L2 refer to lane 1 and 2, respectively. CoVeh and PrVeh refer to commercial and private vehicle classification, respectively.

	L1	L2	CoVeh	PrVeh	Total
Average Hourly Traffic AHT					
	L1	L2	CoVeh	PrVeh	Total
Mean week	41	148	32	157	189
Mean wkday	39	146	34	151	185
Mean wkend	47	152	29	171	199
Average Period Traffic APT (15 minute periods)					
	L1	L2	CoVeh	PrVeh	Total
Mean week	9	34	6	38	43
Mean wkday	9	33	6	36	42
Mean wkend	11	36	6	41	47
Daily Total					
	L1	L2	CoVeh	PrVeh	Total
Mean week	931	3208	763	3376	4139
Mean wkday	857	3057	774	3139	3914
Mean wkend	1103	3555	738	3920	4658
Percentage of Daily Total					
	L1	L2	CoVeh	PrVeh	
Mean week	0.21	0.79	0.20	0.80	
Mean wkday	0.21	0.79	0.21	0.79	
Mean wkend	0.23	0.77	0.16	0.84	

Table 24. Average daily vehicles per hour. Average Vehicle per hour (Avg Hour), per period (Avg prd). The period is 15 minutes.

Weekly Traffic Trends			
DOW	Avg Hour	Avg Prd	Daily Totals
Sat	205	49	5095
Sun	193	45	4221
Mon	170	39	3755
Tue	193	43	4250
Wes	182	41	4549
Thur	155	34	2176
Fri	215	50	4819
Mean	188	43	4124
STD	21	6	963

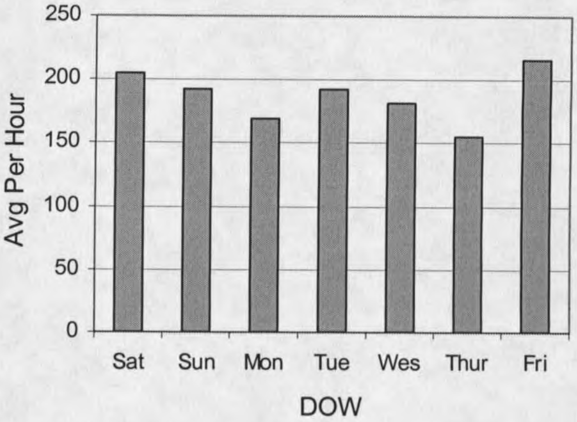

Figure 24. Average vehicles per hour by day of the week.

Traffic volumes exhibit diurnal variations. Figure 25 shows the diurnal vehicle flow rate of a typical weekday and weekend for a dry and snow-covered road. As can be seen traffic volumes reach a peak volume during morning and afternoon periods and minimal volumes for late evenings through early mornings. Weekdays exhibit an abrupt increase, near 7:00 am, that weekends did not exhibit. The sudden jump is attributed to commuter traffic. The diurnal fluctuation exhibited by both weekend and weekday traffic is approximated fairly well by weighting the APT by a periodic function for the 4 typical days in Figure 25. The polynomial coefficients were obtained by a least squares fit to a percentage of the APT to the daily mean APT and are given in Table 25. The result gives the diurnal vehicle flow rate R_{DAPT} (Vehicles/15 minutes) as follows,

$$R_{DAPT} = APT \cdot y \tag{78}$$

with

$$y = a \cdot t^4 - b \cdot t^3 + c \cdot t^2 - d \cdot t + e \tag{79}$$

where t is the time of day on a 24 hr cycle input as a decimal hour and APT represents the mean daily average traffic. The R_{DAPT} is seen fit to 4 typical days in Table 25. Figure 25, (a) and (b), also indicate no appreciable difference in traffic volumes between dry and snow covered roads during the measurement period. Therefore, weather dependence on traffic volumes is neglected in the model.

Table 25. Coefficients a, b, c, d and e for equation (79).

a	1.155×10^{-4}
b	6.333×10^{-3}
c	101.649×10^{-3}
d	400.591×10^{-3}
e	482.495×10^{-3}

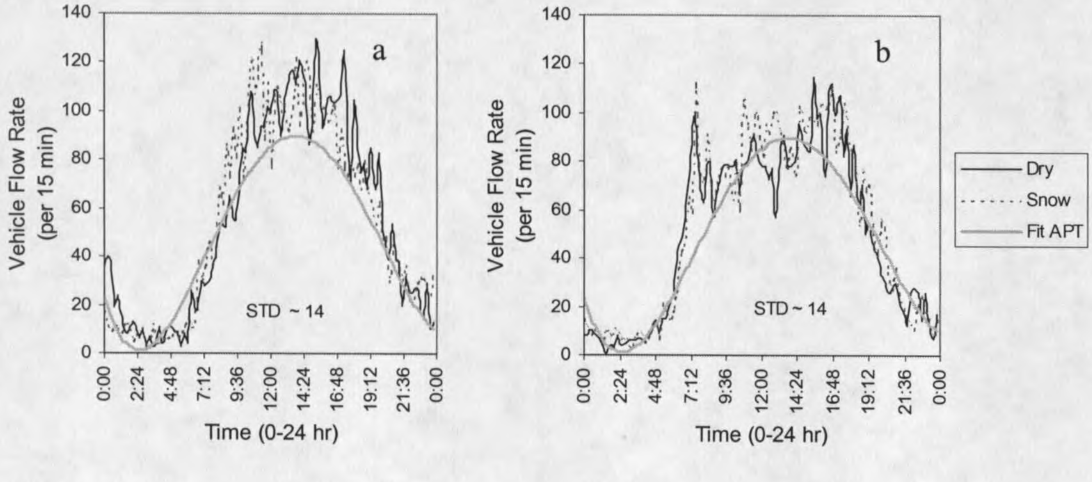

Figure 25. Average period traffic APT flow rates (vehicles per 15 minutes) for a typical (a) weekend and (b) weekday.

Findings

In this section allwave albedo is computed using CAR. CAR is initially run using observed snow properties on the road. The calculated albedo is compared to the measured albedo for validation of the routine. Then a simple temporal model is developed and compared to observed data. Validation of the temporal model is carried out through comparison of calculated surface temperature and albedo to observed values.

Validation of the Computational Albedo Routine (CAR)

As expected, initial runs of CAR showed large variation from the observed albedo at all regions on the road, STD = 0.29 (Figure 26, (a)). The level of error in the model is not attributed to the parameterization, as Marshall (1989) obtained good results with the theoretical model (WWI and WWII) producing the largest error of 8% for thin snow layers. Choosing the wavelength separation (WS) between VIS and NIR as 0.7 μm gives slightly better results (STD = 0.28) but is still drastically below measured values (Figure 26, (b)). The large error is attributed to two factors, namely snow grain size and light absorbing contaminates. Figure 27 (a) and (b), show how the model has better behavior when impurity fraction and grain size are altered. Results were nearly the same for WS = 0.9 μm. ARPS uses a wavelength separation near 0.7 μm. Therefore, the rest of CARs calculations are run with WS = 0.7 μm.

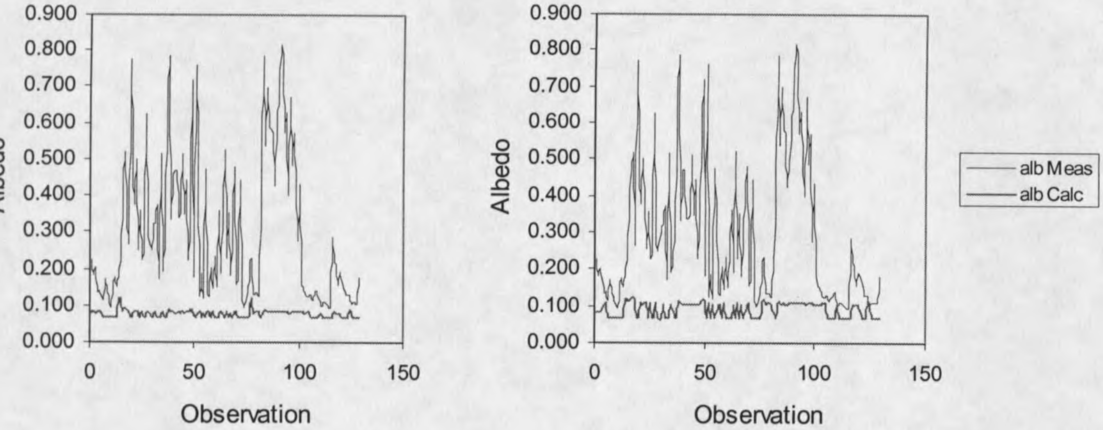

Figure 26. Measured vs. calculated albedo using CAR for wavelength separations between VIS and NIR (a) 0.9 and (b) 0.7 μm. Data are for regions R1, R2, and R3.

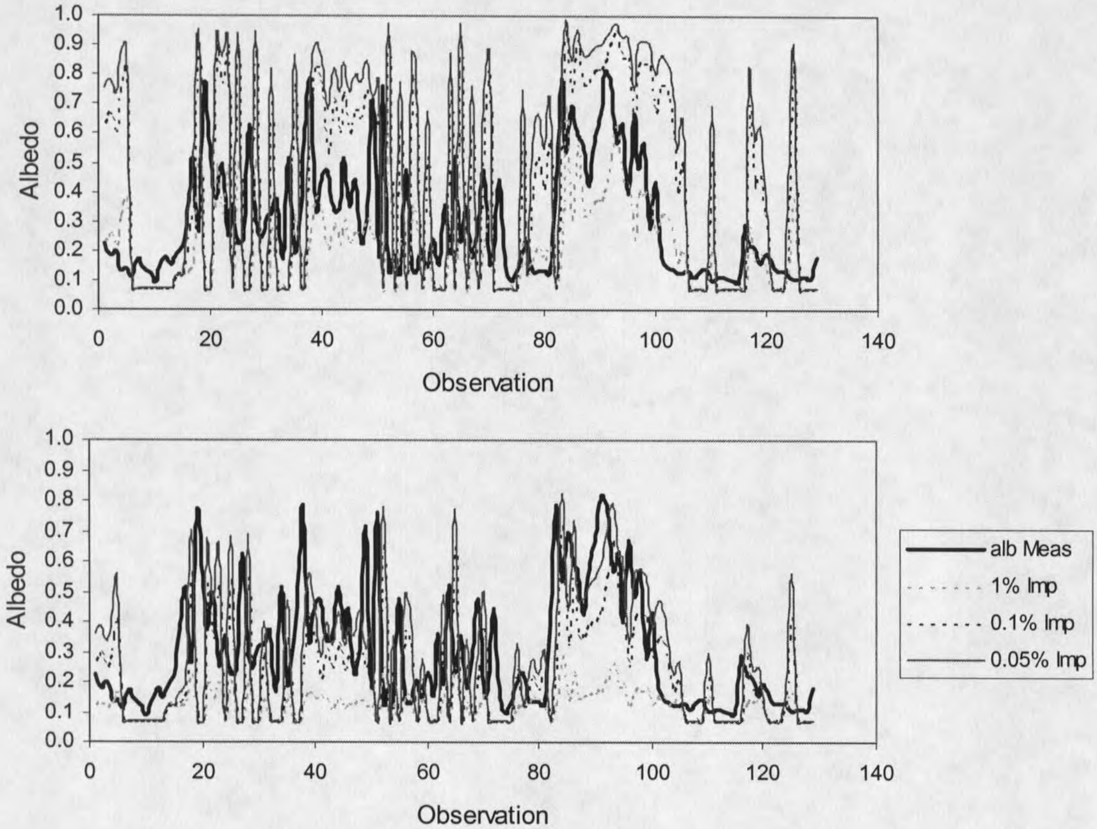

Figure 27. Measured vs. calculated albedo, using CAR for different impurity fractions. Data are for WS 0.7 (a) 1% of measured grain size and (b) 10% of measured grain size. Regions R1, R2 and R3.

Determining the Optical Grain Size in the Model. Within this section, is discussed the determination of an appropriate optically equivalent ice particle radius from observed snow grain sizes. The radius of the optically equivalent sphere is used by CAR as the effective snow grain size r_{eff} which gives the best fit to the data.

The grain size of an ice particle may be classified using (1) the equal-volume sphere, (2) the equal-surface-area sphere, (3) the equal-projected-area sphere, (4) the equal-V/A sphere, (5) half the long dimension, or (6) half the short dimension [Aoki et al. 2000]. For radiative transfer theory a common method endorsed by Giddings and LaChepelle [1961] and used by Wiscombe and Warren [WWI, WWII] is (4), an equivalent r_{va} that is proportional to V/A, the volume-to-surface-area ratio of the actual snow grain. This method requires knowledge of the geometrical structure and size of the ice particle, not considered at the time of collection, to estimate volume and surface area, which was not collected for this thesis. An alternative, to obtain a good estimate of the optically equivalent size by using a single value, as recommended by Grenfell and Warren [1999] and demonstrated by Aoki et al. [1998] comparing observed data to theoretical calculations, is to use the shortest dimension of the ice particle [similar to (6)] because it corresponds most closely to r_{va}. Aoki et al. [2000] experimentally supports this through comparison of observations of spectral albedo to theoretical albedos, requiring an r_{eff} on the order of a branch width of dendrite crystals, or less than or equal to the shortest dimension of the ice particle. Nakamura et al. [2001] also used this method to classify grain size distributions.

Aoki et al. [2000] compared in detail the relation between measured grain size and the radius of an optically equivalent sphere, employing snow pit work, image processing and spectral albedo fitting. Aoki et al. [2000] found that snow grain sizes obtained by image processing were not applicable to the optically equivalent radii. Grain sizes measured by image processing were 1.6 - 2.6 times larger than the required optically equivalent radii.

As discussed previously and seen in Figure 27, the method used to measure grain size overestimated the optically equivalent size required by the model because the longest length of the ice particle was used to classify the optical size. In order to correctly input the observed grain size into the model a relation must be applied that relates the longest to the shortest length, which better represents r_{va}.

The longest dimension may be related to the shortest dimension through the aspect ratio. A wide range of aspect ratios are present in ice crystals (1:1 spherical particles up to 80:1 for needle type, Fig. 1 [Grenfell and Warren 1999]) and snow grains, thus generalizations must be made. Aoki et al. [2000] published values for the longest and shortest dimension of snow grain radii observed in a snow pit (Table 26). By generalizing grain sizes by the maximum and minimum of the range, comparison produces aspect ratios from 1:1 to 15:1, the mean is about 6:1.

Table 26. Snow grain radii obtained from snow pit work by Aoki et al. [2000]. r_1 is ½ the longest length and r_2 is ½ the shortest length the ice particle. Partially reproduced from Table 2, Aoki et al. [2000].

1998	r_1	r_2
Feb. 22	100-750	50-100
Feb. 23	300-500	50-150
Feb. 24	100-500	50-150
Feb. 25	250-750	50-150
Mean	187.5-625	50-137.5

Aoki et al. [2000] observed the grain radii for a seasonal snowcover. On roads vehicles may break crystals which can reduce the size and hence the optical radius. Also, Nakamura et al. [2001] suggests that the "actual size distribution may shift towards smaller grains", if the smaller bonds between grains are not included in the size distribution. In this thesis a size distribution was not determined but simply a size range for snow radii. However, because of the limited magnification during inspection and the protocol employed, measurement did not include the smallest grains and bonds between grains. This probably shifted the median grain radii towards larger grains. Considering the above, it was determined to apply a general aspect ration of 10:1 for the snow particles on the road.

Application of the 10:1 aspect ratio allows a 10% reduction in the grain size input into the model and shifts grain sizes nearer to values employed by Wiscombe and Warren in their theoretical model, 50 μm for new snow and 200 μm for fine old snow [WWI, WWII]. This also agrees with Aoki et al. [2000] who required grain radii on the order of 35 to 85 μm to obtain good correlation between measured and calculated spectral albedos. Furthermore, because the snowcover was generally present on the road for relatively short periods of time, and generally while it was still snowing, it is reasonable to assume that size distributions would be better represented by small grain radii near that of new snow rather than that of old snow. For old snow Wiscombe and Warren used 1000 μm [WWI].

Snow metamorphism on roads is influenced by motor vehicles, winter maintenance practices and diurnal temperature fluctuations. The shorter existence (time period) of snowcovers on roads as compared to seasonal snowcovers can strongly decrease the influence of natural metamorphism. The natural metamorphism in a dry seasonal snowcover that drives grain growth is fueled by temperature and water vapor pressure gradients due to diurnal temperature fluctuations [Colbeck 1982, 1997] and act comparatively slower than the anthropogenic "forced" metamorphism of snow on roads. Cold temperature (200 – 260 K°) growth rates are about 0.008 mm/day. This growth rate relates to the rapid increase in grain size from 50 to 150 μm, which corresponds to the first week or two following deposition [Marshall 1989]. Warm snow grain growth occurs much faster than in cold snow [Marshall 1989] but still slow compared to snow presence observed on the road through the corridor for each storm event. The average grain growth rate for melting snow (at 5 C°) is about 0.125 mm/day [estimated from Figure 3.4, Marshall 1989]. As a result, grain growth in snow on roads does not occur as it does in seasonal snowcovers. In fact, grain growth from natural metamorphism is a secondary influence on crystal structure on roads where actions by vehicles break up crystals, which may actually act to reverse the influence of grain growth. As a result, this suggests additional support to reduce the measured grain size to better represent the effective optical mean grain size required by CAR.

Determining the Effective Soot Content in the Model. This section discusses determination of an appropriate fraction of the actual snow contaminates to use to accurately normalize them to carbon soot. A percentage of the mass fraction is used by CAR as the effective soot value which gives the best fit to the data.

Carbon soot is a principal impurity in seasonal snowcovers and primarily comes from atmospheric aerosol pollution depositing on the snowcover [WWII]. Because most of the theoretical work to date with snow reflectance has been conducted with seasonal snowcovers, soot is the common impurity used in spectral albedo models. As a result the parameterization of snow albedo employed in this thesis uses soot as a basis to weight the influence of other light absorbing contaminates on the albedo.

As discussed earlier, the impurities present in snow on and near roads differs from seasonal snowpacks in size distributions, concentration and characteristic absorbing properties, as a result of maintenance practices (sanding) and vehicle actions (mechanical mixing). Impurities are in higher concentration on roads compared to seasonal snowpacks and differ in their optical properties. Contaminates other than soot that are present in the snow in large concentrations must be normalized to carbon soot before input into SNOALB [Marshall 1989]. The reason is that carbon is highly absorptive compared to other contaminates present in the snow. Black carbon has a single-scattering albedo ω close to 0.5 while most other particles are around 0.9 – 1.0 [Goldberg 1985]. If all contaminates are assumed to be soot then their influence is overweighted in the model.

The imaginary part of the refractive index represents the ability of the median to dampen (absorb) light. Generalizing from this, the sanding materials were normalized to soot using the wavelength averaged imaginary refractive index, assuming that the ratio of $m_{im\ soot}$ / $m_{im\ bulk\ snow\ impurity}$ represents the normalization factor N_f. Soot is approximately 50 times more effective at reducing snow albedo than dust [Warren 1984]. Reasonable bounds of m_{im} for desert dust (r_{mean} ~ 1 μm) reported by Lindberge [1975] are 0.01 to 0.005. WWII used for dust m_{im} = 0.01 and for soot m_{im} = 0.5. Applying to the assumed normalization ratio yields 0.5/0.01 = 50, which agrees with what was approximately required by WWII to normalize dust to soot. Therefore, this suggests that a reasonable estimate of the effective soot fraction S_f in CAR may be obtained from

$$S_f = \frac{m_{xsSAND}}{N_f} \tag{80}$$

where m_{xsSAND} is the mass fraction of sanding materials and N_f is given by

$$N_f = \frac{m_{imSOOT}}{m_{imBULK}} \tag{81}$$

Additional error, probably small and included in N_f, may be inherent in the model because of the differing size between the actual contaminates in snow and assumed particulate size of impurities used in the model. The assumed radii of contaminates in the parameterized model (1 μm for dust and 0.1 μm for carbon soot [WWII]) are much smaller than the mean radius of the anti-skid materials used on the highway. Sanding materials used through the corridor range from 0.05 mm to 15 mm. It is reasonable to suggest that for the same mass of impurity, if concentrated in a single particle, it will have less of an influence than when distributed across the snowcover as a finer grain size. Wiscombe and Warren [WWII, Fig. 4.] support this point. They demonstrated the reduced influence of impurities on lowering snow albedos as their radii increased. Also, Mita and Isano [1980] reported that for identical weight-fractions of dust constituents, differing size distributions produced different "average" m_{im} values [WWII]. This suggests that there is additional support to reduce the mass fraction of the observed sanding materials for normalization to carbon soot.

Considering the above, the model was run again making adjustments to impurity mass fraction and grain radii. The effective soot concentration was input into CAR as 0.1%, 0.07% and 0.05% of the observed mass fraction of the sanding materials. The optically equivalent sphere radii were taken as 10% of the observed grain size as argued above. The improved fit to observed data is seen in Figure 28. Table 27 gives the STDs for regions R1, R2, R3 and the overall road surface.

The best overall fit by CAR, based on comparison of the STDs (~0.15) is obtained by using 0.07% ($N_f = 1500$) of the measured mass fraction of snow impurities. With $N_f = 1500$ it implies a bulk m_{im} of the sanding materials to be around 0.333×10^{-3}. In reality, m_{im} used to represent the sand is not characteristic of any pure substance in the aggregate and is a function of λ.

Table 27. STDs for Regions R1, R2, R3 with different normalization factors N_f.

Solar Albedos (WS = 0.7)			
N_f	1000	1500	2000
R1	0.126	0.122	0.127
R2	0.112	0.116	0.132
R3	0.229	0.217	0.218
All	0.152	0.147	0.153

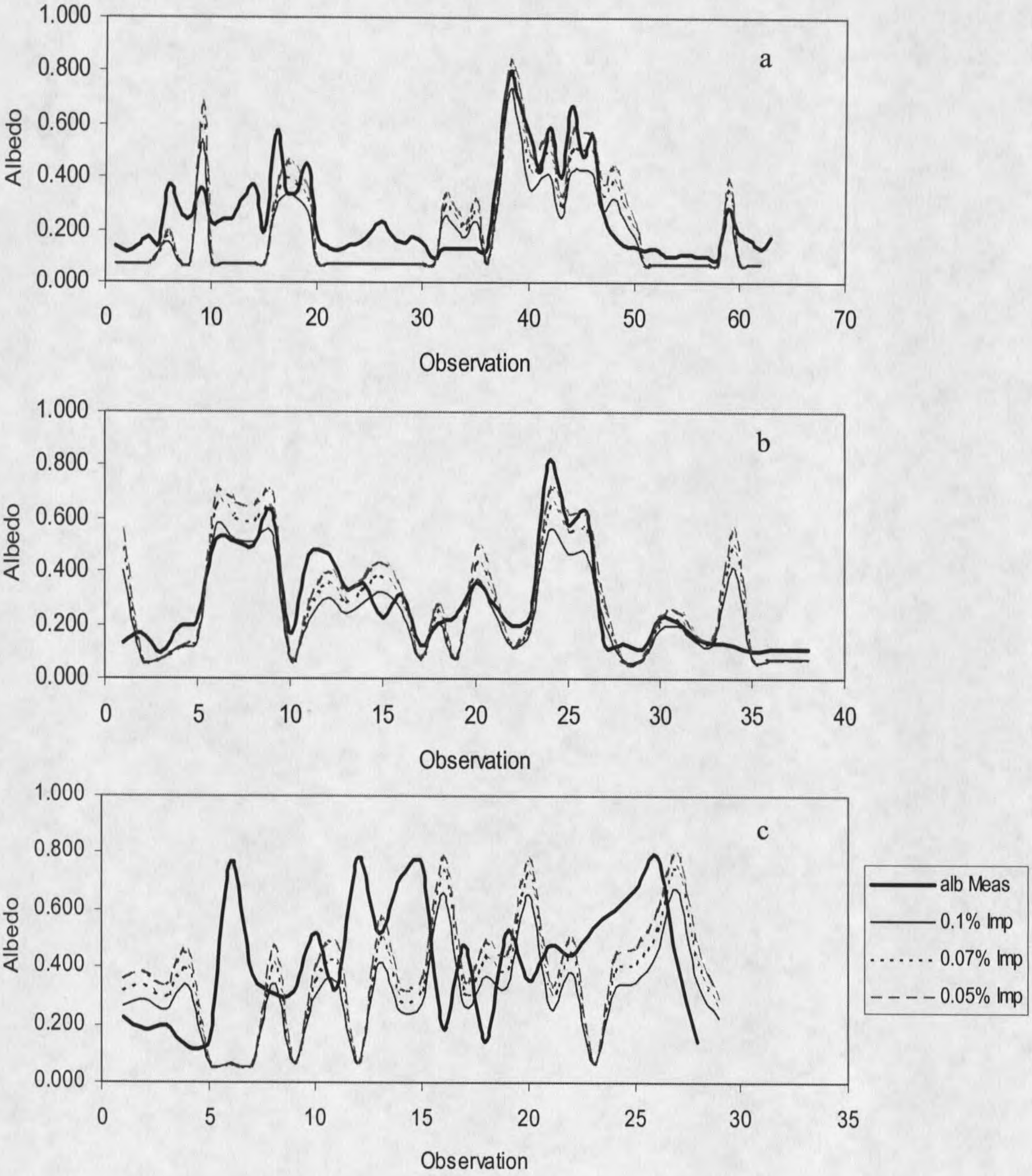

Figure 28. Measured vs. Calculated Albedo for VIS 0.7. Data represented is for (a) R1 (b) R2 and (c) R3. The normalization factor is taken as 1000, 1500 and 2000. (1) The influences of surrounding snow to raise the observed albedo above the calculated for bare asphalt. (2) The influence of surrounding bare pavement to lower the observed albedo below the calculated for snow.

The components of the sanding materials exhibiting contrasting imaginary indicies and differing particle size distributions can strongly affect m_{im} [WWII]. Changing particle and component distributions on the road may contribute to a variation in m_{im} over the surface. The magnitude of any possible variation in particle composition and m_{im} across the road was not studied and thus is neglected in this discussion.

The sanding materials consist of an aggregate mixture of basalt, granite, quartz, clay and other light absorbing impurities. The mixture may very from region to region depending on local materials. MDT-Bozeman obtains aggregate from crushed rock quarried from various local pits [Personal communication with Maurice DeDycker, Division Maintenance Supervisor, MDT-Bozeman]. The optical properties would need to be studied in detail for each region and with each new contract to obtain an accurate value of m_{im}. As a result, to make the model more universal, some assumptions were made about the sanding materials.

Inspection of the aggregate mixture suggests that the sanding materials consists chiefly of basalt and granite particles [Personal communication with Dr. David Mogk, Professor, Department of Earth Sciences, Montana State University], thus the aggregate mixture was assumed to be a mixture of the two. A standard color index was used to estimate the percentage of the darker particles to lighter particles (Figure 29). The darker particles were taken as basalt and the lighter assumed granite. The fraction of basalt $f_{balsalt}$ was estimated at approximately 0.07. Average bulk m_{im} of the sand materials was estimated from an area percentage of basalt and granite from a sample as follows,

$$m_{imBULK} = f_{basalt} \cdot m_{imBASALT} + \left(1 - f_{BASALT}\right) \cdot m_{imGRANITE} \tag{82}$$

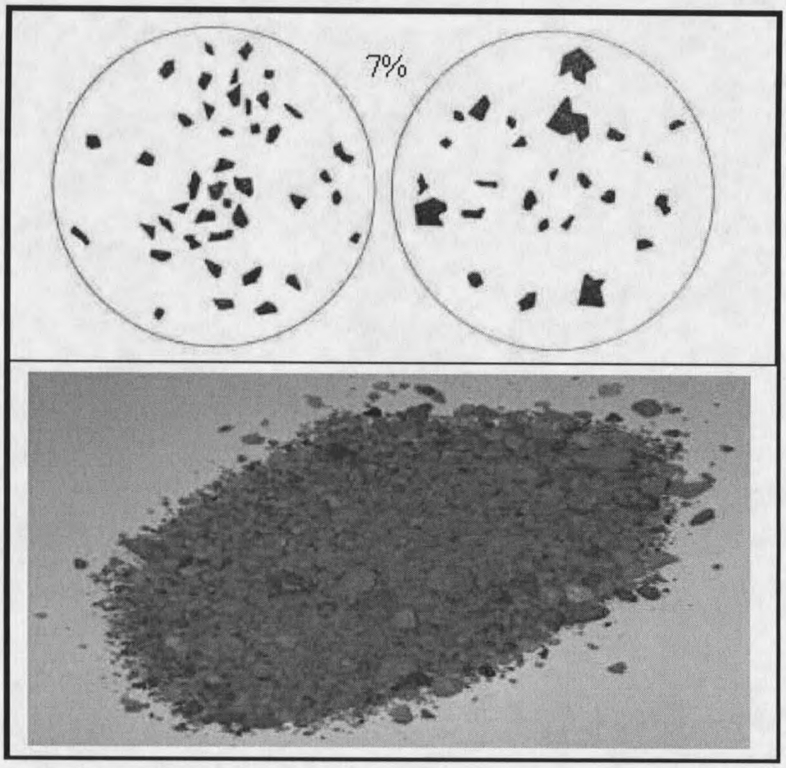

Figure 29. Sanding materials compared to the respective color index.

Representative values of $m_{im}(\lambda)$ for basalt and granite between 0.3 – 0.9 μm and wavelength averages are given in Table 28. The spectral imaginary refractive index values for granite were not directly found but were estimated from using $m_{im}(\lambda)$ of obsidian because the mineral composition of some granites are closely related to obsidian, when chemical analysis of Obsidian from Pollock et al. [1973] is compared to granite from Bagadassarov and Dorfman [1998] and Dorr et al. [1999]. Granite contains slightly more FeO (~1% more), which is highly absorptive in the VIS spectrum [WWI]. This means the actual m_{im} of granite may be a little higher than the value used to represent it. The result would be to lower N_f. Applying the average m_{im} for granite and basalt from Table 28 to (82) yields a bulk $m_{im} = 0.291 \times 10^{-3}$ for the sanding materials, the respective N_f from (81) is about 1718. This is a little larger but within range with the N_f required by CAR to obtain a good fit (Table 27). Differences may be attributed to particle size distributions and other constituents neglected in the aggregate which have conflicting m_{im}.

Table 28. Spectral imaginary refractive index m_{im} (1×10^{-3}) for basalt and granite. Granite is estimated from obsidian [Pollack et al. 1973].

Wavelength (μm)	Granite	Basalt
0.3	0.38	
0.32	0.27	0.97
0.34	0.25	0.93
0.36	0.21	0.93
0.38	0.2	0.87
0.4	0.2	0.86
0.42	0.2	0.85
0.44	0.21	0.88
0.46	0.21	0.88
0.48	0.22	0.91
0.5	0.23	0.92
0.52	0.23	0.92
0.54	0.24	0.93
0.56	0.25	0.95
0.58	0.26	0.95
0.6	0.27	0.99
0.7	0.3	1.1
Mean	0.243	0.928

CAR had different results for the three regions outlined on the road (Table 27). R1 and R2 showed the best fit having STDs of about 0.12 (Table 27). R3 had the least accuracy with an STD of 0.22 (Table 27).

A portion of the error in the fit albedos to observed values is due to measurement uncertainties, attributed to discrepancies in the measured snow conditions and observed albedo. The albedo measurements represent an area-averaged albedo of the surface seen by the instrument, while observed snow conditions represent a point specific value rather than the true area averaged value. Snow coverage on the road was commonly highly variable, changing quickly and laterally across the road. Generally, snow in R1 was quickly removed and deposited in R2. As a result, observed albedo was commonly an averaged albedo of bare asphalt and a snow covered surface. This may be visualized as a color index with different percent coverages. However, measured snow conditions (grain size, snow depth and mass fraction) input into CAR to calculate albedo depended on the coverage at the specific point below where the measurement of albedo were taken. Therefore, when no snow was below the sensor but was present in the adjacent surrounding area in view of the sensor, common in R1, it acted to raise the observed albedo above that of the bare asphalt albedo calculated by CAR. Similarly, when snow was present below the sensor, common in R2, but bare asphalt was in the surrounding area, CAR tended to overestimate the albedo based on the inputs, less so than the previous. This is apparent in 0, (b), (c) and (d). Region R3 experienced both behaviors frequently, seen by the erratic fit to observed albedo.

Eliminating conditions when no snow was present below the sensor improved the overall fit of albedo, STD = 0.107 (Figure 30). STDs are tabulated in Table 29. R3 improved the most reducing the error by about 9%. R1 also improved by about 4%. However, R2 had a slightly poorer fit by about 1%.

Table 29. STDs for Regions R1, R2, R3 eliminating conditions with no snow.

N_f	1500
R1	0.080
R2	0.128
R3	0.123
All	0.107

Overall, CAR did a relativity good job of estimating albedos based on snow conditions measured on the road. CAR calculated albedos within 15% for all regions (R1, R2 and R3) on the road. The model performed better in regions R1 and R2, within about 12% of observed values, this probably because the highly reflective snow on the edge of the road was less influential on observed albedo.

Error in the model may be related to a number of things, such as the high level of averaging which was used to estimate inputs, measurement uncertainties and the extremely inhomogeneous snowcover. A major portion of the error is attributed to measurement methods employed to classify snow conditions, because of time and safety constraints associated with working on an active highway, which did not provide an accurate average of the snow conditions within the sensors view used to measure albedo. Also, precision limitations in measurement equipment required some generalization of data to obtain inputs.

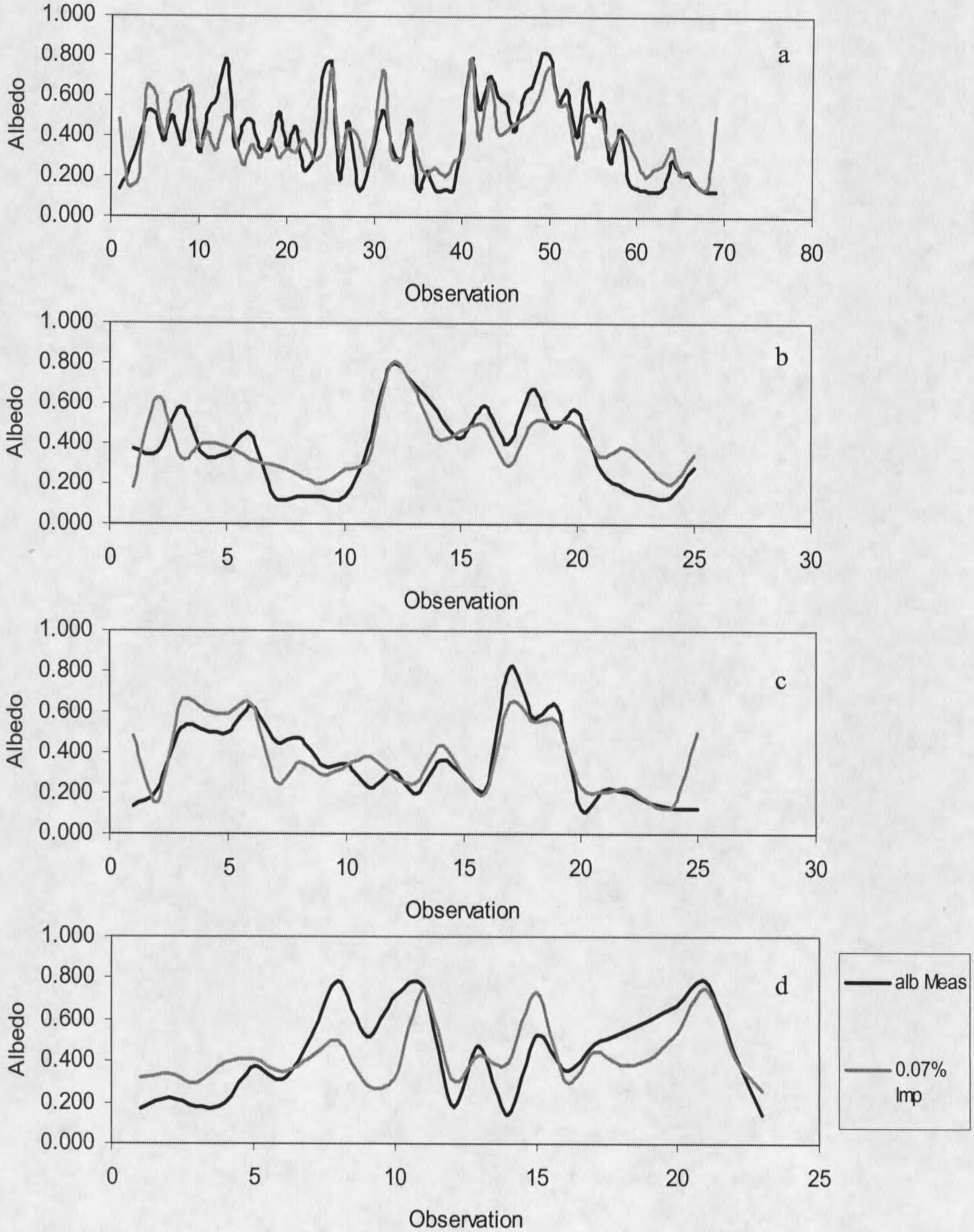

Figure 30. Measured vs. Calculated Albedo for VIS 0.7 eliminating conditions with no snow. Data represented is for (a) overall road surface (b) R1 (c) R2 and (d) R3. The normalization factor N_f is taken as 1500.

Validation of the Test-Platform

This section discusses validation of the test-platform built to provide an experimental foundation to develop the SOSA model. The test-platform simulates energy flux forecast calculations used as input to WinThermRT. However, because heat fluxes were not directly measured at the site, an additional function was included in the routine that estimates the surface temperature of the road. The test-platform then could be verified through comparison of the model's predicted surface temperatures to measured surface temperatures.

The test-platform is initially developed using data for dry road conditions to minimize influencing variables during validation of the routine. This allows the CAR and SCR to be eliminated during initial validation because albedo can be taken as a single value (~0.12) when snow is not present. Snow is introduced into the model after verification of the test-platform under dry conditions.

As mentioned earlier, longwave and subsurface ground temperature data obtained via the RWIS is suspect. Suspicion was verified when the model was run using measured RWIS data from Bozeman Hill (February 10, 2001) and the energy routine predicted temperatures drastically lower (up to 25 C below) than the actual measured surface temperatures (Figure 31). This is attributed to bad incident longwave radiation and subsurface temperature data throwing off longwave radiation and ground heat fluxes in the energy routine. Two relations were examined for use in the model to approximate incident longwave radiation. The relations are a function of air temperature, water vapor pressure and cloud cover fraction [Pluss, 1997]. Figure 32 is a plot of (83) and (84) against measured IR. It can be seen from Figure 29 that measured incoming IR shows poor agreement.

Equation (83) estimates IR under clear sky conditions using only air temperature and water vapor pressure [Brutseart 1975],

$$Q_{lw\_in} = 0.642 \cdot \left(\frac{e_a}{T_a}\right)^{\frac{1}{7}} \cdot \left(\sigma \cdot T_a^4\right) \tag{83}$$

where Q_{lw_in} = incoming longwave radiation (W/m^2)

T_a = air temperature (K)

e_a = water vapor pressure (kPa)

σ = Stefan-Boltzmann constant (W/m^2-K^4)

A relation which also includes cloud cover, (84), presented by Konzelmann et al. [1994] estimates IR,

$$Q_{lw\_in} = \left[\left[0.23 + 0.483 \cdot \left(\frac{e_a}{T_a}\right)^{\frac{1}{8}}\right] \cdot \left(1 - n^3\right) + 0.963 \cdot n^3\right] \cdot \left(\sigma \cdot T_a^4\right) \tag{84}$$

where n is the cloud cover fraction. Both relations improved the estimated surface temperature, with (84) giving the best fit overall as expected (Figure 32).

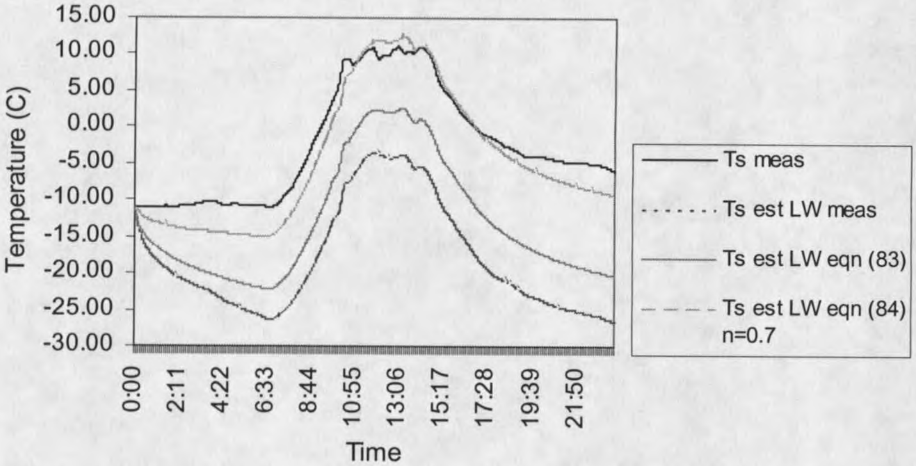

Figure 31. Measured vs. predicted surface temperatures for February 10, 2001.

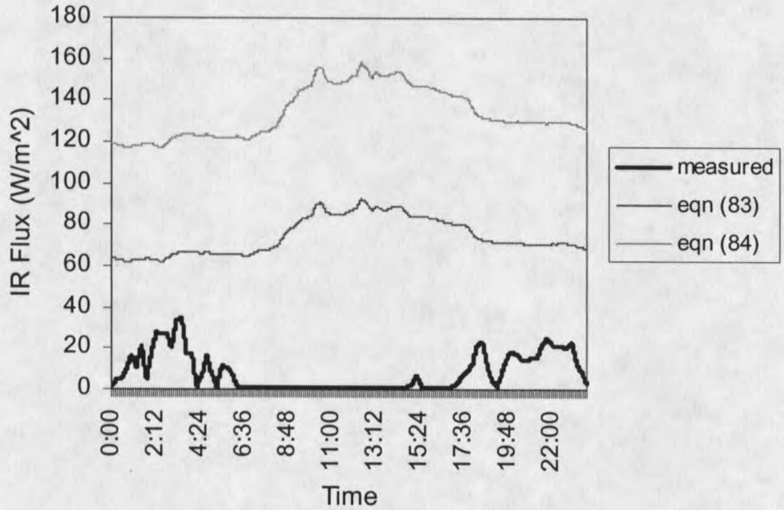

Figure 32. Measured vs. predicted incoming IR radiation flux for February 10, 2001.

The subsurface temperature sensor was also giving incorrect data. Figure 33 is a graph of subsurface temperatures at different depths over a two and half year period from Fort Assiniboine, MT, Site 2019, NRCS, USDA. As can be seen in Figure 33, the temperature at 40 inches is well behaved i.e., low sensitivity to highly oscillatory diurnal temperatures at the surface. The lowest subsurface temperature from the site in northern

Montana over the period investigated is around –7 C. The sub-surface temperature sensor (~ 50 cm deep) at the RWIS unit recorded values as low as –50 C in May, 2001 and as high as 90 C for February, 2001. These values are obviously incorrect when compared to historical temperature patterns in Figure 33, indicating to a fault in the sensor or somewhere else in the RWIS system. To eliminate error induced from bad data, the need for measured subsurface temperature data was eliminated from the model by substitution of a sinusoidal function fit to the seasonal temperature trend at 40 inches (~1 m), (71) [unpublished calculation, Jeff Bristow, WTI, MSU].

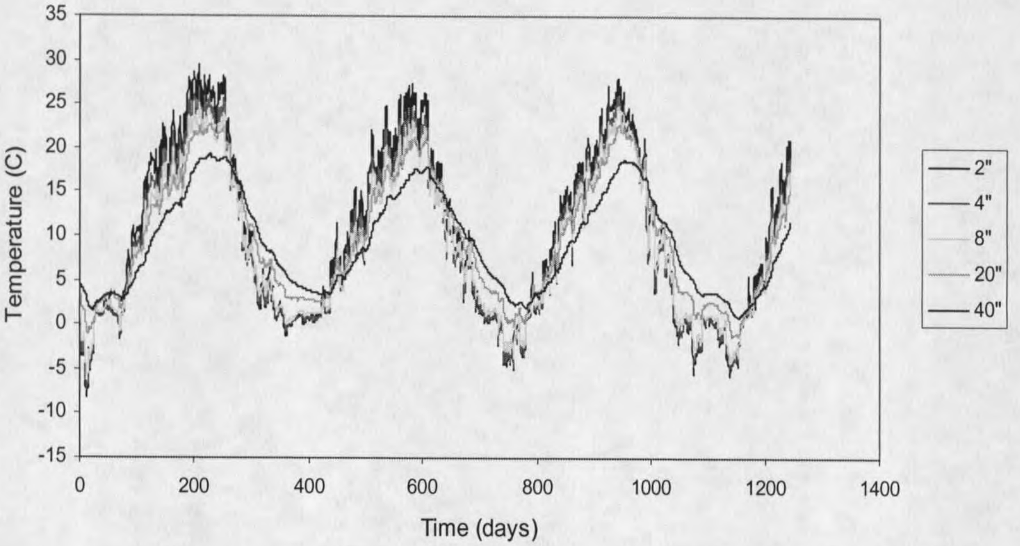

Figure 33. Ground temperature at different depths. Data from 1/1/98 to 5/31/01.

As shown in Figure 32 the model still underestimates the surface temperature by up to 8 C on February 10th, 2001 when using the fit subsurface temperature data in conjunction with equation (84). To see if the model behaved in a similar pattern under different inputs, the model was run using data from other days. Figure 34 plots the results from the 12th of May 2001. Again, the model showed similar behavior (compare Figure 32 to Figure 34). Further investigation shows that the difference is attributed to the cloud cover fraction n used in equation (84), because clouds significantly influence IR from the sky [Pluss 1997]. Figure 35 demonstrates the large influence cloud cover has on the estimated surface temperatures for varying values of n held constant over the day. Previous runs of the model had assumed that the cloud cover for the day was 30%, which greatly under estimated incident IR and hence the surface temperature. When a significant portion of incoming IR is neglected the net IR is lower than the actual, meaning the surface is emitting more thermal heat than the real surface, the result is an exaggerated surface cooling. When cloud cover fraction n_{fit} is arbitrarily varied over a single day to give the best-fit, (84) shows the improved fit between measured and modeled surface temperatures, STD = 1.3°C.

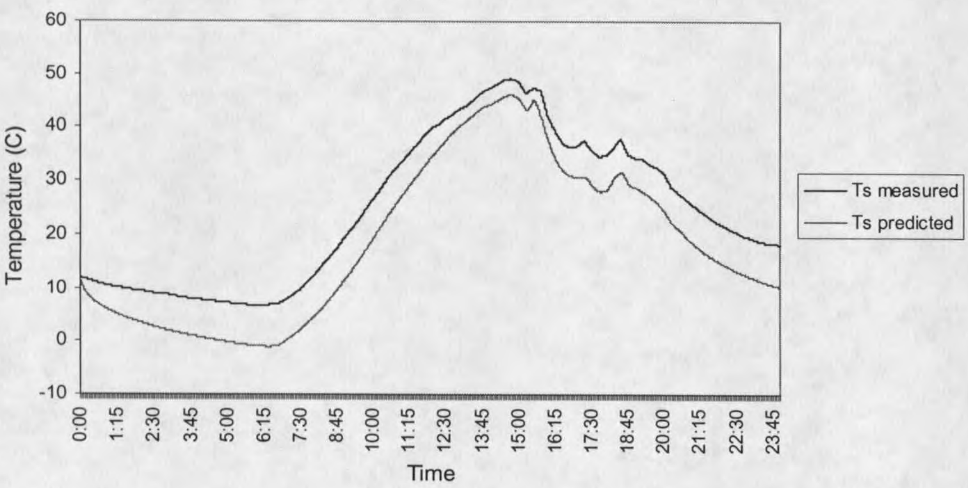

Figure 34. Measured vs. predicted surface temperature for May 12, 2001.

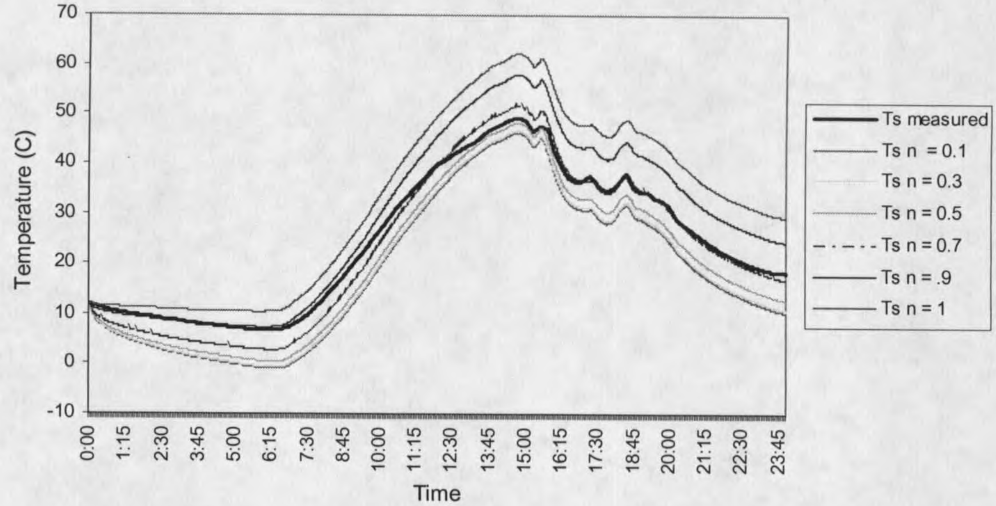

Figure 35. Measured vs. predicted surface temperature for various n factors on May 12, 2001.

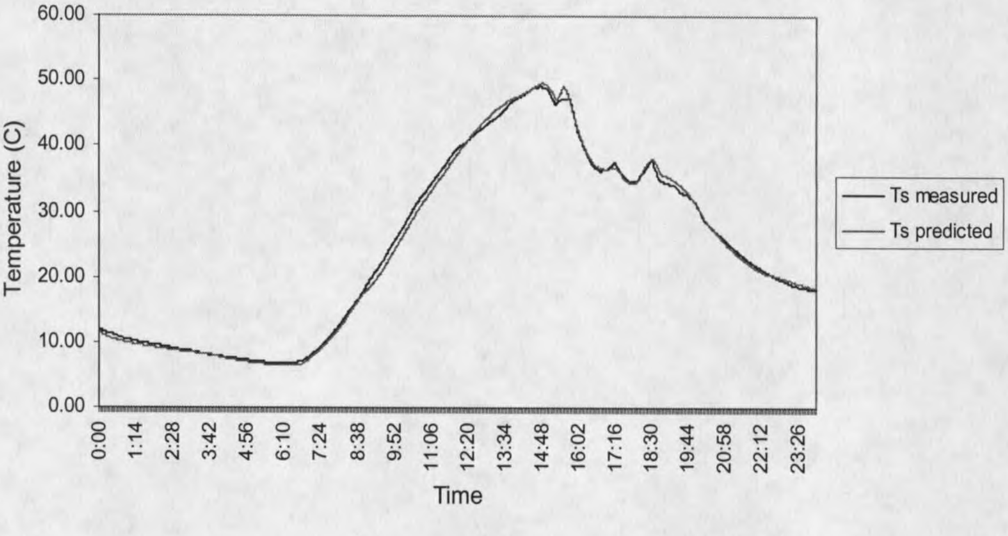

Figure 36. Measured vs. predicted surface temperature for an arbitrary n varied over the day, May 12, 2001.

The cloud cover fraction n was not measured during the observation periods. As a result, an n factor forecasted from ARPS is used as an estimate of the cloud cover for all the days analyzed. Figure 37 plots the difference in predicted surface temperature for an arbitrary cloud cover fraction that gives the best-fit n_{fit} vs. a cloud cover fraction forecasted from ARPS n_{arps}, data is for February 10th, 2001. As seen in Figure 37, n forecasted by ARPS does a relatively good job of estimating the required n to obtain a good fit, STDs for n_{arps} and n_{fit} are 1.91 °C and 0.8 °C, respectively; a difference of about 1.1 °C.

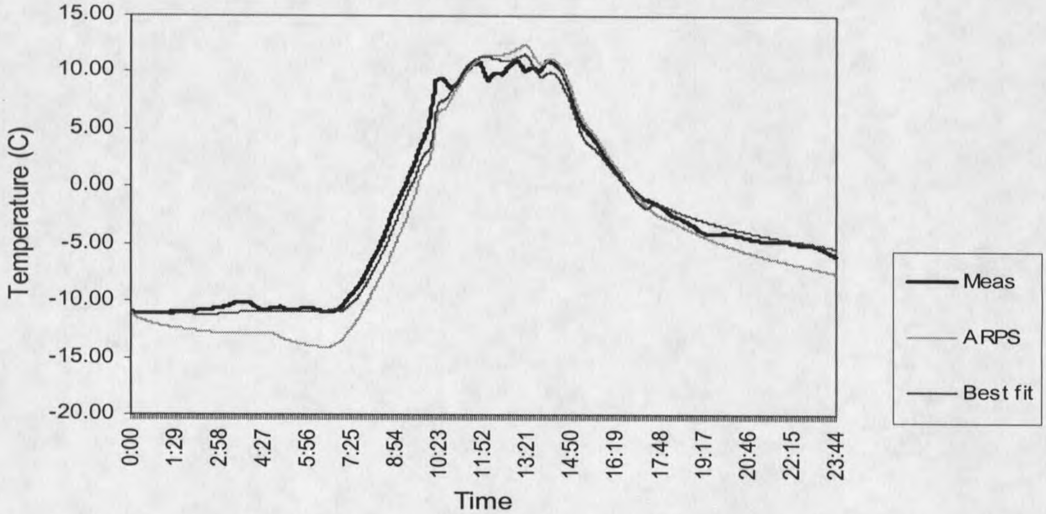

Figure 37. Measured vs. predicted surface temperature for n_{arps} and n_{fit} for February 10th, 2001.

Temporal Snow-on-Slab Albedo Model

The temporal snow-on-slab albedo model is concerned with the change in road albedo over time. It uses a simple test platform to calculate heat fluxes on the road. The test platform is intended to provide a stage to mimic thermal calculations within WinThermRT. The thermal model assumes the snowcover is thin and thus neglects heat heat conduction in the snow cover. The surface temperature is assumed to represent the temperature of the snow layer and the pavement surface. All radiant flux is assumed to be absorbed and emitted at the pavement surface. Snowmelt occurs uniformly through the snowcover with all melt water (with a mass cross-section > 1 kg/m^2 and no snow present or with a FWC > 30%) draining from the pack.

SOSA shows good results when run for a number of days chosen randomly from within the observation period. The days selected provide a brief view of possible road conditions, which may be encountered during winter periods. Theses include wet and snowy surface conditions that exhibit melt, precipitation, evaporation, and refreeze cycles. The daily 24 hr cycle is taken from midnight to midnight. Days selected are grouped by surface conditions present and are as follows,

Wet conditions

1.) 5/15/01 Initially wet to drying in the afternoon.

2.) 5/16/01 Initially dry to wet from rain precipitation to drying in the evening.

Snow conditions

1.) 2/5/01 Initially wet to icing and snowcover, melting to dry conditions with late evening snow flurries.

2.) 2/6/01 Initially dry to relatively constant snowcover conditions.

Wet to dry conditions are run in the model first to provide insight into the erosion influences of vehicles exclusive to water. When snow is not present, erosion from plowing and sanding operations may be eliminated. Initially, vehicle erosion of water VEW is neglected. Figure 38 (a) shows the suppressed afternoon temperature for May 15th 2001. Without including VEW, SOSA predicts complete drying of the road approximately 1 ½ hours after the actual road surface dries (Figure 38 (b)). Extended water presence on the road during the afternoon as predicted by SOSA is suppressing the temperature peak because net energy is converted to phase change rather than temperature change at the surface (Figure 38 (c)). Figure 39 (a) and (b) show the improved temperature fit when an estimated VEW is included, STD = 1.71 °C. The mass cross-section on the road shows good correlation to the actual surface conditions required by the RWIS road sensor. The predicted dry time is within ~ 15 minutes of the real dry time, just lagging behind. The difference can be attributed to a number of factors such as an improper value used for the water pavement saturation depth parameter of 1 kg/m^2 that is assumed in the model, uncertainty in MET and traffic inputs and lack of a sophisticated approach to include vehicle erosion influences.

A single value VEW parameter of 0.18 kg/m^2-veh is employed because it provides the best fit to the temperature and the road conditions. A number of other single values and more complicated techniques tried did not provide as simple nor as consistent results, partially because lack of data eliminated accurate modeling of vehicle erosion. In lieu of this, VEW is adopted from the snow removal rate for thick wet snow, which is approximated from Fig. 1, Schaerer [1970] (see Chapter 3, Pavement Snow Conditions Routine).

The SOSA also shows good behavior for a pavement surface experiencing intermittent periods of wet and dry conditions. During the 16th of May 2001 the research site experienced conditions of rain and sun throughout the afternoon. Runs of the model show it to be sensitive enough to reflect the rapidly changing conditions, Figure 40, (a), (b) and (c). Despite the noise and averaging inherent in the inputs, SOSA estimates the surface temperature within a STD of 1.5 °C. If water is present on the surface near the evening as temperatures drop SOSA will predict surface refreeze.

With SOSA exhibiting good behavior modeling wet-dry conditions, the model is run for conditions of snow on the road where surface albedo is a stronger player in the energy budget. February 5th 2001 initially began with a damp pavement surface accumulating snow in the early morning, melting and drying to a bare pavement in the afternoon. In the late evening snow fell for a short period, the small amount of accumulation probably never securely bonded to the surface and was wiped off by passing vehicles. An excellent fit of the surface temperature is obtained over the day, STD = 1.18 °C (Figure 41, (a)). The model is tracking surface temperatures well. Regions of constant temperature from about 3:00 to 5:00 and 9:00 to 12:00 represent snowmelt where the surface temperature is held at the equilibrium temperature between solid and liquid state. Table 30 compares the measured vs. predicted surface conditions for February 5th 2001.

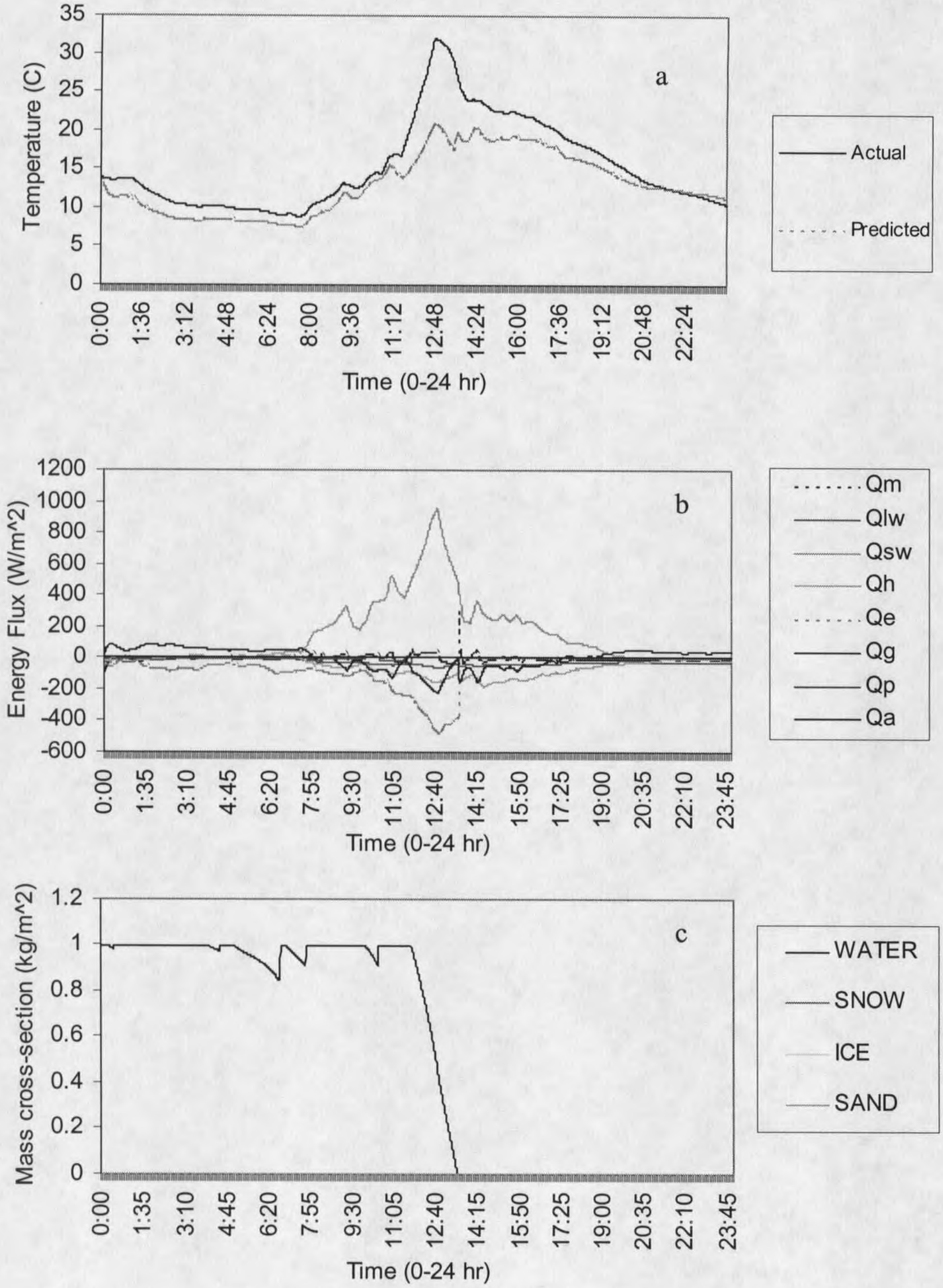

Figure 38. SOSA results neglecting VEW for May 15th 2001. The plots are (a) surface temperature, (b) energy fluxes and (c) effective depth over the day.

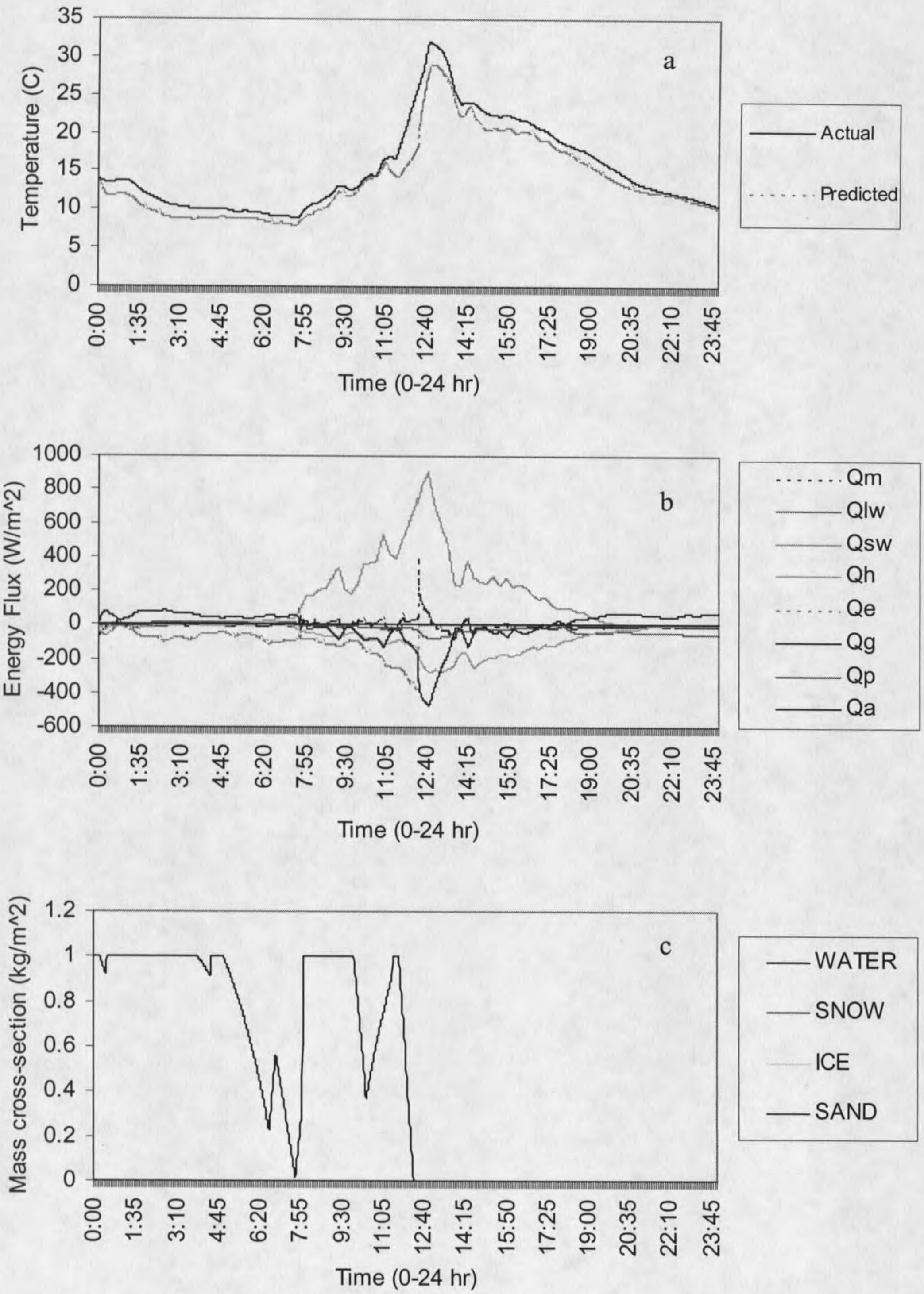

Figure 39. SOSA results including VEW for May 15th 2001. The plots are (a) surface temperature, (b) energy fluxes and (c) effective depth over the day.

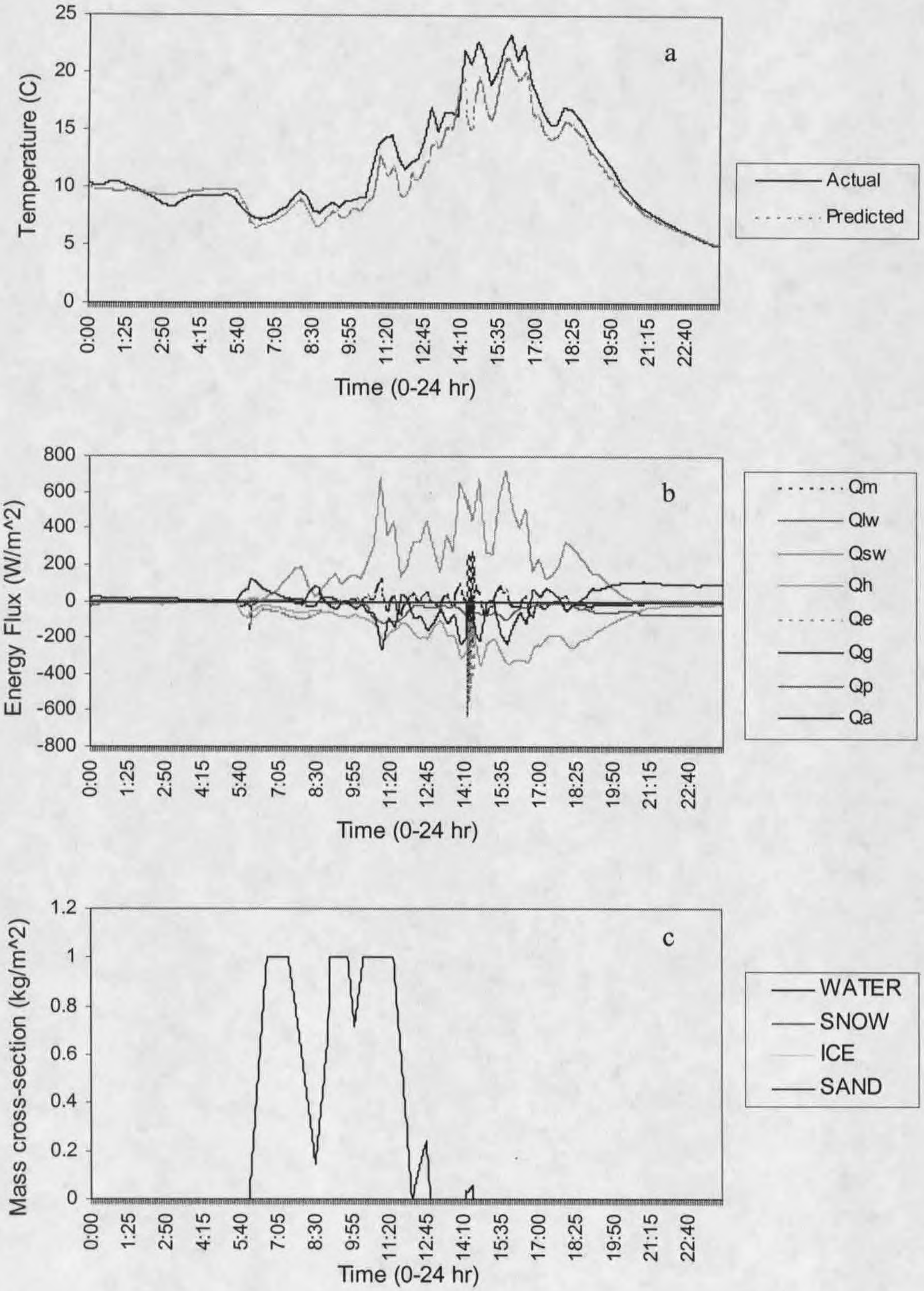

Figure 40. SOSA results including VEW for May 16th 2001. The plots are (a) surface temperature, (b) energy fluxes and (c) effective depth over the day.

Table 30. Road conditions for February 5th 2001. Measured data is from RWIS and predicted is from SOSA.

<table>
<tr><th colspan="6">Road Conditions</th></tr>
<tr><th>Time</th><th>Measured</th><th>Predicted</th><th>Time</th><th>Measured</th><th>Predicted</th></tr>
<tr><td>0:00</td><td rowspan="12">damp</td><td rowspan="7">damp</td><td>12:00</td><td rowspan="4">wet</td><td rowspan="2">wet</td></tr>
<tr><td>0:15</td><td>12:15</td></tr>
<tr><td>0:30</td><td>12:30</td><td rowspan="33">dry</td></tr>
<tr><td>0:45</td><td>12:45</td></tr>
<tr><td>1:00</td><td>13:00</td><td rowspan="32">dry</td></tr>
<tr><td>1:15</td><td>13:15</td></tr>
<tr><td>1:30</td><td>13:30</td></tr>
<tr><td>1:45</td><td rowspan="6">dry</td><td>13:45</td></tr>
<tr><td>2:00</td><td>14:00</td></tr>
<tr><td>2:15</td><td>14:15</td></tr>
<tr><td>2:30</td><td>14:30</td></tr>
<tr><td>2:45</td><td>14:45</td></tr>
<tr><td>3:00</td><td rowspan="3">wet</td><td>15:00</td></tr>
<tr><td>3:15</td><td rowspan="9">wet snow</td><td>15:15</td></tr>
<tr><td>3:30</td><td>15:30</td></tr>
<tr><td>3:45</td><td rowspan="28">wet snow</td><td>15:45</td></tr>
<tr><td>4:00</td><td>16:00</td></tr>
<tr><td>4:15</td><td>16:15</td></tr>
<tr><td>4:30</td><td>16:30</td></tr>
<tr><td>4:45</td><td>16:45</td></tr>
<tr><td>5:00</td><td>17:00</td></tr>
<tr><td>5:15</td><td>17:15</td></tr>
<tr><td>5:30</td><td rowspan="16">snow / ice</td><td>17:30</td></tr>
<tr><td>5:45</td><td>17:45</td></tr>
<tr><td>6:00</td><td>18:00</td></tr>
<tr><td>6:15</td><td>18:15</td></tr>
<tr><td>6:30</td><td>18:30</td></tr>
<tr><td>6:45</td><td>18:45</td></tr>
<tr><td>7:00</td><td>19:00</td></tr>
<tr><td>7:15</td><td>19:15</td></tr>
<tr><td>7:30</td><td>19:30</td></tr>
<tr><td>7:45</td><td>19:45</td></tr>
<tr><td>8:00</td><td>20:00</td></tr>
<tr><td>8:15</td><td>20:15</td></tr>
<tr><td>8:30</td><td>20:30</td></tr>
<tr><td>8:45</td><td>20:45</td><td rowspan="13">snow</td></tr>
<tr><td>9:00</td><td>21:00</td><td>snow</td></tr>
<tr><td>9:15</td><td>21:15</td><td rowspan="11">dry</td></tr>
<tr><td>9:30</td><td rowspan="10">wet snow</td><td>21:30</td></tr>
<tr><td>9:45</td><td>21:45</td></tr>
<tr><td>10:00</td><td>22:00</td></tr>
<tr><td>10:15</td><td>22:15</td></tr>
<tr><td>10:30</td><td>22:30</td></tr>
<tr><td>10:45</td><td rowspan="5">wet</td><td>22:45</td></tr>
<tr><td>11:00</td><td>23:00</td></tr>
<tr><td>11:15</td><td>23:15</td></tr>
<tr><td>11:30</td><td>23:30</td></tr>
<tr><td>11:45</td><td>23:45</td></tr>
</table>

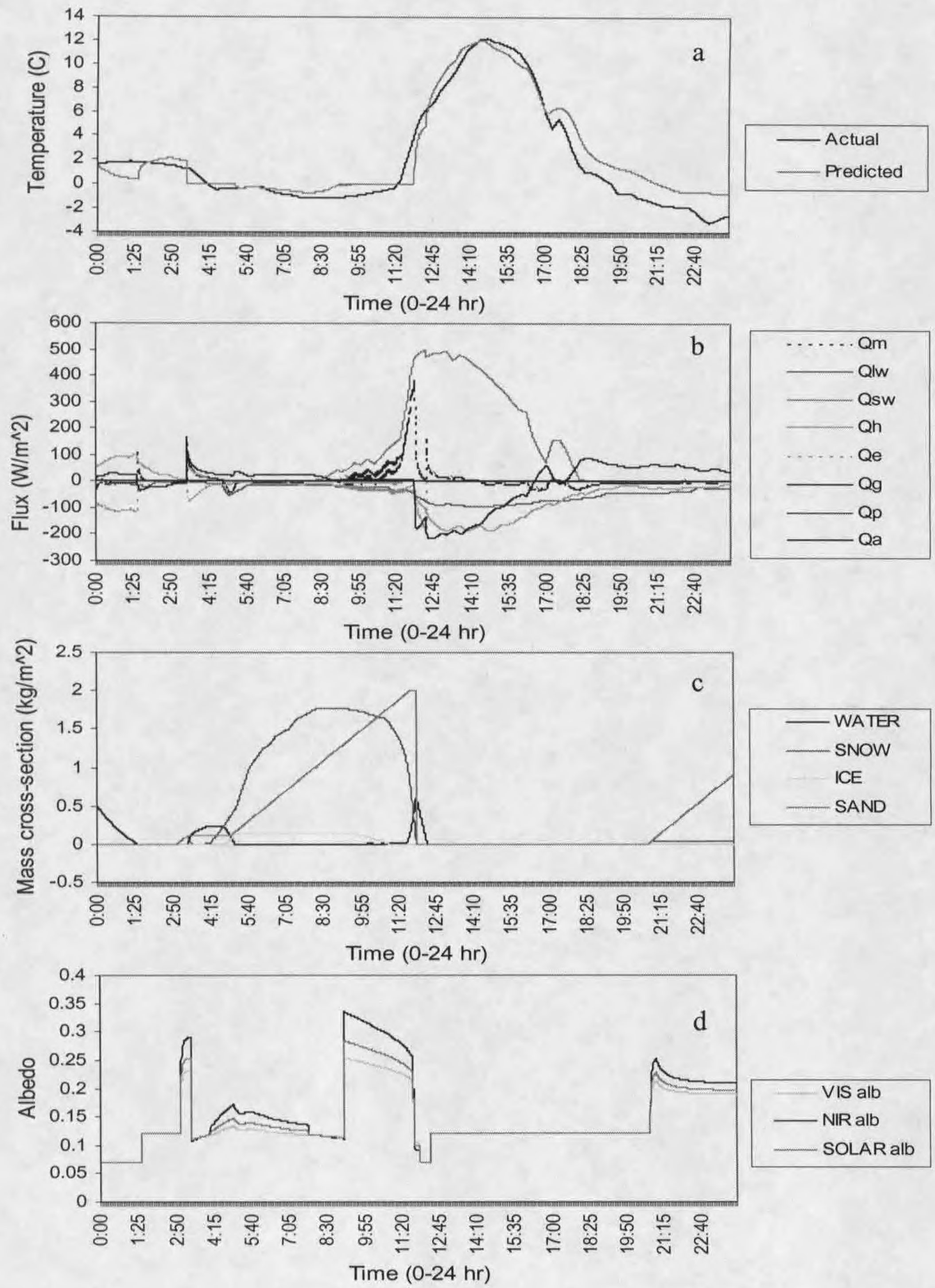

Figure 41. SOSA results including VEW for February 5th 2001. The plots are (a) surface temperature, (b) energy fluxes (c) effective depth and (d) albedo over the day.

Surface conditions predicted by SOSA compare relatively well considering the level of uncertainty in the inputs. The predicted conditions track the actual conditions within about 15 to 60 minutes. Discrepancies in the early morning and evening are attributed to the unsophisticated approach employed to include vehicle influences and uncertainties in precipitation data (intensity rate, time of precipitation, blowing snow effects, etc) and road conditions reported by the RWIS road sensor.

Premature drying of the surface near 1:30 (Table 30) correlated with a dropping surface temperature seems to suggest that the model is over estimating the actual evaporation or water removal rate. There may be a couple of factors affecting the outcome. Wind helps to increases evaporation but should not increase the evaporation rate without limit [Liaw 1973]. There is an upper limit, which is controlled by the vapor emission rate from the liquid. As it stands, the SOSA evaporation rate can increase without limit as the wind speed increases as given by (59), but this does not seem to be the primary factor because winds speeds were low near 5 – 10 m/s during the morning, which means that evaporation remained within reason. The excessive removal of water seems to be primarily related to vehicle factors. When VEW is set to zero and the model is run the road surface remains damp until 2:45. Two factors seem to be influencing this, (1) the single value assumed for VEW probably over weights vehicles influences for damp conditions and (2) the estimated APT most likely over estimated the actual APT because of the sharp increase in vehicle volumes from 0:00 to 2:00 (Figure 24), innate in the parabolic equation used to fit the traffic volumes.

A very thin amount of snow that remains on the road after 21:00, 0.4 kg/m^2 (~ 0.4 mm of 100 kg/m^3 snow), may represent snow caught between voids in the aggregate that is not compacted, melted or readily removed by passing vehicles. This snow would not remain long on the smooth flat surface of the road conditions sensor and thus the pavement sensor (Table 13) may report dry conditions when cold dry snow is actually present in small amounts between the surrounding aggregate. On the other hand, the predicted snow remaining on the road in the late evening following the short snowfall may also be a result of the model not accounting for snow removal by traffic when the FWC < 0.15. At times when the surface temperatures are well below freezing and winds are strong, snow may not stick to the pavement and be compacted but is wiped to the side of the road by passing vehicles and wind. However, snow particles may still remain in the voids between aggregate, which supports the prior reasoning. Lack of data eliminates a sophisticated inclusion of these factors within SOSA at this time.

The following day February 6th 2001 experienced relatively constant precipitation over the day, which produced reasonably stable snow conditions on the road. The day experienced a cold front, which dropped the temperature steadily over the day. The mean wind speed was near 9 m/s. Again, SOSA shows good agreement modeling the surface temperature, STD = 1.11°C (Figure 42). Comparison of the surface conditions is in Table 31. The suppressed predicted surface could be from uncertainties in cloud cover data, other MET data, or from a small insulation layer created by the snow that is not accounted for in the radiative model. The RWIS temperature sensor is located in region R2, which potentially collects more snow from wheels moving snow out of R1. Because of the relatively stable conditions over the day, snow consistently covered the sensor (R2, mean depth of 5.2 mm) and also generally in region R1 (mean depth of 2.4 mm). The thin layer of snow offers some (probably small) insulation to the surface sensor. Future inclusion of this in the model most likely will account for some differences the measured and modeled surface temperatures seen here.

The SOSA model works better for transitional periods where accumulation and melt are present during a diurnal cycle. Insufficient work has been conducted to accurately model snow and sand removal and sand deposition due to winter maintenances operations. Neglect of winter maintenance operations can be seen in Figure 42, (c). Periods of dry conditions are required to reset the sand concentration in the snow, which is presently not zeroed out until the snow mass cross-section drops to zero. Despite not including plowing and traffic influence to account for contaminate removal, the temperature results are relatively good, albedo stabilizes as the day progresses (Figure 42, (d)). This is in part due to the fact that snow is not removed from the road in SOSA when FWC < 0.15. Excessive snow left acts to balance out the sand accumulation. However, the model does not provide adequate data to road conditions after longer periods of snow coverage because of the excessive accumulation of snow and sand, which don't reflect actual conditions on the road. Improved knowledge of plow and vehicle influences on sand and snow accumulation or erosion will provide an understanding to facilitate development of a more sophisticated approach to eliminate the excessive snow and sand accumulation currently seen in the model.

Table 31. Road conditions for February 6th 2001. Measured data is from RWIS and predicted is from SOSA.

Road Conditions		
Time	Measured	Predicted
0:00	dry	dry
0:15		
0:30		
0:45	snow	snow
1:00		
1:15		
1:30		
1:45		
2:00		
2:15		
2:30		
2:45		
3:00		
3:15		
3:30		
3:45	new snow over wet compact snow	
*		
*		
23:45		
0:00		

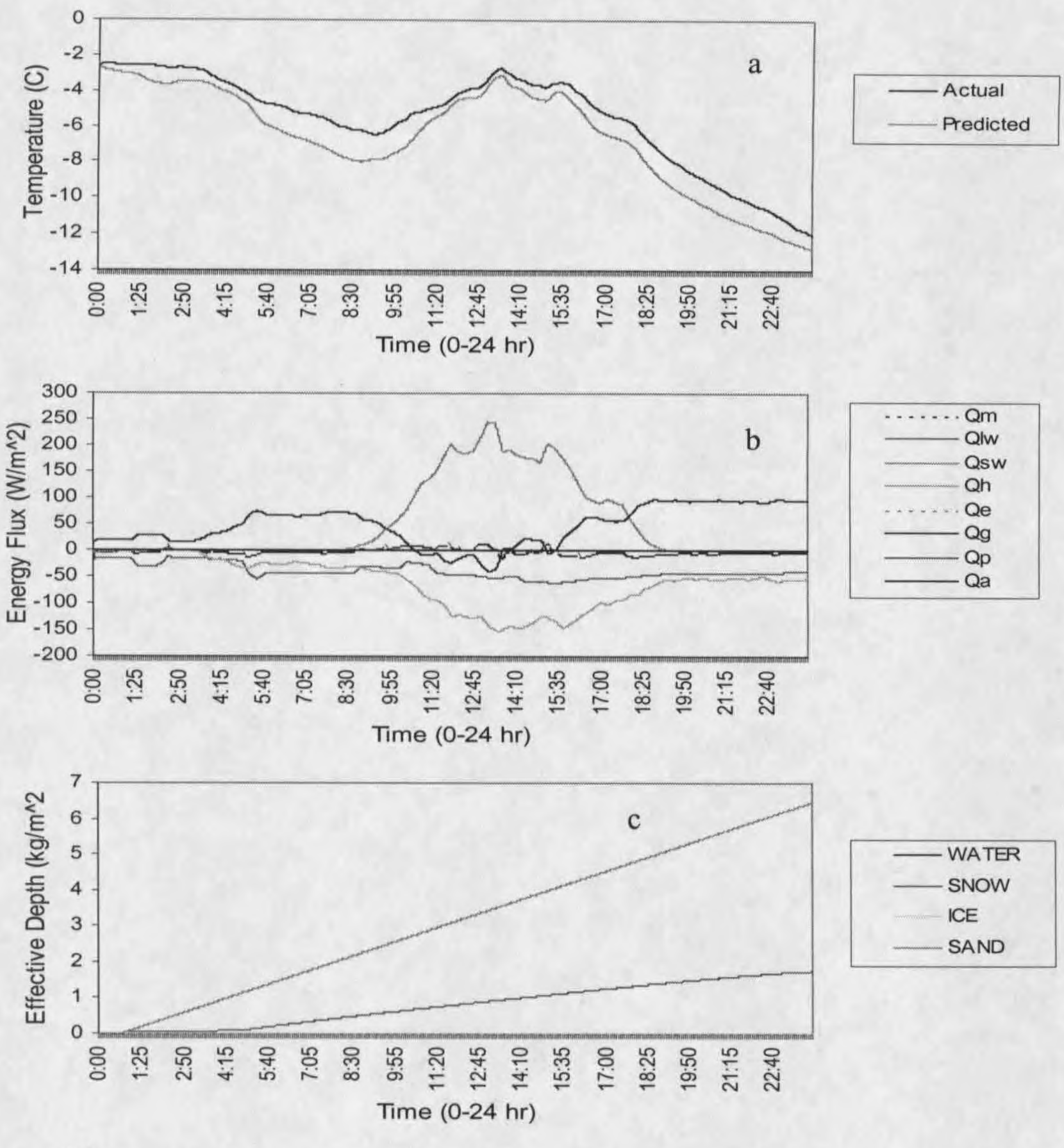

Figure 42. SOSA results including VEW for February 6th 2001. The plots are (a) surface temperature, (b) energy fluxes (c) effective depth and (d) albedo over the day.

CHAPTER 5

CONCLUSIONS AND RECOMMENDATIONS

This study develops a temporal snow-on-slab albedo (SOSA) model for use in thermal modeling of pavement surface temperatures. SOSA estimates the surface albedo by modeling surface conditions on highways that strongly affect albedo. These are effective grain size, effective impurity concentration and the mass cross-section of snow, ice, water and sand. The model is composed of two components, (1) a computational albedo routine (CAR) and (2) a pavement snow conditions routine (SCR).

The computational albedo routine accurately models the road surface albedo for dry, wet, snow and a mixture of the conditions. The routine requires on input 7 physically based parameters: snow grain radius (μm), light absorbing contaminate concentration (mass fraction), optical mass cross-section (g/cm^2), zenith cosine, atmospheric pressure (millibar), underlying surface albedo, diffuse fraction for visiable VIS and near infrared NIR, surface downflux for VIS and NIR and atmospheric transmittance for VIS and NIR. On output, the albedo model calculates a spectrally averaged VIS, NIR and solar albedo (0.3 – 5 μm). A choice in the wavelength separation between VIS and NIR (0.7 or 0.9 μm) for albedo calculations is provided.

The pavement conditions routine is an effort to temporally model snow conditions on the highway that may be incorporated into WinThermRT, which directly control albedo. SCR models the mass cross-section of water, ice, snow and sand (kg/m^2), the light absorbing contaminate concentration of the snow, and the effective snow grain size.

CAR requires as input meteorological data (air temperature, precipitation type, intensity rate, relative humidity, etc.), energy fluxes at the surface, average period traffic APT and average hourly pass rate AHP of winter maintenance vehicles. On output SCR calculates the optically equivalent snow grain size, an effective impurity concentration and a mass cross-section of water, ice, snow and sand on the pavement.

SOSA is written in C language to allow future implementation as a subroutine package to WinThermRT. All communication between WinThermRT and SOSA may be accomplished through call statements. SOSA is developed to model albedo at a single point based on the physical conditions at the grid point. Spatial variability of albedo over the terrain grid is accomplished in WinThermRT.

Prior to linking SOSA to WinThermRT a test-platform was created to provide an experimental foundation to which SOSA could be compared. The test-platform is developed to use the same meteorological inputs as WinThermRT but is spatially restricted to a single grid point.

Results of SOSA are encouraging. SOSA effectively models surface temperature for quickly changing surface conditions. Highway conditions ranged from snow and ice to dry pavement. STDs on predicted surface temperatures were no more than 1.7°C. The close fit showed that SOSA is responsive and accurate in modeling quick changes in albedo on the road. From this SOSA has accomplished the goal of better modeling albedo on the road surface. This assists in more accurate thermal modeling of surface temperatures and conditions.

The albedo routine showed good comparison in calculated to observed albedos. CAR yeilded an overall STD of 0.15 to observed results and increased to 0.11 when it was limited to predicting albedo for snow. This is quite good given the level of uncertainty in the data. The optically equivalent snow grain size required to obtain a best fit was on order of 50 – 150 μm. This required the effective grain size to be ~ 1/10 the observed grain size on the road due to measurement protocol which classified snow particle size by the longest dimension. The mass fraction of sanding materials in the snow had to be normalized to carbon soot before input into CAR. A normalization factor of 1500 was required to obtain a good fit. This means that sanding materials have 0.07% of the influence of carbon soot to lower the albedo. The normalization factor was found to be proportional to the ratio of m_{im} of carbon soot to that of the bulk sanding materials.

Future refinement in the model may come in expanding the understanding of vehicle and winter maintenance operations to snow, ice, water, and sand conditions on highways. CAR is only as accurate as its inputs. Lowering the uncertainty in the traffic factors to surface conditions is essential to improve the accuracy of SOSA. Increased understanding of traffic influences will allow refinement in the model to include a more sophisticated approach to account for vehicle and winter maintenance erosion effects and impurity deposition from sanding operations to snow conditions.

SOSA will also benefit by refinement in the treatment of radiative and thermal modeling of the snowcover. The assumption of a homogenous snowcover drastically simplifies the actual highly complicated composite structure over the road. Future work may include considerations of where radiation absorption takes place within the snowcover, such as the influence of impurity locations in the snow on the absorption of solar radiation. Also, the future inclusion of heat conduction through the snowpack would provide a more sophisticated approach and understanding to snow melt, disbonding, and erosion through the snow layer. A more sophisticated approach will generate better modeling of pavement surface conditions, which in turn will increase the accuracy of albedo calculations.

REFERENCES

Adams, E., S. McDowell. *Thermal model for snow on three dimensional terrain.* Proc. Juwsldpc. 1991.

Akhmanov, S.A., S. YV. Nikitin. *Physical Optics.* Clarendon Press, Oxford. 1997.

Aoki, T., C. Shimomura, S. Ishihira, H. Kaneko. *Sekkan taisaku chosa (I).* Doboku Kenkyujo shiryo, 1306: 1-64pp. 1977. (in Japanese)

Aoki, T., T. Aoki, M. Fukabori, Y., Tachibana, Y. Zaizen, F. Nishio, T. Oishi. *Spectral albedo observation on the snowfield at Barrow, Alaska.* Proc. NIPR Symp. Polar Meteorol. Glaciol., vol. 12, National Institute of Polar Research, Tokyo, Japan, 1-9pp. 1998.

Aoki, T., T. Aoki, M. Fukabori, A. Uchiyama. *Numerical simulation of the atmospheric effects on snow albedo with a multiple scattering radiative transfer model for the atmosphere-snow system.* Journal of the Meteorological Society of Japan, 77(2): 595-614pp. 1999.

Aoki, T., T. Aoki, M. Fukabori, A. Hachikubo, Y. Tachibana, F. Nishio. *Effects of snow physical parameters on spectral albedo and bi-directional reflectance of snow surface.* Journal of Geophysical Research, 105 (D8): 10, 219-10,236pp. 2000.

Bagdassarov, N., A. Dorfman. *Viscoelastic behavior of partially molten granites.* Tectonophysics, 290: 27-45pp. 1998.

Bohren, C.F. *Multiple scattering of light and some of its observable consequences.* Am. J. Phys., 55(6): 524-533pp. 1987.

Born, M., E. Wolf. *Principles of optics, 3rd edition.* Pergamon Press, 808pp. 1965.

Brown, B.E. *Effect of an ash fall on snowmelt rate at Paradise, Mount Rainier.* Washington Journal of Geophysical Research, 87: 1347-1350pp. 1982.

Brutsaert, W. *On a derivable formula for longwave radiation from clear skies.* Water Resour. Res., 11: 742-744pp. 1975.

Bryazgin, N., A. Koptev. *Spectral albedo of snow-ice cover.* Prob. Arctic Antarc., 29-32: 355-360pp. 1969.

Chandrasekharaiah, D.S., L. Debnath. *Continuum Mechanics.* Academic Press. 1994.

Choudhury, B.J., A.T.C. Chang. *Two-stream theory of reflectance of snow.* IEEE Trans. Geosci. Electron., GE-17: 63-68pp. 1979a.

Choudhury, B.J., A.T.C. Chang. *The solar reflectance of a snow field.* Cold Reg. Sci. Technol., 1: 121-128pp. 1979b.

Choudhury, B.J., T. Mo, J.R. Wang, A.T.C. Chang. *Albedo and flux extinction coefficients of impure snow for diffuse short wave radiation.* Cold Reg. Sci. Technol., 5(2): 119-125pp. 1981.

Colbeck, S.C. *Grain and bond growth in wet snow.* Snow Mechanics Symposium, IAHS-AISH Publ. No. 114: 51-61pp. 1975.

Colbeck, S.C. *Grain clusters in wet snow.* J. Colloid Interface Sci., 72(3): 371-384pp. 1979.

Colbeck, S.C. *An overview of seasonal snow metamorphism.* Reviews of Geophysics and Space Physics, Vol. 20, No. 1: 45-61pp. 1982.

Colbeck, S.C. *A review of sintering in seasonal snow.* CRREL Report, 97-10. 1997.

Coulter, R.G. *Understanding the action of salt.* Public Works, 96 No. 9: 78-80pp. 1965.

Dörr, W., P.A. Floyd, B.E. Leveridge. *V-Pb ages and geochemistry of granite pebbles from the Devonian Menavor Conglomerate, Lizard peninsula: province of Rhenohercynian flysch of SW England.* Sedimentary Geology, 124: 131-147pp. 1999.

Dunkle, R.V., J.T. Bevans. *An approximation analysis of the solar reflectance and transmittance of a snow cover.* J. Meteorol., 13(2): 212-216pp. 1956.

Giddings, J.C., E. Lachapelle. *Diffusion theory applied to radiant energy distribution and albedo of snow.* J. Geophys. Res., 66(1): 181-189pp. 1961.

Goldberg, E.D. *Black carbon in the environment.* John Wiley and Sons, NY. 198pp. 1985.

Gray, D.M., Male, D.H.. *Handbook of snow, principles, processes, management, and use.* Pergamon Press. 1981.

Grenfell, T. C., S. G., Warren. *Representation of a nonspherical ice particle by a collection of independent spheres for scattering and absorption of radiation.* J. Geophys. Res. 104 (D24), 31,697 – 31,709pp. 1999.

Hanbali, R.M. *Influence of winter road maintenance on traffic accident rates.* Ph.D. Dissertation, Marquette University, Wisconsin. 1992.

Hansen, J.E., L.D. Travis. *Light scattering in planetary atmospheres.* Space Sci. Rev. 16:527-610pp. 1974.

Horvath, H. *Atmospheric light absorption-Review.* Atmospheric Envir. Vol. 27A, No. 3, 293-317pp. 1993.

Hubbley, R.C. *Measurements of diurnal variations in snow albedo on Lemon Creek Glacier, Alaska.* J. Glaciol., 2: 560-563pp. 1955.

Ishikawa, N., H. Narita, Kajiya. *Contributions of heat from traffic vehicles to snow melting on roads.* Transportation Research Record-Journal of The Transportation Research Board 1672. 1999.

Jones, J.B., R.E. Dugan. *Engineering Thermodynamics.* Prentice Hall: 1000pp. 1996.

Josheph, J.H., W.J. Wiscombe, J.A. Weihman. *The delta-Eddington approximation for radiative flux transfer.* J. Atmos. Sci., 33: 2452-2459pp. 1976.

Kinosita, S., E. Akitoya. *Snow and ice on roads I.* Low Temperature Science, A27: 163-179pp. 1969. (in Japanese with English summary)

Kinosita, S., E. Akitoya, K. Tanuma. *Snow and ice on roads II.* Low Temperature Science, A28: 311-323pp. 1970. (in Japanese with English summary)

Kondratyev, K. YA. *Radiation in the atmosphere.* Academic Press, NY. 1969.

Konzelmann, T., R. Van de Wal, W. Greuell, R. Bintanja, E. Henneken, A. Abe-Ouchi. *Parameterization of global and longwave incoming radiation for the Greenland ice sheet.* Global and Planetary Change, 9: 143-164pp. 1994.

Korff, H.C., J. Gailivn, T. Vonder Haar. *Radiation measurements over a snowfield at an elevated site.* Atmos. Sci. Pap. No. 221, Colorado State University, [NTIS N74-31878/3GI]. 1974.

Liaw, Jye-Ren. *Open channel flow evaporation study.* Bonneville Power Administration, U.S. Department of the Interior: 112pp. 1973.

LI-COR. *LI-COR Terrestrial Radiation Sensors.* Type SA Instruction Manual, LI-COR, Inc.: 28pp. 1986.

Liljequist, G.H. *Energy exchange of an Antarctic snowfield-short-wave radiation (Maudheim, 71°03'S, 10°56'W).* Norwegian-British-Swedish Antarctic

Expedition, 1949-52. Scientific Results, Vol. 2, Pt. 1A, Oslo, Norsk Polarinstitutt: 107pp. 1956.

Linderg, J.D. *The composition and optical absorption coefficient of atmospheric particulate matter*. Opt. Quant. Electron., 7(Review): 131-139pp. 1975.

Maeno, N., H. Narita, K. Nishimura, R. Naruse. *Structures and new classification of snow and ice on roads*. Low Temperature Science, A46: 119-133pp. 1987. (in Japanese with English summary)

Maeno, N., H. Narita, K. Nishmura, R. Naruse. *New classification of snow and ice on roads*. Proc, 9th International Symposium On Ice, Sappora, Japan, August 23-27, 1988: 304-313pp. 1988.

Marshall, S.E. *A physical parameterization of snow albedo for use in climate models*. Ph.D. thesis, University of Colorado. 1989.

Meyer-Arendt, J.R. *Introduction to classical and modern optics*. Prentice-Hall, Inc., Englewood Cliffs, New Jersey. 1984.

Minsk, L.D. *Snow and ice properties pertinent to winter highway maintenance*. Highw. Res. Rec. 94, Highw. Res. Board, NAS-NRC, Washington, D.C. 1965.

Mita, A., K. Isono. *Effective complex reftractive index of atmospheric aerosols containing absorbing substances*. J. Meteor. Soc. Japan, 58: 69-80pp. 1980.

Nakamura, T., O. Abe, T. Hasegawa, R. Tamura, T. Ohta. *Spectral reflectance of snow with a known grain-size distribution in successive metamorphism*. Cold Regions Science and Technology, 32: 13-26pp. 2001.

Nakawo, M., M. Shimizu, S. Takahashi. *Studies of Icing on road surface in snowy region*. National Research Institute for Earth Science and Disaster Prevention, Science and Technology Agency, Tokyo. 1992.

Naruse, R., N. Ishikawa, K. Takeichi, N. Maeno. *Characteristics of ablation process of snow and ice on roads.* Low Temperature Science, Ser. A, 46. (with English summary p. 148) 1987.

Naruse, R., N. Ishikawa, N. Maeno. *Ablation process of snow and ice on roads.* Proc., 9th International Symposium on Ice, Sappora, Japan, August 23-27. 1988.

Petzold, D.E. *An estimation technique for snow surface albedo.* Clim. Bull. (McGill University), 21: 1-11pp. 1977.

Plüss, C. *The energy balance over an alpine snowcover.* Zürcher Geographische Schriften, Heft 65. 1997.

Pollack, J.B., O.B. Toon, B.N. Khare. *Optical properties of some terrestrial rocks and glasses.* ICARVS, 19: 372-389pp. 1973.

Pomerantz, M., H. Akbari, P. Berdahl, S.J. Konopacki, A.H. Rosenfeld. *Reflective surfaces for cooler buildings and cities.* Philisophical Magazine B, 79(9): 1457-1476pp. 1999.

Price, A.J., T. Dunne, S.C. Colbeck. *Energy balance and runoff from a subarctic snowpack.* Cold Regions Research and Engineering Laboratory. CRREL Report 76-27: 29pp. 1976.

Robinson, N. *Solar radiation.* Elsevier Publishing Company, NY. 1966.

Rusin, N.P. *Meteorologicheskiy: radiatsionyy rezhim Antarktidy. Leningrad, Gidrumeteorologischeskoye Izdatel'stvo.* [English translation: Meteorological and Radiational Regime of Antarctica.] Jerusalem, Israel Program for Scientific Translations, 1964: 335pp. 1961.

Schaerer, P.A. *Compaction or removal of wet snow by traffic.* Sp. Rep. 115, Highw. Res. Board, NAS-NRC, Washington, D.C.: 97-103pp. 1970.

Schneider, S. H. *Encyclopedia of Climate and Weather*. Volume I and II, Oxford University Press. 929pp. 1996.

Sergent, C., C. Leraux, E. Pougatch, F. Guirado. *Hemispherical-directional reflectance measurements of natural snow in the 0.9-1.45 μm spectral range: comparison with adding-doubling modeling*. Annals of Glaciology, 26: 59-63pp. 1998.

Serway, R.A. *Physics for scientists and engineers, 3rd edition.* Saunders College Publishing, Philadelphia. 1990.

Snyder, W.C., Z. Wan, Y. Zhang, Y.Z. Feny. *Thermal infrared (3-14μm) bi-directional reflectance measurements of sands and soils.* Remote Sens. Environ., 60: 101-109pp. 1997.

Sobrino, J.A., J. Cuenca. *Angular variation of thermal infrared emissivity for some natural surfaces from experimental measurements.* Applied Optics, 38(18): 3931-3936pp. 1999.

Sommerfeld, R.A., E. LaChapelle. *The classification of snow metamorphism.* J. of Glaciology, Vol. 9, No.55. 1970.

Stamnes, K., S.C. Tsay, W.J. Wiscombe, K. Jayaweera. *Numerically stable algorithm for discrete-ordinate method of readiative transfer in a multiple scattering and emitting layered media.* Appl. Opt., 27 (12): 2502-2509pp. 1988.

Tan, S.A., T.F. Fwa, C.T. Chuaichip, B.H. Low. *Determination of thermal properties of pavements materials and unbound aggregates by transient heat conduction.* Journal of Testing and Evaluation, 25(1): 15-22. 1997.

Van de Hulst, H.C. *Light scattering by small particles.* Wiley: 470pp. 1957.

Wallace, J. M., P. V. Hobbs. *Atmospheric Science: An Introductory Survey.* Academic Press, Inc., Orlando. 467pp. 1971.

Warren, S.G. *Optical properties of snow.* Reviews of Geophysics and Space Physics, 20 No. 1: 67-89pp. 1982.

Warren, S.G. *Impurities in snow: Efforts on albedo and snowmelt (Review).* Annuals of Glaciology, 5: 177-179pp. 1984.

White, F.M. *Heat and mass transfer.* Addison-Wesley Publishing Co.: 718pp. 1991.

Wiscombe, J., Warren, S.G. *A model for the spectral albedo of snow, I: Pure snow.* Journal of the Atmospheric Sciences, 37: 2712-2733pp. 1980a.

Wiscombe, J., Warren, S.G. *A model for the spectral albedo of snow, II: Snow containing atmospheric aerosols.* Journal of the Atmospheric Sciences, 37: 2734-2745pp. 1980b.

Yong, R.N., M. Fukue. *Performance of snow in confined compression.* Journal of Terramechanics, 14(2): 59-82pp. 1977.

Xue, M., K. K. Droegemeier and V. Wong. *The Advanced Regional Prediction System (ARPS) – A multi-scale nonhydrostatic atmospheric simulation and prediction model.* Center for Analysis and Prediction of Storms, School of Meteorology, University of Oklahoma. 2000.

APPENDIX A

SNOW-ON-SLAB ALBEDO MODEL SOURCE CODE

```
/*************************************************************
* SNOW-ON-SLAB ALBEDO MODEL (SOSA)
* MAIN PROGRAM
*************************************************************/

// LIBRARIES USED IN MAIN
#include <stdio.h>
#include <stdlib.h>

// PROTOTYPE FUNCTIONS
long double est_surf_temp(const long double Qm, const long double T_pre,
                          const long double ts, const long double mass[]);
long double adj_atm_pressure(const long double Po);
void interperlate_data(const long double in_data[][COLUMNS],
                       long double out_data[][12],const int in_rows,
                       int * out_rows);
void initialize_tt_pre(long double tt_pre[],const long double tg);
void ground_temp(long double surfaceTemp, long double tt_pre[],
                 long double ts, int loops, long double tg,
                 long double T[], int * size_t);
void initialize_tt(long double ts,long double tg, long double Ttd[]);
void energy_balance(const long double metData[][COLUMNS],
                    const long double Tt[], const long double albedo,
                    const long double mass[], const long double ts,
                    const int j,long double Q[]);
void mass_balance(const long double metData[][COLUMNS],const int j,
                  const long double Q[],const long double mo[],
                  const long double ts, long double mass[],
                  const long double amt);
double eff_grain_rad(const long double metData[][COLUMNS],const int j,
                     const long double Q[], long double mass[],
                     const double radpre);
long double trafficvolume(const double mintime);
long double mass_fraction(const long double metData[][COLUMNS],
                          const double j, const long double mo[],
                          long double mass[]);
// File Functions
void print_file_data(char * file_name, long double array[][COLUMNS],
                     int rows);
void print1dfile(char * file_name, long double array[], int length);
int  get_file_data(char * file_name, long double array[ROWS][COLUMNS],
                   int * rows, int * days);


int Albedo( int iwvl,double cosz,double ps, double rad,
        long double snowmass,long double soot, double srfalb[2],
        double dfrac[2],double sflx[2], double trans[3],
        double alb[3]);


void main(int argc, char * argv[])
{
```

```
/******************** INITIALIZE VARIABLES **********************/
    // INTEGERS //
    int rows     = 0;  // Contains the number of rows in data
    int int_rows = 0;  // Contains the number of rows in int_data
    int j        = 0;  // Counter
    int rows_tt  = 0;  // Number of rows in Ttd;
    int days     = 0;  // Contains # of days into the year
    int iwvl     = 1;  // Wavelength Seperation between VIS and NIR
                       // 0 = VIS 0.7 and 1 = VIS 0.9
    int type     = 1;  // Mass type indicator;

    // MATRICES //
    long double data[ROWS][COLUMNS];       // Contains the data read in from the data file
    long double int_data[MAXROWS][COLUMNS]; // Contains the interperted data from data file

    // ARRAYS //
    long double tt_pre[TT_SIZE];     // Used to initialize ground temp profile
    long double Q[10];               // Heat Flux Array
    long double Ttd[TT_SIZE];        // Ground temp profile array

    // Mass on road of [WATER, SNOW, ICE, FWC, SAND, SMF]
    long double mass[6]={ 0,  0,  0,  0,  0,  0 };
    // all are (kg/m^2) except FWC and SMF which are decimal fractions
    // FWC = free water content of snow
    // SMF = sand mass fraction of total snow water sand mass


    double srfalb[2] = {0.12,0.12};
    double dfrac[2] = {0.5, 0.5};
    double sflx[2] = {-1.0, -1.0};
    double trans[3] = {-1.0, -1.0, -1.0};
    double alb[3] = {0.0, 0.0, 0.0};


    // DOUBLES //
    long double ts = 60.0;       // TIME STEP (SECONDS)
    long double albedo = .12;    // APPROXIMATE ALBEDO OF DRY ASPHALT
    long double tg = 0.0;        // CONTAINS THE DIURNAL GROUD TEMPERATURE (C)
    long double Tse = 0.0;       // ESTIMATED SURFACE TEMPERATURE (C)
    long double Patm;            // Adjusted atmospheric pressure (kPa)
    long double soot = 0.0;      // Snow impurity mass fracition
    long double amt;             // Average minute traffice AMT (veh/min)
    double cosz = 0.65;          // Solar zenith cosine (degrees)
    double rad = 0.0;            // Effective snow grain radii (micrometers)
    double mintime = 0;          // Minute time on 24hr cycle (minutes)

    // CHAR'S
    char * file_name = "data.txt";     // Contains the default file name
    char * test_file = "test_out";

    // FILES
```

```
    FILE * sfc_file;   // Used to write the surface temp's to a file
    FILE * flux_file; // Used to write the flux data to a file
    FILE * alb_file;   // Used to write the albedo results data to a file
    FILE * mass_file;   // Used to write the mass result to a data file
    FILE * test_out;    // Used as test output file

/*********************** Body ******************************/

    // If an argument is given, it is used to overide the default
    // file name for input data

    if(argc > 1)
            file_name = argv[1];

    // Read the text file & get the # of rows, # of days, and
    // initialize the data matrix

    if(get_file_data(file_name, data, &rows, &days) == TRUE)
    {
            flux_file = fopen("result/flux.txt", "w");
            sfc_file  = fopen("result/sfc_temp.txt", "w");
            alb_file  = fopen("result/alb_results.txt","w");
            mass_file = fopen("result/mass_file.txt", "w");
            test_out = fopen("result/test_out.txt", "w");

            fprintf(sfc_file, "Actual\t\tPredicted\tError\n");
            fprintf(flux_file, "Qm\tQlw\tQsw\tQh\tQe\tQg\tQp\tQa\tQl_in\tQl_out\n");

            // Diurnal ground temp (tg) (c) via Jeff Bristow
            tg = 8.2 * (sin(2*PIE*days/365 - 266*PIE/365)) + 10.3;

            // Initialize data matricies for ground temperature profile
            initialize_tt_pre(tt_pre, tg);

            // Fill int_data with interpalated data from matrix data
            interperlate_data(data, int_data, rows, &int_rows);

            // Print int_data to a file
            print_file_data("result/interp_data.txt", int_data, int_rows);

            // Estimate steady state temperature profile Tt (C)
                    // 10-18-01 initialize_tt initializes Ttd to a linear state
                    // ground_temp depends on how many time it is run to determine the
                    // initial state of Ttd.
            // ground_temp(int_data[0][SURFACE_TEMP], tt_pre, ts, 5000, tg, Ttd, &rows_tt);
            initialize_tt(int_data[0][SURFACE_TEMP],tg, Ttd);

            // Print the steady state matrix to a file
            print1dfile("result/ground_temp.txt", Ttd, TT_SIZE);

            // Initialize the flux's Q (W/m^2)
            energy_balance(int_data, Ttd, albedo, mass, ts, 0, Q);
```

```
// Initialize the surface temperature
Tse = int_data[0][SURFACE_TEMP];

// LOOP THROUGH ALL THE DATA
for(j=1; j<int_rows; j++)
{
        // TRAFFIC VOLUME APT
        // Time decimal hour
        mintime = j;
        amt = trafficvolume(j);

        // ENERGY BALANCE - calculate the flux array
        energy_balance(int_data, Ttd, albedo, mass, ts, j, Q);

        fprintf(flux_file, "%f\t%f\t%f\t%f\t%f\t%f\t%f\t%f\t%f\t%f\n",
        Q[QM],Q[QLW],Q[QSW],Q[QH],Q[QE],Q[QG],Q[QP],Q[QA],
        Q[QL_IN],Q[QL_OUT]);

        // ESTIMATE SURFACE TEMPERATURE
        Tse = est_surf_temp(Q[QM], Tse, ts, mass);

        fprintf(sfc_file, "%f\t%f\t%f\n", int_data[j][6], Tse,
                        int_data[j][SURFACE_TEMP]-Tse);
        int_data[j][SURFACE_TEMP] = Tse; // Rewrite surface temp. to data

        // ESTIMATE GROUND TEMPERATURE PROFILE
        ground_temp(Tse, Ttd, ts, 1, tg, Ttd, &rows_tt);

        // ESTIMATE MASS OF WATER, SNOW AND ICE ON ROAD
        mass_balance(int_data,j, Q, mass, ts, mass, amt);

        fprintf(mass_file,/*%f\t%f\t%f\t*/"%f\t%f\t%f\t%f\t%f\t%f\n",
                mass[WATER], mass[SNOW], mass[ICE], mass[FWC],
                mass[SAND], mass[SMF]);


        // ESTIMATE IMPURITY MASS FRACTION
        soot = mass_fraction(int_data, j, mass, mass);


        // ESTIMATE GRAIN SIZE
        rad = eff_grain_rad(int_data,j, Q, mass, rad);

        // ESTIMATE ALBEDO
                // Adjust atmospheric pressure
                Patm = adj_atm_pressure(int_data[j][P_ATM]);

        if(Albedo(iwvl,cosz,Patm,rad,mass[WATER]+mass[SNOW]+mass[ICE],
                        soot,srfalb,dfrac,sflx,trans,alb)!=0)
                {
                printf("Troubles calculating albedo! exiting---\n");
```

```
                exit(1);
                }
                albedo = alb[ALLWAVE];          // UPDATE ALBEDO

                // PRINT THE VALUES TO THE FILE //
                fprintf(alb_file,"%f %f %f %f %f %f\n",
                        rad, soot, mass[WATER]+mass[SNOW]+mass[ICE], alb[VIS],
                        alb[NIR], alb[ALLWAVE]);

        }
        print1dfile("result/final/ground_temp_final.txt", Ttd, rows_tt);

        fclose(flux_file); // Close the flux file
        fclose(sfc_file);  // Close the sfc_file
        fclose(alb_file);  // Close the alb_file
        fclose(mass_file); // Close the mass_file
        fclose(test_out);  // Close the test_out
    }
    else
        printf("ERROR - reading the file %s\n", file_name);
}
```

```
*****************************************************
* ENERGY BALANCE ROUTINE
*****************************************************
#include <math.h>

// PROTOTYPE FUNCTIONS
long double adj_atm_pressure(const long double Po);
long double air_density(const long double Pa, const long double T);
long double vapor_pressure(const long double Le, const long double T,
                           const long double To, const long double Po);

// ENERGY ROUTINE
void energy_balance(const long double metData[][12], const long double Tt[],
                    const long double albedo, const long double mass[2],
                    const long double ts, const int j, long double Q[])
{
  long double n = metData[j][10]; // Cloud Cover fraction
  long double converted_temp = metData[j][0] + 273.15; // Convert air temp to Kelvins

  long double Cp = 0.0003*(converted_temp*converted_temp) // Heat capacity of air
                                    - 0.1310*converted_temp+1017.15;
  long double Pa = adj_atm_pressure(metData[j][P_ATM]); // Atmospheric pressure (mmbar)
  long double pa = air_density(Pa, metData[j][AIR_TEMP]); // Air density (kg/m^3)
  long double e_a; // Air water vapor pressure
  long double e_s; // Surface water vapor pressure
  double Le = LEV;    // Latent Heat of transfermation


// WATER VAPOR PRESSURE

    //if (mass[WATER] > 0 ) Le = LEV;
    //else Le = LES;
  // Air liquid vapor pressure (kPa) - accounting for the relative humidity of the air
  e_a = vapor_pressure(Le, metData[j][AIR_TEMP], 0.01, 0.61173) * metData[j][RH]/100.0;

  // Surface liquid vapor pressure (kPa)
  if(j==0)
    e_s = vapor_pressure(Le, metData[j][SURFACE_TEMP],0.01, 0.61173);
  else
    e_s = vapor_pressure(Le, metData[j-1][SURFACE_TEMP], 0.01, 0.61173);

// LONGWAVE RADIATION HEAT FLUX

 // Incoming IR cacluated using equation 5.3 (Pluss, 1997)
 Q[QL_IN] = ((0.23 + 0.483 * pow((e_a/(metData[j][0]+273.15)),(1/8))) * (1-pow(n,3)) +
                (0.963*(pow(n,3))))*S_B*pow(metData[j][0]+273.15, 4);

 // Outgoing IR
  if(j == 0)
      Q[QL_OUT] = E*S_B*pow(metData[j][6] + 273.15,4);
  else
```

```
    Q[QL_OUT] = E*S_B*pow(metData[j-1][6] + 273.15,4);

  // Net IR
  Q[QLW] = Q[QL_IN] - Q[QL_OUT];

// SHORTWAVE RADIATION HEAT FLUX
    Q[QSW] = metData[j][8]*(1-albedo);

//  SENSIBLE (CONVECTIVE) HEAT FLUX
    if(j==0)
            Q[QH] = pa*Cp*KH*metData[j][3]*(metData[j][0] - metData[j][6]);
    else
            Q[QH] = pa*Cp*KH*metData[j-1][3]*(metData[j][0] - metData[j-1][6]);


// LATENT HEAT (EVAPORATION) FLUX

    if(mass[WATER] > 0)
    {
            if (j==0)
            Q[QE] = 0.622*pa*Le*KE*metData[j][WIND_SPD]*(e_a - e_s)*(1000.0/(Pa/10));
            else
            Q[QE] = 0.622*pa*Le*KE*metData[j-1][WIND_SPD]*(e_a - e_s)*(1000.0/(Pa/10));
    }
    else
            Q[QE] = 0.0;


// GROUND HEAT FLUX //
  Q[QG] = KG*(Tt[99] - Tt[100])/H;


// PRECIPITATION HEAT FLUX

 if((metData[j][4] == RAIN) || (metData[j][4] == SNOW))
    // Precipitation type: snow=2, rain=1, none=0
  {
   if(j == 0)
     Q[QP] = PW*CPW*(metData[j][AIR_TEMP]-metData[j][SURFACE_TEMP])*
                         (metData[j][PC_RATE]/360000);
   else
     Q[QP] = PW*CPW*(metData[j-1][AIR_TEMP]-metData[j-SURFACE_TEMP][6])*
                                    (metData[j-1][PC_RATE]/360000);
  }
  else
            Q[QP] = 0;

// VEHICLE HEAT FLUX
Q[QA] = 0; // NOT SIGNIFICANT DUE TO HIGH VEHICLE SPEEDS

// CALCULATE NET HEAT FLUX AT SURFACE
Q[0] = Q[QLW] + Q[QSW] + Q[QH] + Q[QE] + Q[QG] + Q[QP] + Q[QA];
```

```
/*****************************************************************
* MASS BALANCE ROUTINE
*****************************************************************
This function approximates the mass cross-section of snow, ice and water on the
pavement. A vertical column with unit area is used. Small amounts
of evaporation and sublimation are neglected when snow and ice are
present.

OUTPUT
    mass[] = [WATER, SNOW, ICE, FWC, SAND, SMF]
    where:  mass     mass of H20 (solid or liquid) on road (kg/m^2)

INPUT
    metData = meteorological data
    Q         Net Heat flux (W/m^2)
    mo        previous mass on road[WATER, SNOW] (kg/m^2)
    ts        time step (sec)

*****************************************************************/

#include <stdio.h>

long double mass_transfer(const long double Qm, const long double Le,
                                        double b);
void mass_balance(const long double metData[][COLUMNS],const int j,
                        const long double Q[],const long double mo[],
                        const long double ts, long double mass[],
                        const long double amt)
{
 // INITIALIZE MASS TRANSFERS TO ZERO
  long double melt = 0;          // Snow and Ice melt (kg/m^2)
  long double evapmass = 0;  // Evaporated mass (kg/m^2)
  long double frostmass = 0; // Frost mass (kg/m^2)
  long double accumsnow = 0; // Accumulated Precipitation SNOW (kg/m^2)
  long double accumrain = 0; // Accumulated Precipitation RAIN (kg/m^2)
  long double evs = 0;// Erosion of snow mass by vehicles (kg/m^2)
  long double evw = 0;           // Erosion of water mass by vehicles (kg/m^2)
  long double ems = 0;           // Erosion of snow mass by maintanence (kg/m^2)

 // MASS TRANSFER RATES
  // Erosion rate by vehicles (Assumed fast removal rate) (kg/m^2-veh)
  long double evrate[3][3] = {{0.18, 0.036, 0},{0.018, 0.0036, 0}};
  long double emrate = 0; // Erosion by maintanences

  long double p_ns;    // New snow density (kg/m^3)
  double pmeltsnow = 0.5; // Assume 50% split in melt
  double pmeltice = 0.5;  // between snow and ice
```

```
// MASS BALANCE CALCULATIONS

  // MELT OR FREEZE OVER TIME INTERVAL ts (kg/m^2)
  // (+) sign indicates melt and (-) sign indicates freezing
  if (metData[j][SURFACE_TEMP] <= MELT_TEMP && Q[QM] < 0 && mo[WATER] > 0)
  {
    // Water freeze to ICE
    melt = ts*mass_transfer(Q[QM], LEF, B);
    pmeltsnow = 0;  // 100% of refreeze goes to ice mass
    pmeltice = 1;
    // Can't freeze more water than is present
    if ((-melt) > mo[WATER]) melt = - mo[WATER];
  }
  else if (metData[j][SURFACE_TEMP] >= MELT_TEMP && Q[QM] > 0)
  {
   if (mo[SNOW] > 0 && mo[ICE] <= 0 )
   {
     // 100% of melt is from SNOW
     melt = ts*mass_transfer(Q[QM], LEF, B);
     pmeltsnow = 1;
   pmeltice = 0;
   // Can't melt more snow than is present
   if (melt*pmeltsnow > mo[SNOW]) melt = mo[SNOW]/pmeltsnow;
     }
    else if (mo[SNOW] <= 0 && mo[ICE] > 0 )
   {
     // 100% of melt is from ICE
     melt = ts*mass_transfer(Q[QM], LEF, B);
     pmeltsnow = 0;
   pmeltice = 1;
   // Can't melt more ice than is present
   if (melt*pmeltice > mo[ICE]) melt = mo[ICE]/pmeltice;
     }
    else if (mo[SNOW] > 0 && mo[ICE] > 0 )
   {
   double msnow, mice;
     // Melt split between ICE and SNOW
     melt = ts*mass_transfer(Q[QM], LEF, B);
     msnow = melt*pmeltsnow;
     mice = melt*pmeltice;
     // Can't melt more snow and ice than is present
     if ( msnow > mo[SNOW]) msnow = mo[SNOW]/pmeltsnow;
     if ( mice > mo[ICE]) mice = mo[ICE]/pmeltice;
     melt = msnow + mice;
     }
  }


  // EVAPORATION MASS LOSS
  if (metData[j][SURFACE_TEMP] > MELT_TEMP && Q[QE] < 0 && mo[WATER] > 0)
  {
   evapmass = ts*mass_transfer(Q[QE], LEV, B);
```

```
 frostmass = 0;
 // Can't evaporate more water than is present on surface
 if (evapmass > mo[WATER]) evapmass = mo[WATER];
}
else if (metData[j][SURFACE_TEMP] < 0 && Q[QE] > 0)
{
 evapmass = 0;
 frostmass = ts*mass_transfer(Q[QE], LEV, B);
}


// PRECIPITATION MASS GAIN (SNOW OR RAIN)
if (metData[j][PC_TYPE] == SNW)
{
 // Density (kg/m^3) of new snow based on air temperature (C)
 // from Gray and Male (1981), eqn (14.1).
   p_ns = 16.018*exp(1.907+0.0835*metData[j][AIR_TEMP]);

   // Accumulated SNOW precipitation
   accumsnow = ts*metData[j][PC_RATE]*(p_ns/360000.00);
}
else if (metData[j][PC_TYPE] == RAIN) // RAIN)
{
 // Accumulated RAIN precipitation
 accumrain = ts*metData[j][PC_RATE]*(1000.00/360000.00);
 }


// VEHICLE EROSION OR COMPACTION
// Snow is compacted (not removed) for FWC < 0.15
// Mass removel is slower for thin layers*density < SNMASS_DIV
if (mo[FWC] >= 0.15 && mo[FWC] < 0.3)
{
 if (mo[SNOW] > SNMASS_DIV) evs = amt*evrate[0][1];
 else          evs = amt*evrate[1][1];
}
if (mo[FWC] >= 0.3)
{
 if (mo[SNOW] > SNMASS_DIV) evs = amt*evrate[0][0];
 else    evs = amt*evrate[1][0];
}

// Vehicle erosion of water
if (mo[WATER] > 0) evw = amt*evrate[0][0];

//if (mo[WATER] >= 0.15 ) evw = amt*evrate[0][0];
//else if (mo[WATER] >= 0.1 && mo[WATER] < .5) evw = 2*amt*evrate[1][0];
//else evw = 0.5*amt*evrate[0][0];
//else evw = 0;


// PLOWING EROSION
```

```
// Left out of the picture at this point.
//emv = emrate*ts;


// CALCULATE MASS OF SNOW, WATER AND ICE
mass[SNOW] = mo[SNOW] + accumsnow - (pmeltsnow*melt + evs + ems)+frostmass;
if (mass[SNOW] < 0) mass[SNOW] = 0;  // NO NEGATIVE MASS ALLOWED

mass[WATER] = mo[WATER] + accumrain + melt + evapmass - evw;
if (mass[WATER] < 0) mass[WATER] = 0; // NO NEGATIVE MASS ALLOWED

mass[ICE] = mo[ICE] - pmeltice*melt;
if (mass[ICE] < 0) mass[ICE] = 0; // NO NEGATIVE MASS ALLOWED


// FREE WATER CONTENT OF SNOW
if (mass[SNOW] > 0)
{
 if (mass[WATER] > 0)
 {
  mass[FWC] = mass[WATER]/(mass[WATER] + mass[SNOW] + mass[ICE]);
  // Max free water holding capacity FWC of snow 30%
  if (mass[FWC] > 0.3) mass[FWC] = 0.3;
 }
 else mass[FWC] = 0;
}
else mass[FWC] = 0;

// Assumed saturation capacity of road surface 1 kg/m^2 (~ 1 mm)
if (mass[WATER] > 1) mass[WATER] = 1;
}
```

```
/*****************************************************************
* EFFECTIVE GRAIN SIZE
*****************************************************************
This function approximates the effective snow radius used by
the albedo routine.

OUTPUT
    rad:       optically equivalent snow grain radius (micrometers)
INPUT
    metData: meteorological data
    j:         row indicator
    mass:      mass of WATER, SNOW, and ICE (kg/m^2)
*****************************************************************/

double eff_grain_rad(const long double metData[][COLUMNS],const int j,
                          const long double Q[], long double mass[],
                          const double radpre)
{
 double rad;

// EFFECTIVE SNOW RADIUS

if (mass[SNOW] > 0 )
{
 if (Q[QM] < 0  || metData[j][SURFACE_TEMP] < MELT_TEMP) //No melting
  {
  rad = radpre;
  if (rad == 0) rad = 50;
  }
 else // (Q[QM] > 0 &&  metData[j][SURFACE_TEMP] >= MELT_TEMP) // Melting
  {
  // New snow <= 15% liquid H20
  if (mass[WATER]/(mass[SNOW]+mass[WATER]) <= 0.15) rad = EFF_RADNS;
  // Aged snow damp %15 < liquid H20 <= 30%
  else if (mass[WATER]/(mass[SNOW]+mass[WATER]) > 0.15 &&
      mass[WATER]/(mass[SNOW]+mass[WATER]) <= 0.3) rad = EFF_RADAS;
  // Old melting snow "slush" > 30%
  else rad = EFF_RADOS;

  // After melting snow rad only drops from new snow fall
  if (rad < radpre && mass[ICE] > 0 && metData[j][PC_RATE] < 0)
  {rad = radpre;}
  }
}
// No snow on road
else rad = 0;
if (mass[SNOW] <= 0 && mass[ICE] <= 1) rad = 0;        // Black ice
if (mass[SNOW] <= 0 && mass[ICE] > 1) rad = 500000; // Thick bubble free ice


return(rad);
}
```

```
/*****************************************************************
* MASS FRACTION ROUTINE
******************************************************************
This function approximates the effective impurity (soot) mass
fraction for the albedo model.  The mass fraction is normalized to
soot.

OUTPUT
     effsoot: effective soot parameter (mass fraction)
INPUT
     metData: meteorological data
     j:                      row indicator
     mass:      mass of WATER, SNOW, and ICE (kg/m^2)
*****************************************************************/

long double mass_fraction(const long double metData[][COLUMNS],
                          const double j, const long double mo[],
                          long double mass[])
{
 // lane average minute pass rate amp

 double massdist = 0.2834/2; // Mass distribution on road (kg/m^2)
                             // per lane and pass of plow truck
 long double soot;                  // Effective soot
 double amp = AHP/60;               // Average minute pass rate per lane


// EFFECTIVE SOOT MASS FRACTION

// SAND REMOVEL FROM PLOWING AND VEHICLES HAVE NOT BEEN
// INCLUDED

if (mo[SNOW] > 0 || mo[ICE] > 0)
{
 // Sanding snow and ice
 if (mo[FWC] <= 0.2) mass[SAND] = massdist*amp + mo[SAND];
 // No sanding over time period
 else mass[SAND] = mo[SAND];
 mass[SMF] = mass[SAND]/(mo[WATER]+mo[SNOW]+mo[ICE]+mass[SAND]);
}
else
{
 mass[SAND] = 0;
 mass[SMF] = 0;
}

// Normalize sand mass fraction SMF into an effective soot fraction
soot = mass[SMF]/NF;

return(soot);
}
```

```
/*****************************************************************
* TRAFFIC VOLUME
******************************************************************
This function approximates the diurnal Average Period Traffic APT
based on a polynomial fucntion.

OUTPUT
     amt:            Average minute traffic (vehicle/minute)
INPUT
     mintime:        Row indicator used to represent minute of day
*****************************************************************/
#include <math.h>

long double trafficvolume(const double mintime)
{
 long double a = 0.0001155;
 long double b = 0.006333;
 long double c = 0.101649;
 long double d = 0.400591;
 long double e = 0.482495;
 double amt;
 double t;

 t = mintime/60;

 amt = (a*pow(t,4) - b*pow(t,3) + c*pow(t,2) - d*t + e)/15;

return(amt);
}
```

```
/*****************************************************
* GROUND TEMPERATURE ROUTINE
******************************************************
* This procedure calculates the ground temperature profile
******************************************************/
void ground_temp(long double surfaceTemp, long double tt_pre[],
                 long double ts, int loops, long double tg,
                 long double T[], int *size_tt)
{
  int i, j;
  long double h2 = 0.0001; // THIS IS H^2
  long double a[101];
  long double t_prev[101];

  for(i=1; i<50; i++)  // 1 -> 49 = 0.00000025
    a[i] = 0.00000025; // 2.5 * 10 ^ -7

  for(i=50; i<90; i++)  // 50 -> 89 = 0.000000426
    a[i] = 0.000000426; // 4.26 * 10 ^ -7

  for(i=90; i<100; i++)  // 90 -> 99 = 0.000000536
    a[i] = 0.000000536; // 5.36 * 10 ^ -7

  t_prev[0] = tg;
  t_prev[100] = surfaceTemp;
  T[0] = tg;
  T[100] = surfaceTemp;

  for(i=1; i<100; i++)
    t_prev[i] = tt_pre[i];

  for(j=0; j<loops; j++)
  {
    for(i=1; i<100; i++)
    {
      T[i] = (t_prev[i] + ((ts*a[i])/h2) * ((t_prev[i+1]) -
                    (2*t_prev[i]) + (t_prev[i-1])));
    }
     for(i=1; i<100; i++)
     t_prev[i] = T[i];
  }
  *size_tt = 101;
}
```

```
/*******************************************************************************
* INTERPOLATE DATA
********************************************************************************
* This procedure linearly interperlates to every minute  between data points on a 15 min interval.
*******************************************************************************/

void interperlate_data(const long double in_data[][COLUMNS],
                       long double out_data[][COLUMNS],
                       int in_rows,  int * out_rows)
{
 int i=0, j=0, k=0, count=0;
 long double slope;

    for(i=1; i<in_rows; i++)
    {
     for(k=0; k<COLUMNS; k++)
     {

       if (k == 4 || k == 5)
        {
         for(j=0; j<STEP; j++)
          {
           out_data[count][k] = in_data[i-1][k];
           count++;
          }
          count = count-15;
        }
        else
        //if (k!=4)
        {
          slope = (in_data[i][k] - in_data[i-1][k])/STEP;

          for(j=0; j<STEP; j++)
          {
            out_data[count][k] = j*slope + in_data[i-1][k];
            count++;
          }
          count = count-15;
        }

     }
    count = count+15;
    }
    *out_rows = count;
}
```

```
/*****************************************************
* PROCEDURES TO READ AND WRITE TO FILES
*****************************************************/
#include <stdio.h>

void print_1darray(long double array[], int size)
{
  int i;

  for(i=0; i<size; i++)
    printf("%d\t%f\n", i, array[i]);
}

/*****************************************************/
void print_array(long double array[][COLUMNS],int rows)
{
  int i;

  for(i=0; i<rows; i++)
    printf("%d row: %1.1f %1.1f %1.1f %1.1f %1.1f %1.1f %1.1f %
       1.1f %1.1f %1.1f %1.1f %1.1f\n", i, array[i][0], array[i][1],
       array[i][2], array[i][3], array[i][4], array[i][5], array[i][6],
       array[i][7], array[i][8], array[i][9], array[i][10], array[i][11]);
}

/*****************************************************/
void print_file_data(char * file_name, long double array[][COLUMNS], int rows)
{
  FILE * fileptr;
  int i;

  fileptr = fopen(file_name, "w");

  fprintf(fileptr, "This file contains the interpertated data used in the
              calculation of Albedo\n\n");
  fprintf(fileptr, "Air Temp\tRH\t\tWind dir\tWindspeed\tpre type\tpre rate\
              tsfc temp\tsub temp\tsolar     rad0\tsolar rad1\tcloud cover
              \tpreasure\n");

  for(i=0; i<rows; i++)
  fprintf(fileptr, "%f\t%f\t%f\t%f\t%f\t%f\t%f\t%f\t%f\t%f\t%f\t%f\n",
         array[i][0], array[i][1], array[i][2],    array[i][3], array[i][4], array[i][5],
         array[i][6], array[i][7], array[i][8], array[i][9], array[i][10], array[i][11]);

  fclose(fileptr); // CLOSE FILE
}

/*****************************************************/
void print1dfile(char * file_name, long double array[], int length)
{
  FILE * fileptr;
  int i;
```

```
  fileptr = fopen(file_name, "w");

  for(i=0; i<length; i++)
    fprintf(fileptr, "%.10f\n", array[i]);

  fclose(fileptr);
}

/****************************************************/
void initialize_tt_pre(long double tt_pre[], long double tg)
{
  int i;

  tt_pre[0] = tg;

  for(i=1; i<TT_SIZE; i++)
    tt_pre[i] = 0.0;
}

/****************************************************/
int get_file_data(char * file_name, long double array[ROWS][COLUMNS],
                  int * rows, int * days)
{
  FILE * fileptr;
  int month=0, day=0, year=0, i=0, j=0;
  char garbage;
  char * weather= "none";

  fileptr = fopen(file_name, "r");

  if(fileptr != NULL)
  {
    fscanf(fileptr, "%d%c%d%c%d\n", &month, &garbage, &day, &garbage, &year);

    for(i=1; i<month; i++)
    {
      if((i == 1) || (i == 3) || (i == 5) || (i == 7) || (i == 8) || (i == 10))
        day += 31;
      else if((i == 2) && (year % 4 != 0))
        day += 28;
      else if (i == 2)
        day += 29;
      else
        day += 30;
    }
    i = 0;

    while((fscanf(fileptr,"%lf %lf %lf %lf %s %lf %lf %lf %lf
    %lf %lf %lf\n",&array[i][0],&array[i][1],&array[i][2],
    &array[i][3],weather,&array[i][5],&array[i][6],&array[i][7],&array[i][8],&array[i][9],
    &array[i][10],
```

```
    &array[i][11]) != EOF) && (i <= ROWS))
    {

    // CONVERT STRING "snow, rain or none"  TO A NUMBER VALUE
      if(strcmp(weather, "snow") == 0) array[i][4] = 2.0;
      else if(strcmp(weather, "rain") == 0) array[i][4] = 1.0;
      else array[i][4] = 0.0;

      i++;
    }
    *days = day;
    *rows = i;
  }
  else
  return(FALSE);
  fclose(fileptr); // CLOSE FILE

  return(TRUE);
}
```

```
/*******************************************************
* ADDITIONAL FUNCTIONS
*******************************************************/

/*******************************************************
 * long double adj_atm_pressure(const long double Po)
 *
 * returns long double: Atmospheric pressure a distance y above
 *            1455.42 m (Boze hill, elev. ~1524 m) in (mmbar)
 *
 * Parameters:
 * const long double Po: Reference Pressure (Bozeman Farm,
 *                  elev. 1455.42 m) in (mmbar)
 *
 * This function calculates the approximate atmospheric
 * pressure at Bozeman Hill from data recorded at Bozeman
 * Farm in the Gallatin valley.
 *
 * Assumes: Constant Atmospheric Temperature
 *       Cylindrical column of dry air
 *       Elev. gain 68.58 m.
 ******************************************************/

long double adj_atm_pressure(const long double Po)
 {
  long double y = 68.58;        // Elevation gain (m)
  long double m = 28.97;        // Molar mass of dry air (kg/kmol)
  long double g = 9.80;         // Boltzman molecular gas constant (J/molecule*K)

  //long double k = 1.38*10^-23;        // Acceleration of gravity (m/s^2)
  //long double Na = 6.022*10^26;       // Avagadros number (molecules/kmol)
  //long double T = 273.0;          // Avg Atmospheric Temperature (K)

  long double bottom = 2268728.28; // THIS IS (k*Na*T)

  // return atmospheric preasure
  return( (Po)*exp(-(m*g*y)/(bottom)));
 }

/*******************************************************
 * long double mass_transfer(Qm, Le, B)
 *
 * returns mass transfer rate (kg/m^2*sec)
 *
 * Parameter:
 * Qm: Net heat flux at surface (W/m^2)
 * Le:  Latent heat of transformation
 *  b : Thermal quality of medium, The fraction of ice
 *  in a unit mass of wet snow, for slush b = 0.5
 *  to 0.85, for water b = 1.
 *
 * This function calculates a mass phase change rate (kg/m2-sec)
```

```
*******************************************************/

long double mass_transfer(const long double Qm, const long double Le,
                          double b)
{
return(Qm/(Le*b*1000));
}


/*******************************************************
 * long double air_density(const long double Pa, const long double T)
 *
 * returns: Air density (kg/m^3)
 *
 * Parameters:
 * const long double Pa: Atmospheric pressure (mm bar)
 * const long double T: Air temperature (C)
 *
 * This function calculates air density from the ideal gas
 * law based on air temperature and atmospheric pressure.
 *
 *******************************************************/

long double air_density(const long double Pa, const long double T)
{
  long double R = 0.287; // Gas constant of air (kJ/kg-K)

  return( (Pa/10.0) / (R * (T + 273.15)) );
}


/*******************************************************
* long double vapor_preasure(Le, T, To, Po, Pv)
*
* returns:  Saturation Vapor Pressure (kPa)
*
* Parameters:
* long double Le:     Latent heat of transformation (kJ/kg)
* long double T:      Temperature of Interest (C)
* long double To:     Reference Temperature (C)
* long double Po:     Reference Pressure (kPa)
*
* This function calculates the water vapor pressure in kPa
* using the  Clausis-Clapeyron equation.
* Assumed: Air is an Ideal Gas
* and for small temperature changes Le is ~ constant
*******************************************************/

long double vapor_pressure(const long double Le, const long double T,
                         const long double To, const long double Po)
{
  long double R = 0.462;        // GAS CONSTANT FOR WATER (kJ/kg*K)
```

```
  // CONVERT THE TEMPERATURE TO KELVINS

  long double To_k = To + 273.15;
  long double T_k = T + 273.15;

  return(Po*exp((Le/R)*(1/To_k - 1/T_k)));
}


/**********************************************************
 * This function estimates surface temperature on a surface
 * using heat capacity of the surface.
 *
 * returns: estimated surface temperature (C)
 *
 * parameters:
 * const long double Q: energy budget or deficit at the surface (W/m^2)
 * const long double T_pre: previous surface temperature (C)
 * const long double ts: time step in seconds
 *
 **********************************************************/


long double est_surf_temp(const long double Qm, const long double T_pre,
                          const long double ts, const long double mass[])
{
  long double pbituminous = 2203.0; // Density of bitumen (kg/m^3)
  long double Db = 0.000000536;          // Thermal diffusivity of bitumen (m^2/s)
  long double Cp_b = 881.2;   // Heat capacity of bitumen (J/kg-k)
  long double Tnew;              // New temperature (C)

     if (T_pre <= MELT_TEMP && Qm < 0 && mass[WATER] > 0)
     {
     Tnew = MELT_TEMP;// Change of phase (freezing) equal. temperature
     }
    else if (T_pre >= MELT_TEMP && Qm > 0 && mass[SNOW] > 0)
     {
     Tnew = MELT_TEMP;// Change of phase (melting) equal temperature
  }
  else if (T_pre >= MELT_TEMP && Qm > 0  && mass[ICE] > 0)
     {
     Tnew = MELT_TEMP;// Change of phase (melting) equal temperature
  }
  else
  {
   Tnew = (Qm*ts)/(H*pbituminous*Cp_b) + T_pre;
  }
 return(Tnew);
}

/**********************************************************
```

```
* Initialize_tt
*
* This function initializes the ground temperature profile
**********************************************************/

void initialize_tt(long double ts,long double tg, long double Ttd[])
{
    int i;
    long double step = (ts-tg)/TT_SIZE;

    for(i=0; i<TT_SIZE; i++)
    {
     Ttd[i] = tg + step*i;
    }
}
```

/***

COMPUTATION ALBEDO ROUTINE (CAR)

This routine calculates the visiable, near infrared and solar albedos. This work is basically the result of earlier work by Susan Marshall. This is a result of her Ph.D. thesis "A Physical Parameterization of Snow Albedo for Use in Climate Models", university of Colorado, 1989.

************************** DEFINE VARIABLES **********************************

iwvl	Defines wavelength separation of visible and NIR = 0 split at 0.7 micrometers = 1 split at 0.9 micrometers
cosz	solar zenith angle cosine
ps	surface air pressure (millibars)
rad	snow grain radius (micrometers)
snowmass	mass per unit area (g/cm^2)
soot	soot content of snow (mass fraction)
surfalb(i)	albedo of pavement surface i = 0 visible i = 1 NIR
dfrac(i)	diffuse fraction of surface downflux i = 0 visible i = 1 NIR
sflx(i)	fraction of surface downflux in each spectral ban (needed only to return value of broadband solar snow albedo) i = 0 visible i = 1 NIR
trans(i)	atmospheric transmittance (fraction) If value < 0, solar transmittance defaults to value of 0.55 and the others will be estimated in the program. i = 0 visible i = 1 NIR 1 = 2 solar (default = 0.55)
alb(i)	snow albedo i = 0 visible i = 1 NIR i = 2 solar

************************* REFERENCES *****************************

Marshall, s. 1989. A new snow albedo parameterization for use in climate models. Ph. D. thesis. University of Colorado

Marshall, S.E. and S.G. Warren 1987. Parameterization of Snow Albedo for Climate Models in Large Scale Effects of Seasonal Snow Cover (Proceedings of the IUGG/IAHS Symposium. August, 1987). IAHS Publ. no. 166 pp43-50

Wiscombe, W.J. and S.G. Warren 1980. A model for the spectral albedo of snow. I.Pure snow. J. Atmos. Sci. 37. 2712-2733

Rozenberg, G.V. 1966. Twilight: A Study in Atmospheric Optics. Plenum Press. (translated from the Russian). 358pp.

Wallace, J.M. and P.V. Hobbs 1977. Atmospheric Science: An Introductory Survey. Academic Press.

```
*******************************************************************/

#include <math.h>
#include <stdlib.h>
#include <stdio.h>

// PROTOTYPE FUNCTIONS //
double alb5(int i,double as,double it);
double transmt(double solat, int i,int j);
double albclr(int i,int j,double rad,long double soot);
double aintrp(int i,int j,double amax,double rad, long double soot,
                        long double snowd,double srfalb);
double efsoot(int i,int j, long double soot, long double snowd,
                        double srflab);
double efrad(int i, int j, double rad, double czen);
double albcld(int i,double aclr,double at,long double soot);
double difrac(int j,int i,double sigma,double ram,
                        double atrns,double czen);

// PROCEDURE //
int Albedo(   int iwvl,double cosz,long double ps, double rad,
                        long double snowmass,long double soot, double srfalb[2],
                        double dfrac[2],double sflx[2], double trans[3],
                        double alb[3])

{
/************************* DECLARATIONS ************************/


// DEFINE FLOATING POINT VARIABLES //
double       relairmass,sigma,solat,difmu,dfrc,
             mu,erad,ua,esoot,clear,alb3,albmax;
```

```
double po = 1013.0;            // Reference sea-level pressure (mbar)
double solcon = 1372.0;        // solar constant (w/m^2)

// DEFINE INTEGER VARIABLES //
int i;

// DEFINE ARRAYS //
double fluxes[2][2] = {{0.46,0.54},{0.63,0.37}};


/*********************** START CALCULATIONS *********************/

// Relative air mass (relairmass) - ref (Rozenberg, 1966)
    // Relative air mass is also called the "optical path length" or
    // the "optical path".

    relairmass = 1.0/(cosz + 0.025*exp(-11.0*cosz));

    // 1/cosz is sometimes used for the relative air mass.

    // Max allowable value = 10.0.
    if(relairmass >= 10.0) relairmass = 10.0;

// Solar Atmospheric transmittance (SOLAT) - ref
// (Wallace and Hobbs, 1977)
    // Default, trans[2] = 0.55
    if (trans[2] <= 0.0) trans[2] = 0.55;
    solat = trans[2];

// Surface to sea level pressure ratio
    // sigma is the ratio of surface air pressure to the
    // pressure at sea level.
    sigma = ps/po;
    if(sigma >= 1.0) sigma = 1.0;  // Must be above see level.


// Atmospheric transmittance for visible (i = 0) & NIR (i = 1)
    // If value of trans, sflx, or dfrac are set < 0, they will be
    // estimated via the functions trnsmt and diffrac or defaulted
    // to fluxes.
    // sflx is used to calculate a value for the solar snow albedo.
    // dffrac is used to obtain a value of effective zenith cosine.

    for(i=0;i<=1;i++) {
            // Estimate transmittance for visible (i=0) and NIR (i=1).
            // If it is not initally known and supplied as input, use
            // the function trnsmt(solat,i,iwvl).

            if(trans[i] <= 0.0) trans[i] = transmt(solat,i,iwvl);

            // Estimate surface downflux for visible (i=0) and
            // NIR (i=1). If it is not initally known and supplied as
```

```
// input, use the matrix fluxes[i][j].

if(sflx[i] <= 0.0) sflx[i] = fluxes[iwvl][i];

// Estimate diffuse fraction. This is the fraction of the
// incoming radiation at the snow surface that is diffuse
// rather than direct from solar radiation.

if (dfrac[i] <= 0.0)          // not known, estimate
        dfrc = difrac(iwvl,i,sigma,relairmass,trans[i],cosz);
else
        dfrc = dfrac[i];


// The zenith cosine is weighted for diffuse and direct
// fraction, mu. The effective zenith cosine for diffuse
// radiation is cosz = 0.65.

difmu = 0.65;
mu = dfrc*difmu + (1.0-dfrc)*cosz;

if(mu >= 1.0) mu = 1.0;    // mu must lie between 0.0 and 1.0
if(mu <= 0.0) mu = 0.0;

// Estimate effective snow grain radius.
// Check to see if snow on road
if(rad > 0.0) erad = efrad(iwvl,i,rad,mu);


// Estimate deep snowcover albedo (albmax)
ua = srfalb[i];
albmax = albclr(iwvl,i,erad,soot);
//printf("\n albmax = %f\n", albmax);  /* test */

if(snowmass <= 0.0 && rad <= 0.0)
        // Dry road
        alb[i] = ua;
else if(snowmass > 0.0 && rad <= 0.0)
        // Wet road albedo ~58% of dry road
        alb[i] = 0.58*ua;
else
        {
        // Check for special case where srfalb > albmax.
        if(albmax <= ua)
                {
                //printf("surface albedo > albmax\n");  /* test */

                // surface albedo is greater than snow albmax
                alb[i] = aintrp(iwvl,i,albmax,erad,soot,snowmass,ua);
                }
        else
                {
```

```
                    //printf("surface albedo < albmax\n");  /* test */

                    // snow albmax is greater than surface albedo.
                    esoot = efsoot(iwvl,i,soot,snowmass,ua);

                    // Calculate albed for effective soot and effective
                    // radius.
                    alb[i] = albclr(iwvl,i,erad,esoot);
                    }

            // Correct for NIR snow albedo for:
            //      (a) cloudy sky
            //      (b) extend albedo to full range => 5 micrometers.
            if(i==1)
                    {
                    // cloudy day
                    clear = alb[i];
                    //printf("clear = %f\n", clear); /* test */

                    alb[i] = albcld(iwvl,clear,trans[i],esoot);
                    //printf("alb[1] = %f\n", alb[i]); /* test */

                    // extend to 5 micormeters
                    alb3 = alb[i];
                    alb[i] = alb5(iwvl,alb3,trans[i]);
                    }
            }
        // PRINT TO SCREEN  /* test */
        //printf("%i %f %f %f\n\n",i,erad,alb[i],trans[i]);
        }

    // Calculate snow solar albedo
    alb[2] = (sflx[0]*alb[0] + sflx[1]*alb[1])/(sflx[0] + sflx[1]);

    return 0;
    }       // End albedo program

/*************************************************************/

double difrac(int j,int i,double sigma,double ram,double atrns,
                        double czen)

/*************************************************************/

// This function estimates the fraction of diffuse radiation,
// given values sigma. Correction facotrs for relative airmass,
// atmospheric transmittance and zenith cosine are included.

// INPUT VARIABLES
//   i = iwvl, wavelength sepaparation parmaneter.
//   j = visible/NIR identification parameter.
//   sigma = The ratio of surface air pressure to the pressure
```

```
//                       at sea level.
//   ram = Relative air mass is also called the "optical path
//               length" or the "optical path".
//   atrns = atmospheric transmittance, "trans[i]"
//   czen = Zenith cosine

    {

    double dclr, slope, tclr,diffrac;              /** 0.0486 **/
    double at[2][2] = {{0.0540,-0.2567},{0.0400,-0.3957}};
    double bt[2][2] = {{-0.4000,0.3061},{-0.8000,0.2383}};
    double c[2][2] = {{0.4460,0.0630},{0.3450,0.2500}};
    double k[2][2] = {{-0.3888,-0.1686},{-0.4135,-0.0042}};
    double asl[2][2] = {{-0.3389,-0.2971},{-0.3417,-0.2479}};
    double bsl[2][2] = {{0.4689,0.2943},{0.4588,0.1895}};

    // tclr is the clear sky transmission. Calculate this.
    if(i==0)           // visible spectrum
            tclr = 1.0 - (at[j][i]*ram)*exp(bt[j][i]*(1.0-sigma));
    else                         // NIR spectrum
            tclr = exp((at[j][i]*pow(ram,bt[j][i]))*sigma);

    // tclr must lie between atrans and 1.0.
    if(tclr >=1.0) tclr = 1.0;
    if(tclr <= atrns) tclr = atrns;

    // Calculate clear sky diffuse fraction dclr.
    dclr = c[j][i]*(1.0 - exp(k[j][i]*ram*sigma));
    // dclr must lie between 0.0 and 1.0.
    if(dclr >= 1.0)     dclr = 1.0;
    if(dclr <= 0.0) dclr = 0.0;

    // Zenith cosine (czen).
    slope = asl[j][i] + bsl[j][i]*czen;

    // Calculate diffuse fraction (difrac).
    diffrac = (atrns - tclr)*slope + dclr;
    // difrac must lie between dclr and 1.0.
    if(diffrac >= 1.0)  diffrac = 1.0;
    if(diffrac <= dclr) diffrac = dclr;

    return diffrac;
    }

/**************************************************************/

double albcld(int.i,double aclr,double at,long double soot)

/**************************************************************/

// This function estimates the change in NIR snow albedo
// under overcast skies. This usually results with an increase in
```

```
// albedo due to shifts in the spectrum of the incoming radiation.
// - ref (Marshall and Warren, 1987)

// INPUT VARIABLES
//    at = atmospheric transmittance.
//    soot = effective soot content.
//    aclr = albedo under clear skies.

    {

    double a[2] = {0.3865,0.1952};
    double b[2] = {0.0640,0.0384};
    double c[2] = {0.0017,0.0011};
    double to[2] = {0.740,0.640};

    double sl,beta,albedocld;

    if(soot <= 1.0e-9) soot = 1.0e-9;
    sl = log(soot);
    beta = a[i] + b[i]*sl + c[i]*(sl*sl);
    albedocld = (at-to[i])*beta + aclr;

    // The albedo on a cloudy day must lie between 1.0
    // and the value on a clear day. ???????????

    if(albedocld >= 1.0) albedocld = 1.0;
    if(albedocld <= aclr) albedocld = aclr;

    return albedocld;
    }

/*****************************************************************/

double efrad(int j, int i, double rad, double czen)

/*****************************************************************/

// This function estimates the effective radius, "efrad" of the snow
// given a value of the actual mean grain radius, "rad" and the
// zenith cosine angle, "czen". This procedure simplifies the
// problem by combining the effects of radius and zenith
// cosine. Both effects are similar therefore they are combined.

// INPUT VARIABLES
//    i = iwvl, wavelength separation parameter.
//    j = visible/NIR identification parameter
//    rad = mean grain radius
//    czen = Zenith cozine

    {
    double slope, delmu, sqrad, ratio,efradius;
    double  b[2][2] = {{1.2812,1.2642}, {1.3072,1.2039}};
```

```
    slope = b[i][j];
    delmu = czen - 0.65;
    sqrad = sqrt(rad);
    ratio = sqrad/slope;
    efradius = pow((sqrad + delmu*ratio), 2);

    return efradius;
    }

/*****************************************************************/

double efsoot(int i,int j, long double soot, long double snwmass, double srfalb)

/*****************************************************************/

// This function estimates the effective soot given values of
// soot concentration "soot", snowmass "snwmass", and pavement
// surface albedo "srfalb".

// INPUT VARIABLES
//    i = iwvl, wavelength separation parameter.
//    j = visible/NIR identification parameter
//    soot = soot concentration (mass fraction)
//    snwmass = snow mass per unit area
//    srfalb = pavement surface albedo

    {
    double a,b,seffo, effecsoot;
    double  ao[2][2] = {{-13.6421,-13.7878}, {-13.7781,-13.6237}};
    double   a1[2][2] = {{-2.3306,-2.7360}, {-1.8936,-1.8347}};
    double  bo[2][2] = {{-1.2430,-1.3433}, {-1.2855,-1.3044}};
    double  b1[2][2] = {{0.5714,0.9005}, {0.6730,1.3470}};
    double  b2[2][2] = {{-0.4319,-1.5425}, {-0.5038,-2.1925}};

    // Calculate the effective soot as a function of soot content
    // and snow depth.

    a = ao[i][j] + a1[i][j]*srfalb;
    b = bo[i][j] + (b1[i][j]*srfalb) + (b2[i][j]*srfalb*srfalb);
    seffo = exp(a)*pow(snwmass,b);
    if(seffo >= 1.0) seffo = 1.0;
    effecsoot = soot + seffo;
    if(effecsoot <= 1.0e-9) effecsoot = 0.0;

    return effecsoot;
    }

/*******************************************************************/

double aintrp(int i,int j,double amax,double rad, long double soot,
        long double snwmass,double srfalb)
```

```
/**********************************************************************/

// This function interpolates the snow albedo as a function of soot
// content when the pavement surface albedo is higher than the snow
// surface albedo. We also include the case where dirty snow overlies
// clean snow.

// INPUT VARIABLES
//    i = iwvl, wavelength separation parameter.
//    j = visible/NIR identification parameter
//    amax = deep snow cover albedo
//    rad = effective grain radius
//    soot = soot concentration (mass fraction)
//    snwmass = snowmass per unit area
//    srfalb = road surface albedo

    {
    long double  ar,rtox,brs,negp,tmin,tmax, slope,diff,tmin10,
                      tmax10,aintrpp,t[2];
    double  a[2][2][2] = {{{0.1983, 2.640},{5.0e-5, 3.2e-5}},
                                              {{1.5e-2, 1.300},{4.0e-5, 5.0e-4}}};
    double   b[2][2][2] = {{{2.67e9,8.67e8},{0.0,0.0}},
                                              {{2.60e7,2.00e8},{0.0,0.0}}};
    double   x[2][2][2] = {{{1.50,1.40},{0.640,-1.00}},
                                              {{1.20,1.40},{0.640,0.0}}};
    double p = 0.50;

    int k;
    negp = -p;

    for(k = 0;k<=1;k++)
            {
            ar = a[i][j][k]*rad; //printf("a=%f ",a[i][j][k]);
            brs = b[i][j][k]*rad*soot; //printf("brs=%f ",b[i][j][k]);
            rtox = pow(rad,x[i][j][k]); //printf("x=%f \n",x[i][j][k]);

            //printf("ar=%f; brs=%f; rtox=%f\n",ar,brs,rtox); /* test */
            t[k] = ar*pow((brs + rtox),negp);
            }
    tmin = t[0];
    tmax = t[1];
    printf(""); // needed to make model run for thin snow layers
    //printf("tmin = %f; tmax = %f; i = %i\n",tmin,tmax,j);  /* test */ //

    if(snwmass <= tmin)
            {
            //printf("snwmass <= tmin\n");  /* test */
            aintrpp = srfalb;
            }
    else if(snwmass >= tmax)
            {
```

```
            //printf("snwmass >= tmax\n"); /* test */
            aintrpp = amax;
            }
    else
            {
            // Now interpolate
            //printf("snwmass <= tmax\n"); /* test */
            tmin10 = log10(tmin);
            tmax10 = log10(tmax);
            //printf("tmin10=%f; tmax10=%f \n",tmin10, tmax10); /* test */
            //printf("amax=%f; srfalb=%f \n", amax, srfalb);
            slope = (amax - srfalb)/(tmax10 - tmin10);
            diff = log10(snwmass) - tmin10; //log10(tmin);
            //printf("slope=%f; diff=%f \n",slope, diff); /* test */

            aintrpp = slope*diff + srfalb;
            }

    //printf("aintrpp=%f\n", aintrpp); /* test */
    return aintrpp;

    }

/*****************************************************************/

double albclr(int i,int j,double rad,long double soot)

/*****************************************************************/

// This function calculates clear sky surface albedo.

// INPUT VARIABLES
//    i = iwvl, wavelength separation parameter.
//    j = visible/NIR identification parameter
//    rad = effective grain radius.
//    soot = effective soot content.

    {
    double  al,ah,a2,s2,s21,ratio,k,sqrl,sqrad,albedoclr;
    double  l[2][2] = {{0.0700,0.0590}, {0.0710,0.0490}};
    double  c[2][2] = {{0.9988,1.0667}, {0.9952,0.9832}};
    double  d[2][2] = {{-0.0020,-0.1811}, {-0.0034,-0.2161}};
    double  a[2][2] = {{-6.3550,-5.9328}, {-6.3914,-6.0302}};
    double  b[2][2] = {{-1.9752,-1.8102}, {-1.9194,-1.5541}};
    double  kl[2][2] = {{0.4540,0.5670}, {0.4690,0.6320}};
    double  kh1[2][2] = {{0.4500,0.5800}, {0.4500,0.8000}};
    double  kh2[2][2] = {{-0.0400,-0.0400}, {-0.0400,-0.1200}};

    sqrad = sqrt(rad);
    sqrl = log(sqrad);
    al = l[i][j];
```

```
    // Visible spectrum for ah (j = 0).

    if(j == 0)
    ah = c[i][j] + d[i][j]*sqrad;

    // NIR spectrum for ah (j = 1).

    if(j == 1) ah = c[i][j], + d[i][j]*sqrl;

    s21 = a[i][j] + b[i][j]*sqrl;
    s2 = exp(s21);
    a2 = (al + ah)/2.0;
    if(soot >= s2)
            {
            k = kl[i][j];
            ratio = log(soot) - s21;
            albedoclr = al + (a2 - al)*exp(-k*ratio);
            if (albedoclr <= al) albedoclr = al;
            }
    else
            {
            if(soot <= 1.0e-9) soot = 1.0e-9;
            ratio = s21-log(soot);
            albedoclr = ah - (ah - a2)*exp(-kh1[i][j]*ratio
                                    + kh2[i][j]*ratio*ratio);
            if(albedoclr >= ah) albedoclr = ah;
            }
    return albedoclr;
    }

/*****************************************************************/

double transmt(double solat, int i,int j)

/*****************************************************************/

// This function estimates the visible or NIR atmospheric
// transmittance given a value of of the solar atmospheric
// transmittance

// INPUT VARIABLES
//    solat = solar atmospheric transmittance
//    i = 0 for visible, =1 for NIR.
//    j = iwvl = separation factor between visible and NIR. **/

    {

    double transmttnce;

    double  a[2][2] = {{1.5710,0.4246},{1.5064,0.0579}};
    double  b[2][2] = {{-0.5715,0.5751},{-0.5060,0.9412}};
```

```
    // a[i][j] and b[i][j] are both empirical matrices for calculating
    // transmittance of the atmosphere if it is not initially known.

    transmttnce = a[j][i]*solat + b[j][i]*solat*solat;
    return transmttnce;
    }

/******************************************************************/

double alb5(int i,double as,double at)

/******************************************************************/

// This function corrects albedo to full solar range (>= 5 micrometers).

// INPUT VARIABLES
//    i = wavelength separation parameter
//    as = albedo (either visible or NIR)
//    at = atmospheric transmittance (either visible or NIR)

    {
    double frac5, albedo5;

    double  a[2] = {0.0016,-0.0020};
    double  b[2] = {-0.0158,0.0141};
    double   c[2] = {0.0462,0.0372};

    double   albo = 0.015;

    frac5 = a[i] + b[i]*at + c[i]*at*at;
    if(i == 0 & frac5 <= 0.17) frac5 = 0.0;
    if(frac5 <= 0.0) frac5 = 0.0;
    albedo5 = (1.0 - frac5)*as + frac5*albo;
    return albedo5;
    }

/******************************************************************/
/** End of file to calculate albedo of snow **/
/******************************************************************/
```

```
/*****************************************************************
 * GLOBAL VARIABLES  FOR ALL .C FILES
 *****************************************************************/
#define COLUMNS 12
#define STEP 15

#define TRUE 1                // Boolean Constants
#define FALSE 0
#define ROWS 97               // Number of rows in original data
#define MAXROWS 1440          // Number of rows after interpertating orig. data
#define TT_SIZE 101           // Length of the tt_pre array
#define PIE 3.141592654       // Value of Pie

// EFFECTIVE SNOW GRAIN RADIUS IN MODEL
#define EFF_RADNS 50          // Effective snow grain radius new snow
#define EFF_RADAS 100         // Effective snow grain radius new snow
#define EFF_RADOS 1000        // Effective snow grain radius new snow

#define NONE  0               // Precipitation type
#define RAIN  1               // Precipitation type
#define SNW   2               // Precipitation type

// COLUMN LOCATION OF DATA IN DATA MATRICES
#define AIR_TEMP  0           // Air temperature
#define RH        1           // Relitive humidity
#define WIND_DIR  2           // Wind direction
#define WIND_SPD  3           // Wind Speed
#define PC_TYPE    4          // Precipitation Type
#define PC_RATE   5           // Precipitation Rate
#define SURFACE_TEMP 6        // Surface temperature
#define SUBSF_TEMP    7       // Subsurface temperaure
#define SOLAR       8         // Incoming solar radiation
#define IR          9         // Incoming Infrared Radiation
#define N           10        // Cloud cover fraction
#define P_ATM       11        // atmospheric pressure

#define WATER       0         // Column location in mass array
#define SNOW        1         // Column location in mass array
#define ICE         2         // Column location in mass array
#define FWC         3         // Column location in mass array
#define SAND        4         // Column location in mass array
#define SMF         5         // Column location in mass array

#define VIS  0                // Column location in albedo array
#define NIR  1                // Column location in albedo array
#define ALLWAVE 2             // Column location in albedo array

#define QM    0               // Energy budget at the surface for heat flux array
#define QLW   1               // Longwave radiation heat flux for heat flux array
#define QSW   2               // Shortwave radiation heat flux for heat flux array
#define QH    3               // Sensible heat flux for heat flux array
#define QE    4               // Latent heat flux for heat flux array
```

```
#define QG     5            // Ground heat flux for heat flux array
#define QP     6            // Precipitation heat flux for heat flux array
#define QA     7            // Heat flux for vehicles for heat flux array
#define QL_IN  8            // Longwave radiation incoming for heat flux array
#define QL_OUT 9            // Longwave radiation outgoing for heat flux array

// OTHER DEFINITIONS
#define NF    1500          // Normalization factor
#define AHP   1.96          // Average houly pass rate of maint. veh. when snow present
#define FPP   0.928         // Fraction plowed per pass of maint. veh.
#define FSP   0.357         // Fraction sanded per pass of maint. veh.

#define E    0.93           // Approx. emissivity of the surface (snow + blacktop)
#define S_B  0.000000056696 // Steffan-Bolzmann constant (W/m^2*k^4)
#define KH   0.0023         // Dimensionless transfer coeff. for heat
#define KE   0.0023         // Dimensionless transfer coeff. for water vapor
#define LEV  2500.5`        // Latent heat of vaporization at 0.1 C (kJ/kg)
#define LES  2834.8         // Latent heat of sublimation at 0C (kJ/kg)
#define LEF  333.5          // Latent heat of fusion (kJ/kg)
#define KG   1.34           // Thermal Conductivity of asphalt (bituminous) (W/m*k)
#define H    0.01           // Nodal distance for ground temperature profile (m)
#define PW   1000.0         // Density of water (kg/m^3)
#define CPW  4205.0         // Heat capacity of water (J/kg*k)
#define MELT_TEMP 0         // Equilibriam temp. of snow and water (C)
#define B    1              // Thermal quality of Ice
#define SNMASS_DIV          4.5     // mass cross-section division (kg/m^2) at depth 5 mm
```